Measurement of the Proton and Deuteron Spin Structure Functions g_1 and g_2

William Alexander Tobias

Stanford Linear Accelerator Center
Stanford University
Stanford, CA 94309

SLAC-Report-617
March 2003

Prepared for the Department of Energy
under contract number DE-AC03-76SF00515

Printed in the United States of America. Available from the National Technical Information
Service, U.S. Department of Commerce, 5285 Port Royal Road, Springfield, VA 22161.

Measurement of the Proton and Deuteron Spin Structure Functions g_1 and g_2

William Alexander Tobias
Charlottesville, VA

B.S., The College of William & Mary, 1992
M.A., University of Virginia, 1995

A Dissertation Presented to the Graduate
Faculty of the University of Virginia
in Candidacy for the Degree of Doctor of Philosophy

Department of Physics
University of Virginia
January, 2001

To compassion, friendship and peace in the world.

Abstract

Measurement of the Proton and Deuteron Spin Structure Functions g_1 and g_2

William A. Tobias
Under the supervision of Prof. Donald G. Crabb
At the University of Virginia

The SLAC experiment E155 was a deep-inelastic scattering experiment that scattered polarized electrons off polarized proton and deuteron targets in the effort to measure precisely the proton and deuteron spin structure functions. The nucleon structure functions g_1 and g_2 are important quantities that help test our present models of nucleon structure. Such information can help quantify the constituent contributions to the nucleon spin. The structure functions g_1^p and g_1^d have been measured over the kinematic range $0.01 \leq x \leq 0.9$ and $1 \leq Q^2 \leq 40$ GeV^2 by scattering 48.4 GeV longitudinally polarized electrons off longitudinally polarized protons and deuterons. In addition, the structure functions g_2^p and g_2^d have been measured over the kinematic range $0.01 \leq x \leq 0.7$ and $1 \leq Q^2 \leq 17$ GeV^2 by scattering 38.8 GeV longitudinally polarized electrons off transversely polarized protons and deuterons. The measurements of g_1 confirm the Bjorken sum rule and find the net quark polarization to be $\Delta\Sigma = 0.23 \pm 0.04 \pm 0.6$ while g_2 is found to be consistent with the g_2^{WW} model.

Acknowledgments

I would like to thank Dr. Donald Crabb for his support, both as a teacher in the laboratory and as my thesis advisor. Knowledge is experience. Through the efforts of physicists Ray Arnold, Peter Bosted, Stephen Bültmann, Donal Day, Jim Johnson, Jim McCarthy, Joe Mitchell, Steve Rock and my fellow E155 thesis students Paul King, Paul McKee, Greg Mitchell, Terry Toole, Frank Wesselmann, I gained valuable experience in the laboratory, on analysis and what it is to be an experimental physicist. A special thanks to Oscar Rondon, who helped with the subtle physics details. I like to also thank the companionship of Todd Averett, Chris Cothran, Robin Erbacher, Chris Harris, Renee Hutchins (now Fatemi), Pote Pothongsunan, Marcy Stutzmann, Dave Zimmermann, Eric Wulf, Yoshida and the Virginia Physics Department.

However, school is not possible without distractions and friends that made the journey enjoyable and extremely fruitful. Experimental particle physics brought journeys to many different places (Monroe, Alderman, Brandon, Pagemill, La Barranca, Emerson, Kingsley, Thomson and Old Lynchburg): I will remember ... George, Pete and Moe ... Kurt, Lisa, John, Christie and Ali ... Mike, Ryan, Chris, Joaquin, Peter and Steve ... Priscilla, Sara, Lily, Katia and Elliot ... Josh, Anne-Kathrin, Tom, Anthony, and Quark ... and so many others, sorry if did not mention you!

Of course I have to thank my family, parents Herbert and Eva, brother Herb and sister Eva for their support in my pursuit of a degree in an overwhelming subject. My technical skills in the laboratory were undoubtedly shaped by my Dad, the engineer and household handy man.

Contents

List of Figures

List of Tables

Chapter 1

Introduction

Early elastic and inelastic electron-proton scattering experiments carried out in the late 1960's at the Stanford Linear Accelerator Center led to the discovery of point-like objects within the proton and the phenomenon known as scaling [1, 2, 3]. In the first-order approximation of QED, electrons interact as point particles (infinitesimal volume) while protons have structure (finite volume). Elastic electron-electron scattering cross-sections are large at large angles. This would suggest that electrons are much like *hard* billiard balls that bounce off one another. Elastic electron-proton cross-sections are large at small angles and drop off quickly at large angles, suggesting protons are *soft*, modifying a passing particle's path by a small amount. However, when the inelastic electron-proton cross-section data are compared to elastic electron-electron cross-sections, it is evident that the dependence on the four-momentum transfer between the electron and proton, $-q^2$, of both processes are similar. This would indicate that in the deep-inelastic energy regime, the electrons are hard scattering off point-like scattering centers within the proton. At the time, it was shown that spin averaged inelastic electron-proton scattering could be expressed in terms of two independent structure functions, W_1 and W_2, which are functions of two independent kinematic variables, four-momentum transfer $-q^2 = Q^2 = 4EE^{'} \sin^2{(\theta/2)}$ and energy transfer $\nu = E - E^{'}$, where E is the initial electron energy, $E^{'}$ the final electron energy and θ is the angle through which the electron is scattered. It was shown that within a kinematic limit where $-q^2$ and ν become large but with a fixed ratio (ie. limit $-q^2 = Q^2$,$\nu \longrightarrow \infty$), W_1 and νW_2 should not depend on $-q^2$ and ν independently, but be functions of the ratio ν/q^2. This means that different $-q^2$ measurements fall on the same curve when the structure functions are plotted against the ratio ν/q^2. In the field it is common to express the four-momentum squared as $Q^2 \equiv -q^2 \geq 0$.

In QCD, the coupling between quarks goes to zero as the momentum transfer $Q^2 \longrightarrow \infty$. This led Bjorken [4] to the idea that in the asymptotic freedom limit $(\nu, Q^2 \longrightarrow \infty)$ quarks behave as "free" point-like objects within the nucleon, much like point-like charged leptons. This came to be known as Bjorken scaling and the new scaling variable $x = \frac{Q^2}{2M\nu}$ was defined, which can be interpreted as the fraction of the nucleon momentum carried by the scattering quark. The early experiments that led to the discovery of quarks and scaling were led by a collaboration of physicists from MIT and SLAC [5].

It was Gell-Mann [6] and Zweig [7] that first proposed that hadrons were composites of point-like charged spin-1/2 fermions (1964), which later took on the name of quarks (partons as Feynman called them). The nucleon is believed to be made up of three valence quarks held together by gluons which mediate the strong force and a quark-antiquark sea. Once the idea of quarks was accepted, theory and experiment continued in the direction of explaining how these constituents make up the nucleon. For example, how do the properties of the constituent quarks add up to the total charge, spin and magnetic moment of the nucleon? The nucleon charge and magnetic moment are well described in the framework of three constituent quarks; however, nucleon spin is not as well understood.

1.1 Nucleon Spin Puzzle

Quarks carry an intrinsic spin of $\frac{1}{2}$. Naively one can assume that only the three valence quarks carry the nucleon spin, while the sea quarks and gluons do not contribute since they are not polarized. Hence, the valence quarks alone could add up to give the ground state spin of $\frac{1}{2}$ of the nucleon. From experimental measurements, it turns out the case is not that simple. “Where does the spin of the nucleon come from?” This question can be answered by studying spin dependent processes such as deep-inelastic scattering of polarized leptons from polarized nucleon targets. Spin dependent deep-inelastic scattering allows us to measure the spin structure functions $g_1(x)$ and $g_2(x)$ which contain information on the spin content of the nucleons on the quark and gluon level. This can be accomplished by testing sum rule predictions for the integrals of the structure functions such as the Bjorken [section (1.7.1)], Ellis-Jaffe [section (1.7.2)] and Burkhardt-Cottingham [section (1.7.3)] sum rules.

In 1976, the E80 SLAC-Yale collaboration [8], and again in 1983 as the E130 collaboration [9], measured asymmetries in the deep-inelastic scattering of polarized electrons off polarized protons. Their results verified within the experiment’s large error the Ellis-Jaffe sum rule for $g_1^p(x)$, a prescription to account for the spin within the proton and neutron using a model that assumes no strange quark polarization. In 1988, the European Muon Collaboration (EMC) [10] made a high precision measurement of the proton spin structure function scattering polarized muons off polarized protons. Their results obtained:

$$\int_0^1 g_1^p(x)dx = 0.114 \pm 0.012 \pm 0.026 \tag{1.1}$$

which did not agree with the Ellis-Jaffe sum rule prediction of ∼ 0.185. As a result, the collaboration concluded that only a small percentage of the nucleon spin is carried by the quarks. If EMC assumed no strange quark polarization, the data implied that only $(14 \pm 9 \pm 21)\%$ of the proton spin is carried by the quarks. On the other hand, if EMC assumed the difference between the data and the Ellis-Jaffe sum rule is due to a polarized strange quark sea, they found that the quark spins carry $(1 \pm 12 \pm 24)\%$ of the proton spin. Later other experiments such as the CERN's Spin Muon Collaboration (SMC), and the SLAC experiments 142 and 143 (E142 and E143) indicated significant deviations of the data from the predictions made by the Ellis-Jaffe sum rule. This disagreement was coined as the "spin crisis" [11], which indicates that the spin of the nucleon cannot be explained by simple sum of the spins of the valence quarks in the nucleon [12]. However, many agree that there never was and there is no spin "crisis", rather a "nucleon spin puzzle [13]". Further analysis suggests that spin contributions from the gluons and the sea quarks within the nucleon must be taken into account in order to explain the spin structure of the proton and neutron [14, 15]. One can decompose the total nucleon spin in terms of spin contributions from the quarks (valence quarks and the sea), gluons and the orbital angular momentum of the constituents into the spin sum rule:

$$S_z = \frac{1}{2}\Delta\Sigma + \Delta G + \langle L_z \rangle = \frac{1}{2} \tag{1.2}$$

where the quark contribution and the orbital angular momentum of the system are given by:

$$\Delta\Sigma = \Delta u + \Delta d + \Delta s \tag{1.3}$$

$$\langle L_z \rangle = \langle L_q \rangle + \langle L_G \rangle . \tag{1.4}$$

The data on the g_1 spin structure function provides a strong constraint on the net quark polarization $\Delta\Sigma$ [16].

Details on how one can extract g_1 and g_2 from deep-inelastic scattering are discussed in the following sections. Information on how g_1 and g_2 can be used to extract spin structure information via various quark models is provided in section (1.5).

1.2 Deep-Inelastic Scattering

Inelastic electron-nucleon scattering, which for large momentum transfer is typically referred to as *deep-inelastic scattering* (DIS), is a powerful method through which the internal spin structure information of the proton and neutron can be extracted [17]. In this experiment, we concern ourselves with *inclusive* electron-nucleon scattering, where only the scattered electron is detected and the hadronic final state is not detected. The formalism for DIS can be found in any book on high energy physics.

The general form of the inclusive reaction can be denoted by

$$e + N \longrightarrow e' + X \tag{1.5}$$

where e, e' are the initial and final electron states, N is the target nucleon and X is the hadronic final state. In the single photon exchange approximation (the Born process which is to first order in α), an electron with momentum k scatters off a nucleon with mass M and momentum P which can be represented by the Feynman

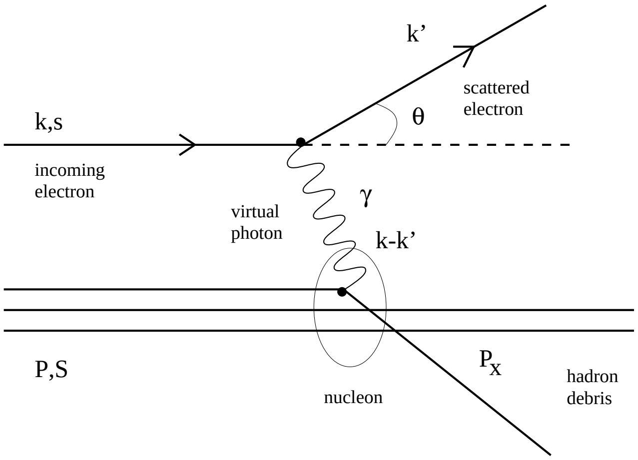

Figure 1.1: **Leading Order Feynman Diagram for Deep-Inelastic Scattering** Leading order reaction contains a single virtual photon exchange between the incoming electron and the struck quark inside the nucleon.

diagram in figure (1.1). In the process there is an exchange of a virtual photon with momentum q between the electron and the nucleon. Table (1.1) characterizes the electron, virtual photon and nucleon states [18]. Moreover, DIS can be characterized by relativistically invariant quantities: four momentum transfer Q^2, energy transfer ν and the relativistically invariant mass W of the hadronic final state, as denoted in table (1.2). It is useful to define additional kinematic factors used in deep inelastic scattering relations. Table (1.3) defines factors used in expressing various asymmetry and structure function relations. *Deep-inelastic* refers to kinematics where Q^2 and the mass W of the hadronic final state are large compared with typical hadron masses M.

The inelastic cross-section in the laboratory frame is given by

$$\frac{d^2\sigma}{d\Omega dE'} = \frac{4\alpha^2}{Q^4}\frac{E'}{E}L_{\mu\nu}W^{\mu\nu} \tag{1.6}$$

where α is the fine structure constant, $d\Omega$ is the differential solid angle of the scattered

	electron	**virtual photon**	**nucleon**
energy	$E, E^{'}$	$\nu = E - E^{'}$	
four momentum	$k, k^{'}$	$q = k - k^{'}$	P, P_X
mass	m		M, W
spin four vector	s		S

Table 1.1: **DIS Kinematic Variables** The incident electron has four momentum $k = (E, \vec{k})$ and the scattered electron has $k^{'} = (E^{'}, \vec{k^{'}})$ The laboratory scattering angle of the electron is θ. W (P_X) is the mass (four momentum) of the hadronic final state. The deep-inelastic region of scattering is defined by the conditions such that $Q^2 \gg M^2$ and $W \gg M$.

$$\boxed{\begin{aligned} &Q^2 = -q^2 = -(k - k^{'})^2 = 4EE^{'} \sin^2\left(\tfrac{\theta}{2}\right) \\ &\nu = \tfrac{P \cdot Q}{M} = E - E^{'} \\ &W^2 = P_X^2 = (P + q)^2 = M^2 + 2M\nu - Q^2 \end{aligned}}$$

Table 1.2: **Relativistic Invariants**

$x = \frac{Q^2}{2M\nu}$	Bjorken scaling variable
$y = \frac{\nu}{E}$	fractional energy loss of scattered electron
$\varepsilon^{-1} = \left[1 + 2\left(1 + \frac{\nu^2}{Q^2}\right)\tan^2\left(\frac{\theta}{2}\right)\right]$	virtual photon longitudinal polarization
$\gamma^2 = \frac{4M^2x^2}{Q^2} = \frac{Q^2}{\nu^2}$	gamma kinematic factor
$f_k = \frac{1}{\nu F_1(x,Q^2)} \frac{(1-\varepsilon)}{[1+\varepsilon R(x,Q^2)]}$	kinematic factor
$D' = \frac{(1-\varepsilon)(2-y)}{y[1+\varepsilon R(x,Q^2)]}$	depolarization factor
$D = \frac{(1-E^{'}\varepsilon/E)}{[1+\varepsilon R(x,Q^2)]}$	depolarization factor
$\eta = \frac{\varepsilon\sqrt{Q^2}}{E-\varepsilon E'}$	kinematic factor
$d = D\sqrt{\frac{2\varepsilon}{1+\varepsilon}}$	depolarization factor
$\zeta = \frac{\eta(1+\varepsilon)}{2\varepsilon}$	kinematic factor
$R(x,Q^2) = \frac{\sigma^L_{1/2}}{\sigma^T} = \left[\frac{F_2}{F_1}\frac{(1+\gamma^2)}{2x} - 1\right]$	longitudinal to transverse virtual scattering

Table 1.3: **Additional DIS Kinematic Definitions** Kinematic variables and factors defined for deep-inelastic scattering. $F_1(x,Q^2)$ is the spin averaged structure function for magnetic scattering which is calculable from $F_2(x,Q^2)$, the spin averaged structure function for electric scattering, and $R(x,Q^2)$ via equation (1.36). Figures (4.15) and (E.1) show F_2, R and F_1 plotted as a function of x and Q^2.

electron with respect to the beam axis and $L_{\mu\nu}$ and $W^{\mu\nu}$ are tensors that describe the structures of the leptonic and hadronic vertices. The lepton current tensor $L_{\mu\nu}$ consists of spin-independent symmetric $L^{(S)}_{\mu\nu}$ and spin-dependent antisymmetric $L^{(A)}_{\mu\nu}$ parts [19, 20, 21, 22, 23].

$$L_{\mu\nu} = L^{(S)}_{\mu\nu} + iL^{(A)}_{\mu\nu} \tag{1.7}$$

$$L^{(S)}_{\mu\nu} = k'_{\mu}k_{\nu} + k'_{\nu}k_{\mu} - g_{\mu\nu}k' \cdot k \tag{1.8}$$

$$L^{(A)}_{\mu\nu} = m\varepsilon_{\mu\nu\alpha\beta}s^{\alpha}q^{\beta} \tag{1.9}$$

The hadronic tensor amplitude $W^{\mu\nu}$ consists of a spin independent symmetric part that defines the $W_1(Q^2,\nu)$ and $W_2(Q^2,\nu)$ unpolarized structure functions, and a spin-dependent part that defines the $G_1(Q^2,\nu)$ and $G_2(Q^2,\nu)$ spin structure functions [24].

$$W^{\mu\nu} = W^{\mu\nu}_{(S)} + iW^{\mu\nu}_{(A)} \tag{1.10}$$

$$W^{\mu\nu}_{(S)} = \left(-g^{\mu\nu} + \frac{q^{\mu}q^{\nu}}{q^2}\right)W_1(\nu,Q^2) + \frac{1}{M^2}\left(P^{\mu} - \frac{P\cdot q}{q^2}q^{\mu}\right)\left(P^{\nu} - \frac{P\cdot q}{q^2}q^{\nu}\right)W_2(\nu,Q^2) \tag{1.11}$$

$$W^{\mu\nu}_{(A)} = M\varepsilon^{\mu\nu\alpha\beta}q_{\alpha}S_{\beta}G_1(\nu,Q^2) + \frac{1}{M}\varepsilon^{\mu\nu\alpha\beta}q_{\alpha}[(P\cdot q)S_{\beta} - (S\cdot q)P_{\beta}]G_2(\nu,Q^2) \tag{1.12}$$

Summing over all spin states, the unpolarized cross-section is proportional to $L^{(S)}_{\mu\nu}W^{\mu\nu}_{(S)}$ and is the function of the two spin averaged structure functions $W_1(\nu,Q^2)$ and $W_2(\nu,Q^2)$, where the leading term $4\alpha^2E'^2\cos^2(\theta/2)/Q^4$ is σ_{Mott}, the Mott cross-section for elastic scattering of spinless electrons by spinless pointlike nuclei [25].

$$\frac{d^2\sigma^{unpol}}{d\Omega dE'} = \frac{4\alpha^2E'^2\cos^2\left(\frac{\theta}{2}\right)}{Q^4}\left[2W_1(\nu,Q^2)\tan^2\left(\frac{\theta}{2}\right) + W_2(\nu,Q^2)\right] \tag{1.13}$$

The difference in cross-sections between target nucleons with opposite spin is proportional to $L^{(A)}_{\mu\nu}W^{\mu\nu}_{(A)}$ and is the function of the two spin polarized structure functions $G_1(\nu,Q^2)$ and $G_2(\nu,Q^2)$. For electrons polarized along the beamline (thin arrow) and target nucleons polarized either parallel or transverse (thick arrow) to the electron spin, the difference in cross-sections are:

$$\frac{d^2\Delta\sigma_{\parallel}}{d\Omega dE'} = \frac{d^2\sigma^{\downarrow\Uparrow}}{d\Omega dE'} - \frac{d^2\sigma^{\uparrow\Uparrow}}{d\Omega dE'} = \frac{4\alpha^2}{Q^2}\frac{E'}{E}\left[MG_1(\nu,Q^2)(E+E'\cos(\theta)) - Q^2G_2(\nu,Q^2)\right] \tag{1.14}$$

$$\frac{d^2\Delta\sigma_{\perp}}{d\Omega dE'} = \frac{d^2\sigma^{\downarrow\Leftarrow}}{d\Omega dE'} - \frac{d^2\sigma^{\uparrow\Leftarrow}}{d\Omega dE'} = \frac{4\alpha^2}{Q^2}\frac{E'}{E}E'\sin(\theta)\left[MG_1(\nu,Q^2) + 2EG_2(\nu,Q^2)\right] \tag{1.15}$$

In the asymptotic limit, or the Bjorken limit, one allows $\nu, Q^2 \longrightarrow \infty$ while keeping the ratio finite. The structure functions then become a function of a single scaling variable $x = Q^2/2M\nu$. Bjorken x is the fraction of the total nucleon momentum carried by the struck quark.

$$\lim_{\nu,Q^2\longrightarrow\infty}\left[MW_1(\nu,Q^2) = F_1(\nu,Q^2)\right] = F_1(x) \tag{1.16}$$

$$\lim_{\nu,Q^2\longrightarrow\infty}\left[\nu W_2(\nu,Q^2) = F_2(\nu,Q^2)\right] = F_2(x) \tag{1.17}$$

$$\lim_{\nu,Q^2\longrightarrow\infty}\left[M^2\nu G_1(\nu,Q^2) = g_1(\nu,Q^2)\right] = g_1(x) \tag{1.18}$$

$$\lim_{\nu,Q^2\longrightarrow\infty}\left[M\nu^2 G_2(\nu,Q^2) = g_2(\nu,Q^2)\right] = g_2(x) \tag{1.19}$$

The differential cross-section in the laboratory frame for unpolarized lepton-nucleon scattering in the asymptotic limit is:

$$\frac{d^2\sigma^{unpol}}{d\Omega dE'} = \frac{4\alpha^2E'^2\cos^2\left(\frac{\theta}{2}\right)}{Q^4}\left[\frac{2F_1(x)}{M}\tan^2\left(\frac{\theta}{2}\right) + \frac{F_2(x)}{\nu}\right]. \tag{1.20}$$

The differential cross-sections in the laboratory frame for polarized lepton-nucleon scattering in the asymptotic limit are

$$\frac{d^2\Delta\sigma_{\|}}{d\Omega dE'} = \frac{d^2\sigma^{\downarrow\Uparrow}}{d\Omega dE'} - \frac{d^2\sigma^{\uparrow\Uparrow}}{d\Omega dE'} = \frac{4\alpha^2}{Q^2}\frac{E'}{E}\left[\frac{g_1(x)}{M\nu}(E+E'\cos(\theta)) - Q^2\frac{g_2(x)}{M\nu^2}\right], \tag{1.21}$$

$$\frac{d^2\Delta\sigma_{\perp}}{d\Omega dE'} = \frac{d^2\sigma^{\downarrow\Leftarrow}}{d\Omega dE'} - \frac{d^2\sigma^{\uparrow\Leftarrow}}{d\Omega dE'} = \frac{4\alpha^2}{Q^2}\frac{E'}{E}E'\sin(\theta)\left[\frac{g_1(x)}{M\nu} + 2E\frac{g_2(x)}{M\nu^2}\right]. \tag{1.22}$$

1.3 Polarized Cross-Section Asymmetries

The difference in cross-sections for spin dependent scattering of electrons off nucleons with electron spin (anti-)parallel or right (left) transverse to the target polarization leads to a parallel or perpendicular asymmetry:

$$A_{\|} = \frac{\sigma^{\downarrow\Uparrow} - \sigma^{\uparrow\Uparrow}}{\sigma^{\downarrow\Uparrow} + \sigma^{\uparrow\Uparrow}} = f_k[g_1(x,Q^2)[E+E'\cos(\theta)] - \frac{Q^2}{\nu}g_2(x,Q^2)] \tag{1.23}$$

$$A_{\perp} = \frac{\sigma^{\downarrow\Leftarrow} - \sigma^{\uparrow\Leftarrow}}{\sigma^{\downarrow\Leftarrow} + \sigma^{\uparrow\Leftarrow}} = f_k E'\sin(\theta)[\frac{2E}{\nu}g_2(x,Q^2) + g_1(x,Q^2)] \tag{1.24}$$

where f_k is a kinematic factor defined in table(1.3). The parallel and perpendicular scattering asymmetries are also related to the virtual photon-nucleon asymmetries A_1 and A_2 as discussed in section (1.4).

$$A_{\|} = D(A_1 + \eta A_2) \tag{1.25}$$

$$A_{\perp} = d(A_2 - \zeta A_1) \tag{1.26}$$

Since the cross-sections are proportional to the number of scattered leptons per incident lepton charge or *rate* of scattered leptons, the asymmetries are measured using the difference in left and right handed electron helicity rates ($R_L = N_L/Q_L$ and $R_R = N_R/Q_R$) [Note that the spin polarization of particles is often referred to by the term *helicity*]. Measuring the difference in cross-sections (asymmetries) instead of absolute cross-sections allows common factors such as detector efficiency and acceptance to cancel. Moreover, measuring these rates for both helicity states with the same spectrometer simultaneously minimizes any time-dependent effects. The measured asymmetries can be represented by:

$$A_{\|}(A_{\perp}) = \frac{1}{fP_bP_t} \cdot \left(\frac{R_L - R_R}{R_L + R_R}\right). \tag{1.27}$$

The quantity $(R_L - R_R)/(R_L + R_R)$ is known as the *raw* or *counting rate asymmetry*, and f, P_b, P_t are factors to correct for scattering off nucleons other than polarized protons or deuterons, beam polarization and target polarization respectively. There are also radiative and other asymmetry corrections that are applied. More on this in section (3.3).

The spin structure functions can be solved in terms of the parallel and perpendicular asymmetries $A_{\|}$ and $A_{\perp}$, the structure function $F_1(x, Q^2)$ and the kinematic depolarization factor $D^{'}$ as defined in table (1.3):

$$g_1(x, Q^2) = \frac{F_1(x, Q^2)}{D'}\left[A_{\|} + \tan\left(\frac{\theta}{2}\right)A_{\perp}\right] \tag{1.28}$$

$$g_2(x, Q^2) = \frac{F_1(x, Q^2)}{D'}\frac{y}{2\sin\theta}\left[\frac{(E + E'\cos\theta)}{E'}A_{\perp} - \sin\theta A_{\|}\right]. \tag{1.29}$$

1.4 Virtual Photon Asymmetries

One can also write $g_1(x, Q^2)$ and $g_2(x, Q^2)$ in terms of the virtual photon asymmetries A_1 and A_2, which involve the interaction between the virtual photon and the nucleon. The transverse virtual photon-nucleon absorption cross-sections $\sigma^T_{1/2}$ and $\sigma^T_{3/2}$ are for processes where the projection of the total angular momentum of the system along the incident photon direction is 1/2 and 3/2 respectively [26]. The $\sigma^{TL}_{1/2}$ term arises from the interference between transverse and longitudinal amplitudes. These cross-sections are related to the structure functions in the following equations where $K = \nu - Q^2/2M$ is the flux of the incoming virtual photons:

$$\sigma^T_{1/2} = \frac{4\pi^2\alpha}{MK}\left[F_1 + g_1 - \left(\frac{2Mx}{\nu}\right)g_2\right] \tag{1.30}$$

$$\sigma^T_{3/2} = \frac{4\pi^2\alpha}{MK}\left[F_1 - g_1 + \left(\frac{2Mx}{\nu}\right)g_2\right] \tag{1.31}$$

$$\sigma^L_{1/2} = \frac{4\pi^2\alpha}{K}\left[\frac{F_2}{\nu}\left(1 + \frac{\nu^2}{Q^2}\right) - \frac{F_1}{M}\right] \tag{1.32}$$

$$\sigma^{TL}_{1/2} = \frac{4\pi^2\alpha}{K}\frac{\sqrt{Q^2}}{M\nu}(g_1 + g_2) \tag{1.33}$$

From these relations and the definitions for A_1 and A_2, one can express the asymmetries in terms of the spin averaged and polarized structure functions.

$$A_1 = \frac{\sigma^T_{1/2} - \sigma^T_{3/2}}{\sigma^T_{1/2} + \sigma^T_{3/2}} = \frac{g_1(x,Q^2) - \gamma^2 g_2(x,Q^2)}{F_1(x,Q^2)} \tag{1.34}$$

$$A_2 = \frac{2\sigma^{TL}_{1/2}}{\sigma^T_{1/2} + \sigma^T_{3/2}} = \gamma\frac{g_1(x,Q^2) + g_2(x,Q^2)}{F_1(x,Q^2)} \tag{1.35}$$

For the kinematics of our experiment, the unpolarized structure functions $F_1(x,Q^2)$ and $F_2(x,Q^2)$ can be related by

$$F_1(x,Q^2) = F_2(x,Q^2) \cdot \frac{(1+\gamma^2)}{2x\left[1 + R(x,Q^2)\right]} \tag{1.36}$$

which is derived from equations (1.30) thru (1.33). In the scaling limit, the above expression reduces to the Callan-Gross relation:

$$F_1(x,Q^2) = \frac{F_2(x,Q^2)}{2x}. \tag{1.37}$$

One can reverse the equations (1.34) and (1.35) and express g_1 and g_2 in terms of the virtual photon asymmetries:

$$g_1(x, Q^2) = \frac{F_2(x, Q^2)}{2x\left[1 + R(x, Q^2)\right]}\Big(A_1 + \gamma A_2\Big) \tag{1.38}$$

$$g_2(x, Q^2) = \frac{F_2(x, Q^2)}{2x\left[1 + R(x, Q^2)\right]}\Big(A_2/\gamma - A_1\Big) \tag{1.39}$$

Note that from (1.25) and (1.26), one can find expressions that allow one to extract A_1 and A_2 from the experimental asymmetries $A_{||}$ and $A_{\perp}$.

An advantage of using the virtual photon asymmetries over g_1 and g_2 is that one can provide a bound for A_1 and A_2 via positivity. The magnitude of A_1 can never exceed 1, while A_2 can never exceed $\sqrt{R}$ [27].

$$\mid A_1 \mid \leq 1 \tag{1.40}$$

$$\mid A_2 \mid \leq \sqrt{R} \tag{1.41}$$

Soffer and Teryaev investigated the well established positivity study done by Doncel and de Rafael from which they rederived a stronger bound for the transverse asymmetry, which could be called the Soffer-Teryaev limit [28].

$$\mid A_2 \mid \leq \sqrt{\frac{R(1 + A_1)}{2}} \tag{1.42}$$

1.5 Quark Models

In the simplest model, Naive Quark Parton Model (NQPM), the nucleons and the other low mass ground state baryons are described as bound states of three different valence quarks, the *up*, *down* and *strange* (u, d, s), with no orbital angular momentum

flavor (q)	**spin**	**isospin (I)**	I_3	**strangeness (S)**	**charge (Q)**	**baryon # (B)**	**hypercharge (Y)**
u	$\frac{1}{2}$	$\frac{1}{2}$	$+\frac{1}{2}$	0	$+\frac{2}{3}$	$\frac{1}{3}$	$+\frac{1}{3}$
d	$\frac{1}{2}$	$\frac{1}{2}$	$-\frac{1}{2}$	0	$-\frac{1}{3}$	$\frac{1}{3}$	$+\frac{1}{3}$
s	$\frac{1}{2}$	0	0	-1	$-\frac{1}{3}$	$\frac{1}{3}$	$-\frac{2}{3}$

Table 1.4: **Quark Quantum Numbers** [14, 21] The proton and neutron are considered an isospin doublet, in much the same way the electron spin up and spin down states are considered a spin doublet. Since the mass of the proton and the neutron are very close in value, it could indicate that the proton and neutron may actually be two different states of the same particle, the nucleon. The mathematical tools used to describe this nucleon doublet are exactly the same as for describing the spin states of the electron, hence the name isospin [21]. Notice that adding up the isospin numbers for three quarks gives the +1/2 (-1/2) isospin for the proton (neutron).

and gluons that are unpolarized [29]. Important quantum number properties of the light quarks are listed in table (1.4). In this formalism, the proton is made up of two *up* and one *down* (*uud*), and the neutron is made up of one *up* and two *down* (*ddu*), both containing no strange quarks. Naively, many properties of the proton and neutron can be described by a sum of the valence quark properties alone. For example, the proton +1 charge (neutron 0 charge) can be explained by a sum of *up* and *down* quark fractional charges +2/3, +2/3 and -1/3 (-1/3, -1/3, +2/3). One might assume the nucleon's spin 1/2 can be described by a combination of three spin 1/2 quarks, but experimentally this turns out not to be the case.

In the NQPM, the spin-flavor component of the wavefunction for a spin up proton and neutron are given by [30]

$$|p^{\uparrow}\rangle = \sqrt{\frac{1}{6}}\Big[|u^{\uparrow}u^{\downarrow}d^{\uparrow}\rangle + |u^{\downarrow}u^{\uparrow}d^{\uparrow}\rangle - 2|u^{\uparrow}u^{\uparrow}d^{\downarrow}\rangle\Big] \tag{1.43}$$

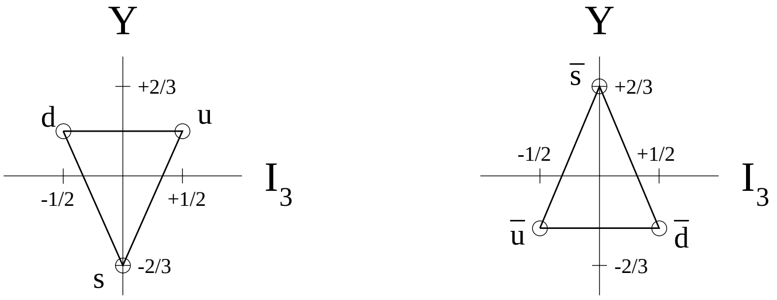

Figure 1.2: **SU(3) Quark and Anti-quark Multiplets** The quark multiplets where I_3 is the third component of isotopic spin and Y = B+S is the hypercharge additive quantum number [21].

$$|n^{\uparrow}\rangle = \sqrt{\frac{1}{6}}\Big[|d^{\uparrow}d^{\downarrow}u^{\uparrow}\rangle + |d^{\downarrow}d^{\uparrow}u^{\uparrow}\rangle - 2|d^{\uparrow}d^{\uparrow}u^{\downarrow}\rangle\Big] \tag{1.44}$$

in the SU(3) limit. One can define $q_{\uparrow}$ and $q_{\downarrow}$ to represent the quark distributions of spin up and spin down partons of flavor q in the proton (neutron). For example, one can determine these quark distributions by calculating the probability that a quark q is in spin state ↑ (↓) using

$$q^{\uparrow} = \sum \Big|\langle p^{\uparrow}|q^{\uparrow}\rangle\Big|^2. \tag{1.45}$$

From the probabilities of finding the spin up proton in the three different quark spin combination states

$$\big|\langle p^{\uparrow}|u^{\uparrow}u^{\downarrow}d^{\uparrow}\rangle\big|^2 = 1/6 \tag{1.46}$$

$$\big|\langle p^{\uparrow}|u^{\downarrow}u^{\uparrow}d^{\uparrow}\rangle\big|^2 = 1/6 \tag{1.47}$$

$$\big|\langle p^{\uparrow}|u^{\uparrow}u^{\uparrow}d^{\downarrow}\rangle\big|^2 = 2/3 \tag{1.48}$$

the individual distributions for u, d and s are readily determined, where the factor of two in equation (1.49) for $u^{\uparrow}$ is due to the fact that two u-quarks with spin up exist in the $|u^{\uparrow}u^{\uparrow}d^{\downarrow}\rangle$ state.

$$u^{\uparrow} = \left(\frac{1}{6}\right) + \left(\frac{1}{6}\right) + 2\cdot\left(\frac{2}{3}\right) = \frac{5}{3} \tag{1.49}$$

$$u^{\downarrow} = \left(\frac{1}{6}\right) + \left(\frac{1}{6}\right) + 2\cdot\left(0\right) = \frac{1}{3} \tag{1.50}$$

$$d^{\uparrow} = \left(\frac{1}{6}\right) + \left(\frac{1}{6}\right) + \left(0\right) = \frac{1}{3} \tag{1.51}$$

$$d^{\downarrow} = \left(0\right) + \left(0\right) + \left(\frac{2}{3}\right) = \frac{2}{3} \tag{1.52}$$

$$s^{\uparrow} = s^{\downarrow} = 0 \tag{1.53}$$

Equation (1.53) reflects that there is no *strange sea* in the NQPM.

Working in the infinite momentum frame and using equation (1.2) as a guide, this simple parton model assumes no spin comes from a strange sea $\Delta s = 0$ such as assumed in the Ellis-Jaffe sum rule [section (1.7.2)], $\Delta G = 0$ since the gluons are considered to be unpolarized and do not participate in the spin-dependent scattering process and $L_z = 0$ if one takes $\vec{k} \parallel \vec{P}$ and $\vec{L} = \vec{r} \times \vec{k}$ where $\vec{P}$ is the linear momentum of the parent nucleon, $\vec{k}$ is the linear momentum of the quark and $\vec{r}$ is the nucleon radius ($L_z \neq 0$ if one assumes the partons have non-zero transverse momentum, k_T). Hence, for the proton we find that all of the nucleon spin is carried by the three valence quarks (uud) since $\Delta\Sigma = 1$.

$$S_z = \frac{1}{2}\Delta\Sigma + \Delta G + \langle L_z \rangle \tag{1.54}$$

$$= \frac{1}{2}\left[\Delta u + \Delta d + \Delta s\right] + 0 + 0 \tag{1.55}$$

$$= \frac{1}{2}\left[\frac{4}{3} - \frac{1}{3} + 0\right] = \frac{1}{2} \tag{1.56}$$

It turns out that experimental measurements constrain the quark spin contribution to

$\Delta\Sigma \sim 0.2$, indicating not all the nucleon spin comes from the quarks. Contributions from the strange sea and gluons must be important as well as an orbital angular momentum contribution due to non-zero quark transverse momentum. The success of the NQPM lies in its ability to readily predict the magnetic moment ratio between the neutron and proton and explain the mass difference between different baryons [14].

1.5.1 Spin Structure from Quark Models

In the scaling limit $Q^2 \longrightarrow \infty$ of the NQPM, the structure functions only depend on x and can be related to the quark spin distributions. The spin-averaged functions can be written in terms of the sum q_i while the spin-polarized functions are related to the difference Δq_i:

$$q_i(x) = [q_i^{\uparrow}(x) + q_i^{\downarrow}(x)] \tag{1.57}$$

$$\Delta q_i(x) = [q_i^{\uparrow}(x) - q_i^{\downarrow}(x)]. \tag{1.58}$$

We can write the following relations for the spin averaged structure functions:

$$F_1(x) = \frac{1}{2}\sum_i e_i^2 q_i(x) \tag{1.59}$$

$$F_2(x) = x\sum_i e_i^2 q_i(x). \tag{1.60}$$

The g_1 spin structure function is related to the longitudinal polarization of the constituent quarks while g_2 is related to the transverse component. The NQPM assumes the internal quarks possess no spin or momentum transverse to the nucleon momentum since the quarks are considered free or non-interacting. Therefore, in the scaling limit, the NQPM describes the quark distributions as having no transverse momentum which well describes g_1 and gives a zero value to g_2:

$$g_1(x) = \frac{1}{2}\sum_i e_i^2 \Delta q_i(x) \tag{1.61}$$

$$g_2(x) = 0. \tag{1.62}$$

The above equations assume free "non-interacting" partons and "on-shell" quark masses ($m_i = xM$). The total contributions of u, d and s quarks to the proton spin can be expressed by the integrals over the quark distribution differences:

$$\Delta q_i = \int_0^1 \left[q_i^{\uparrow}(x) - q_i^{\downarrow}(x) \right] dx, i = u, d, s. \tag{1.63}$$

One can define $u^p(x) \equiv d^n(x)$ and $d^p(x) \equiv u^n(x)$ from isospin symmetry between the proton and neutron. Since the quark masses are not exactly the same, isospin is not a totally correct assumption, but is neglected in the framework of the NQPM.

In the framework of this naive model, the integrals of g_1 for proton and neutron can be expressed as:

$$\int_0^1 g_1^p(x)dx = \frac{1}{2}\left(\frac{4}{9}\Delta u + \frac{1}{9}\Delta d + \frac{1}{9}\Delta s \right) \tag{1.64}$$

$$\int_0^1 g_1^n(x)dx = \frac{1}{2}\left(\frac{1}{9}\Delta u + \frac{4}{9}\Delta d + \frac{1}{9}\Delta s \right) \tag{1.65}$$

where the difference in quark spin distributions for proton and neutron are given in

i	u^i	d^i	s^i	Δu^i	Δd^i	Δs^i
p	+2	+1	0	+4/3	-1/3	0
n	+1	+2	0	-1/3	+4/3	0

Table 1.5: **Nucleon Quark Distributions** Quark distribution predictions for the proton and neutron based on the naive quark parton model.

table (1.5). The naive result for these integrals in the scaling limit are:

$$\Gamma_1^p = \int_0^1 g_1^p(x)dx = \frac{1}{2}\left(\frac{4}{9}(+\frac{4}{3}) + \frac{1}{9}(-\frac{1}{3}) + \frac{1}{9}(0)\right) = \frac{5}{18} \tag{1.66}$$

$$\Gamma_1^n = \int_0^1 g_1^n(x)dx = \frac{1}{2}\left(\frac{1}{9}(+\frac{4}{3}) + \frac{4}{9}(-\frac{1}{3}) + \frac{1}{9}(0)\right) = 0. \tag{1.67}$$

Since our experiments probe finite Q^2 and not the infinite Q^2 scaling limit, transverse momentum effects enter through QCD correction terms by assuming "interacting" quarks. This gives a non-zero result for g_2:

$$g_T(x) = g_1(x) + g_2(x) = \frac{1}{2}\sum_i e_i^2 \left(\frac{m_i}{xM}\right)\Delta q_i(x) \tag{1.68}$$

$$g_2(x) = \frac{1}{2}\sum_i e_i^2 \left(\frac{m_i}{xM} - 1\right)\Delta q_i(x). \tag{1.69}$$

However, this method is sensitive to "off-shell" quark masses, $m_i \neq xM$, leaving the operator product expansion method [section (1.6)] a better alternative to the quark model description of g_2.

1.5.2 QCD-Improved Quark Model

Assuming perfect SU(3) flavor symmetry and no polarized gluons contributing to the nucleon spin, the quark spin distribution differences can be related to the singlet a_0

and non-singlet a_3, a_8 quark axial-vector current matrix elements via

$$a_0 = \Delta\Sigma = \Delta u + \Delta d + \Delta s \tag{1.70}$$

$$a_3 = \Delta u - \Delta d \tag{1.71}$$

$$a_8 = \Delta u + \Delta d - 2\Delta s. \tag{1.72}$$

The matrix elements can also be related to the hyperon decay constants, F and D:

$$a_3 = F + D = \left|\frac{g_A}{g_V}\right|_{np} = 1.2670 \pm 0.0035 \tag{1.73}$$

$$a_8 = 3F - D = 0.584 \pm 0.032 \tag{1.74}$$

where the axial-vector/vector coupling constant ratio g_A/g_V is determined from experimental measurements of neutron β decay [31]. The latest values $F = 0.467 \pm 0.0079$ and $D = 0.8039 \pm 0.0080$ [32] are used for all subsequent analyses in this thesis.

Derivations of various sum rules [section (1.7)] utilize these eigenstate relations. Relating the net quark polarization $\Delta\Sigma$ directly to a_0 is the convention used in this thesis since it maintains the NQPM identity

$$\Delta\Sigma_{\overline{MS}} = a_0 \tag{1.75}$$

which is labeled as the modified minimal subtraction ($\overline{MS}$) scheme [33]. An alternative Adler-Bardeen (AB) scheme [34] commonly used includes gluon contributions from ΔG in the relation for $\Delta\Sigma$ such that

$$\Delta\Sigma_{AB} = a_0 + \frac{n_f \alpha_s}{2\pi}\Delta G \tag{1.76}$$

where n_f = number of quark flavors, but is not used in this study, since the NQPM identity of $\Delta\Sigma$ would be lost.

One can express the net quark polarization $\Delta\Sigma$ in terms of F, D and Δs in the $\overline{MS}$ scheme as

$$\Delta\Sigma = 3F - D + 3\Delta s = a_8 + 3\Delta s. \tag{1.77}$$

Assuming $\Delta s = 0$, this expression gives $\Delta\Sigma \sim 0.6$, indicating that not all the spin comes from the quarks.

Much interest has centered around the first moments of the structure functions since the quark helicity contributions to the nucleon spin can be obtained from them. At finite Q^2, the first moments of g_1 take on the QCD corrections which account for quark-gluon interactions within the nucleon and can be obtained in terms of singlet a_0 and non-singlet a_3, a_8 quark axial-vector current matrix elements from equations (1.70) thru (1.72) via

$$\Gamma_1^p(Q^2) = \frac{1}{36}\left[\big(3a_3 + a_8\big)C_{ns} + 4a_oC_s\right] \tag{1.78}$$

$$\Gamma_1^n(Q^2) = \frac{1}{36}\left[\big(-3a_3 + a_8\big)C_{ns} + 4a_oC_s\right] \tag{1.79}$$

$$\Gamma_1^d(Q^2) = \frac{1}{36}\left[a_8C_{ns} + 4a_oC_s\right] \cdot \left(1 - \frac{3}{2}\omega_D\right) \tag{1.80}$$

where $\omega_D = 0.05 \pm 0.01$ is the D-state probability in the deuteron and C_{ns} and C_s are Q^2-dependent non-singlet and singlet QCD corrections [29, 35, 36].

The non-singlet QCD correction, C_{ns}, calculated to third order for three quark flavors is:

$$C_{ns} = \left[1 - \frac{\alpha_s(Q^2)}{\pi} - 3.583\left(\frac{\alpha_s(Q^2)}{\pi}\right)^2 - 20.215\left(\frac{\alpha_s(Q^2)}{\pi}\right)^3\right]. \tag{1.81}$$

The singlet QCD correction can take on two forms, one which gives a Q^2-dependent $a_0(Q^2)$ and one that gives an asymptotic high Q^2 limit of $a_0(Q^2) \longrightarrow a_0^{inv}$. They are:

$$C_s(Q^2) = \left[1 - \frac{\alpha_s(Q^2)}{\pi} - 1.10\left(\frac{\alpha_s(Q^2)}{\pi}\right)^2\right] \tag{1.82}$$

$$C_s^{inv} = \left[1 - 0.333\frac{\alpha_s(Q^2)}{\pi} - 0.550\left(\frac{\alpha_s(Q^2)}{\pi}\right)^2\right]. \tag{1.83}$$

From these QCD correction terms and equations (1.70) thru (1.72), one can readily extract the Q^2-dependent quark contribution $\Delta\Sigma(Q^2) = a_0(Q^2)$ from the measured first moments of the proton, neutron or deuteron and a_3 and a_8 via

$$\Delta\Sigma(Q^2) = \frac{1}{4C_s(Q^2)}\left[36\Gamma_1^p(Q^2) - \big(3a_3 + a_8\big)C_{ns}\right] \tag{1.84}$$

$$\Delta\Sigma(Q^2) = \frac{1}{4C_s(Q^2)}\left[36\Gamma_1^n(Q^2) + \big(3a_3 - a_8\big)C_{ns}\right] \tag{1.85}$$

$$\Delta\Sigma(Q^2) = \frac{1}{4C_s(Q^2)}\left[\frac{36\Gamma_1^d(Q^2)}{(1 + 1.5\omega_D)} - a_8C_{ns}\right]. \tag{1.86}$$

1.6 Operator Product Expansion for g_1 and g_2

The operator product expansion, a more accurate description of g_2 than the NQPM, uses a technique where g_2 is approximated by expanding the matrix element that describes the DIS process in a series of terms proportional to $1/\sqrt{Q^2}$ consisting of renormalized local operators with singular coefficients [23]. Typically OPE is a tool for studying various processes where the operator with the lowest dimension dominates. In the case of deep-inelastic scattering, operators of higher dimension are important, and the new quantum number *twist* orders the dominant effects [37]. Twist is related to both the dimension and spin of the operators. For deep-inelastic scattering, the lowest possible and most dominant twist term is $\tau = 2$. Also significant are the twist-3 terms with higher twist ($\tau > 3$) predicted to be negligible [38].

The OPE method was first presented by Wilson [39] and later utilized by physicists to describe g_1 and g_2. The moments $\Gamma_1^{(n)}$ and $\Gamma_2^{(n)}$ for g_1 and g_2 are

$$\Gamma_1^{(n)} = \int_0^1 x^n g_1(x, Q^2) dx = \frac{a_n}{2}, \quad n = 0, 2, 4, ... \tag{1.87}$$

$$\Gamma_2^{(n)} = \int_0^1 x^n g_2(x, Q^2) dx = \frac{1}{2}\left(\frac{n}{n+1}\right)(d_n - a_n), \quad n = 2, 4, 6, ... \quad . \tag{1.88}$$

The a_n and d_n terms are labeled the twist-2 and twist-3 matrix elements. Normally only the leading moments are evaluated. The d_n matrix elements can be extracted via g_1 and g_2 using the OPE expression below. The d_2 reduced matrix elements for the proton, neutron and deuteron are of interest for the E155 experiment. The $\overline{g}_2$ term is defined in (1.95).

$$d_n = 2\int_0^1 x^n \left[g_1(x, Q^2) + \left(\frac{n+1}{n}\right) g_2(x, Q^2)\right] dx \tag{1.89}$$

$$d_2 = \int_0^1 x^2 \left[2g_1(x, Q^2) + 3g_2(x, Q^2)\right] dx \tag{1.90}$$

$$= 3\int_0^1 x^2 \overline{g_2}(x, Q^2) dx \tag{1.91}$$

The d_2 elements can be expressed in terms of the Γ moments for $g_1(x)$, $g_2(x)$ and $\overline{g_2}(x)$ as follows:

$$d_2 = 2\Gamma_1^{(2)} + 3\Gamma_2^{(2)} = 3\overline{\Gamma_2^{(2)}}. \tag{1.92}$$

Ultimately, one can express g_2 in terms of g_1 and the twist-2 and twist-3 terms in the expression [40]

$$g_2(x, Q^2) = g_2^{WW}(x, Q^2) + \overline{g_2}(x, Q^2) \tag{1.93}$$

where

$$g_2^{WW}(x, Q^2) = -g_1(x, Q^2) + \int_x^1 \frac{g_1(y, Q^2)}{y} dy \tag{1.94}$$

$$\overline{g_2}(x, Q^2) = -\int_x^1 \frac{\partial}{\partial y} \left(\frac{m}{M} h_T(y, Q^2) + \xi(y, Q^2) \right) \frac{dy}{y} \tag{1.95}$$

The g_2^{WW} term includes only twist-2 contributions. This expression was derived by Wandzura and Wilczek by assuming that the d_n contributions in OPE sum rules are negligible [41]. The h_T term, often called the 'transversity', is an additional twist-2 contribution that takes into account a transverse quark spin distribution which is suppressed by $\frac{m}{M} \ll 1$ in DIS. The ξ term includes quark-gluon correlations inside the nucleon, a twist-3 contribution.

1.7 Sum Rules

1.7.1 Bjorken Sum Rule

A sum rule for the difference in polarization asymmetry in deep inelastic scattering from protons and neutrons was derived by J. D. Bjorken in 1966 from the application of chiral U(6)⊗U(6) algebra of current densities [42]:

$$\int_0^1 \left[g_1^p(x) - g_1^n(x)\right] dx = \Gamma^p - \Gamma^n = \frac{1}{6}\left|\frac{g_A}{g_V}\right|. \tag{1.96}$$

Equation (1.96) is the sum rule for $Q^2 = \infty$ which Bjorken derived without application of any QCD corrections. The theory value of the third order QCD corrected Bjorken sum rule for three quark flavors is given by:

$$\Gamma_1^p - \Gamma_1^n = \int_0^1 \left[g_1^p(x,Q^2) - g_1^n(x,Q^2)\right] dx = \frac{1}{6}\left|\frac{g_A}{g_V}\right| C_{ns} = 0.182 \pm 0.005 \tag{1.97}$$

where C_{ns} from equation (1.81) is evaluated at $Q^2 = 5$ GeV^2 using $\alpha_s(M_z^2) = 0.119 \pm 0.002$ to get $\alpha_s(5 \text{ GeV}^2) = 0.29 \pm 0.02$ for the strong coupling constant.

Past experiments have already verified the Bjorken sum rule within experimental error. E143 data at $Q_o^2 = 5$ GeV^2 measured $\Gamma_1^p - \Gamma_1^n = 0.164 \pm 0.021$, consistent with the theoretical value of 0.182 [29]. The model independent Bjorken sum rule is a fundamental test of QCD and should help us to better understand the quark spin structure of the nucleons.

1.7.2 Ellis-Jaffe Sum Rule

In the late 1960's and early 1970's, experimental verification of the Bjorken sum rule would have required data on polarized electrons scattering from polarized neutrons. Such data would not have been available for a long time. Hence, Ellis and Jaffe derived a sum rule for the asymmetry in scattering from polarized protons (or neutrons) alone [43]. They used standard quark light-cone algebra and the quark parton model assuming that only isosinglet quarks exist in the *sea* of the proton and that the spin of these sea partons are always paired in an *unpolarized quark sea.* Ellis-Jaffe is an improvement over the naive model's predictions for the integrals over g_1^p and g_1^n given in equations (1.64) and (1.65) [10]. The sum rules for predicting the spin structure functions of the proton and neutron separately without QCD corrections, where the plus sign is for the proton, the minus is for the neutron and F and D are constants from the hyperon decays, are:

$$\int_0^1 g_1^{p(n)}(x)dx = \pm\frac{1}{12}(F+D) + \frac{5}{36}(3F-D). \tag{1.98}$$

The most updated values of F and D constants were calculated assuming perfect SU(3) symmetry and using experimental measurements of g_A/g_V from the four semi-leptonic baryon decays, $n \to p$, $\Sigma^- \to n$, $\Lambda^+ \to p$ and $\Xi^- \to \Lambda$ which correspond to $F+D$, $F-D$, $F+D/3$ and $F-D/3$ couplings with the result $F = 0.467 \pm 0.0079$ and $D = 0.8039 \pm 0.0080$ [32]. with errors that assume perfect SU(3) flavor symmetry. The theoretical evaluations of the integrals over $g_1(x)$ are:

$$\int_0^1 g_1^p(x)dx = 0.1867 \pm 0.0039 \tag{1.99}$$

$$\int_0^1 g_1^n(x)dx = -0.0244 \pm 0.0031. \tag{1.100}$$

Just as with the Bjorken sum rule, the Ellis-Jaffe sum rule can be refined with non-singlet and singlet QCD corrections, C_{ns} (1.81) and $C_s(Q^2)$ (1.82), which decreases the absolute value prediction of the integrals over $g_1(x)$ for proton and neutron [44]. This can be done by assuming $\Delta s = 0$ in equations (1.70) and (1.72) which implies

$a_0 = a_8 = 3F - D$. The result is:

$$\Gamma_1^p(Q^2) = \frac{1}{36}\left[\big(3a_3 + a_8\big)C_{ns} + 4a_8C_s(Q^2)\right] = 0.163 \pm 0.004 \tag{1.101}$$

$$\Gamma_1^n(Q^2) = \frac{1}{36}\left[\big(-3a_3 + a_8\big)C_{ns} + 4a_8C_s(Q^2)\right] = -0.019 \pm 0.004 \tag{1.102}$$

$$\Gamma_1^d(Q^2) = \frac{1}{36}\left[a_8C_{ns} + 4a_8C_s(Q^2)\right] \cdot \big(1 - \frac{3}{2}\omega_D\big) = 0.067 \pm 0.006 \tag{1.103}$$

The above integrals may have an unrealistically low error as calculated here since the assumption of perfect SU(3) flavor symmetry underestimates the errors on F and D [35]. Ehrnsperger and Schäefer [45] found that SU(3) symmetry breaking effects can significantly reduce the size of F/D resulting in as much as 10-20% error on F and D. The deuteron result includes the error on the D-state probability in the deuteron $\omega_D = 0.05 \pm 0.01$.

The world measurements on $g_1(x)$ to obtain Γ^p, Γ^n and Γ^d violate the Ellis-Jaffe predictions. For example, E143 found $\Gamma^p = 0.129 \pm 0.010$, $\Gamma^n = -0.034 \pm 0.017$ and $\Gamma^d = 0.044 \pm 0.007$ [29] at $Q^2 = 5$ GeV^2.

1.7.3 Burkhardt-Cottingham Sum Rule

Using A_2 predictions from forward virtual Compton scattering dispersion relations, Burkhardt and Cottingham derived a sum rule for g_2 in the $Q^2 \to \infty$ scaling limit [46]:

$$\int_0^1 g_2^{p(d)}(x)dx = 0. \tag{1.104}$$

The Burkhardt-Cottingham sum rule cannot be derived by way of OPE, since $\Gamma_2^{(n)}$ is not defined for $n = 0$. The computation of $g_2(x)$ in perturbative QCD at order α_s

shows that it vanishes exactly at all orders in m^2/Q^2 (m = quark mass) as required by the sum rule [47].

1.8 E155 Experiment

E155 collected a large data sample, scattering polarized electrons off a polarized ammonia target to extract g_1^p and g_2^p and a lithium deuteride target to extract g_1^d and g_2^d. E155 is the most precise measurement of g_1 to date and the first high intensity electron beam experiment to use ^{6}LiD as a nuclear target. A third spectrometer at 10.5^o was constructed to measure the structure functions at even higher Q^2, in addition to the existing 2.5^o and 5.5^o spectrometers used during the E154 experimental run. The E155 data provides important information on the Q^2 dependence of the nucleon structure functions and continues to verify the Bjorken Sum Rule. The setup and deuteron results of this high precision spin structure measurement experiment is described in the ensuing chapters.

Chapter 2

Experimental Setup

The E155 DIS experiment consisted of a polarized electron beam incident on a polarized nucleon target with three independent spectrometers positioned at three different angles that detected charged particles. The spectrometers measured the path, energy and momentum of particles in order to resolve DIS electrons from background events. Special emphasis shall be placed on the description of the polarized target system since the author was directly involved in its setup and operation during the experiment.

2.1 Polarized Beam

The Stanford Linear Accelerator Center's primary experimental machine is a two-mile long linear electron accelerator. Originally proposed in 1957, construction began in 1962 and was completed in 1967 at the designed energy of 22 GeV. Since then, upgrades to the linac structure have achieved energies as high as 50 GeV.

The SLAC linac provided longitudinally polarized electrons produced by way of photo-emission from a strained-lattice GaAs crystal. These electrons were then accel-

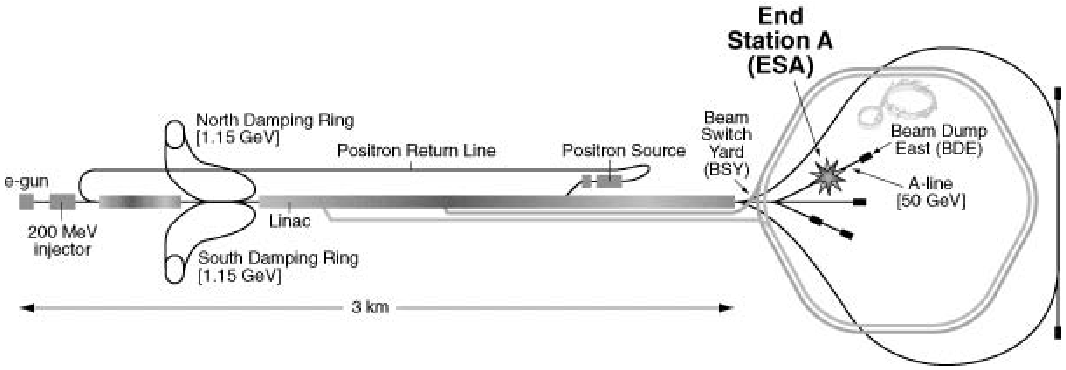

Figure 2.1: **Linac Path to End Station A** Polarized electrons were accelerated via the 2-mile long SLAC linac and directed into the experimental hall through the beam switch yard [48].

erated and steered through the 2-mile long linac and 24.5° A-bend where the polarized electron beam was ultimately delivered to the E155 polarized target in End Station A at an energy of 48.4 GeV (38.8 GeV) for longitudinal (transverse) running [figure (2.1)].

2.1.1 Source

The polarized electron source, as illustrated in figure (2.2), consisted of a system based on photo-emission of spin oriented electrons from a strained GaAs semiconductor crystal. This was achieved by shining left (σ^-) or right (σ^+) circularly polarized light onto the GaAs crystal of which the polarization of the emitted electrons was aligned parallel or anti-parallel to their direction of motion.

A flashlamp-pumped Ti-Saphire laser generated 850nm linearly polarized light which traveled through a circular polarizer, or Pockels cell, to change the light's polarization from linear to circular. The Pockels cell is an electro-optical crystal which, if an electric field is applied, induces birefringence in the crystal and changes the state of the light wave propagating through it. With the proper voltage applied,

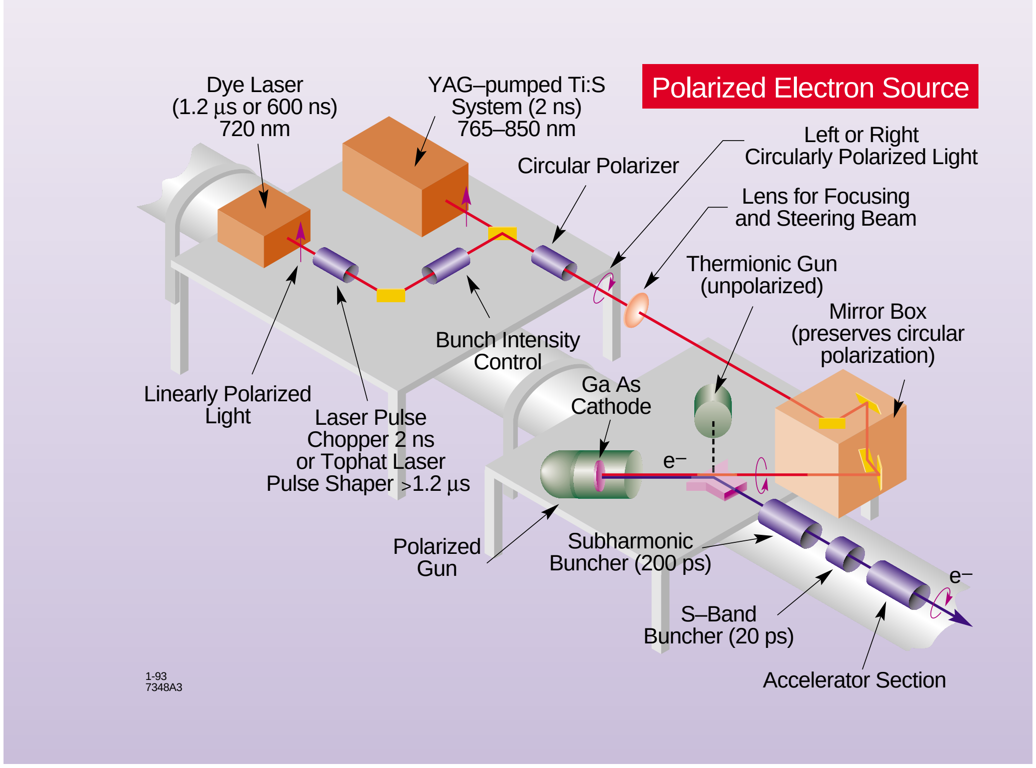

Figure 2.2: **SLAC Polarized Beam Source** Longitudinally polarized electrons were produced via photo-emission from a strained-lattice GaAs crystal. Electrons were then accelerated to 48.4 GeV (38.8 GeV) in the 2-mile long SLAC linac for longitudinal (transverse) running [49].

one can choose to change the linearly polarized light to right or left circularly polarized light. The Pockels cell allowed for rapid changing of the light's polarization in order to achieve a pseudo-random change in final electron polarization on a pulse by pulse basis.

Figure (2.3) shows the energy level diagram for GaAs. A strained GaAs crystal was used instead of the traditional unstrained GaAs crystal since one can improve the maximum polarization from 50% to 100%. When a thin layer of GaAs is grown on a GaAs$_{(1-x)}$P$_x$ substrate with a lattice spacing slightly different from that of the GaAs, the GaAs lattice spacing is slightly strained and an electric field is set up in

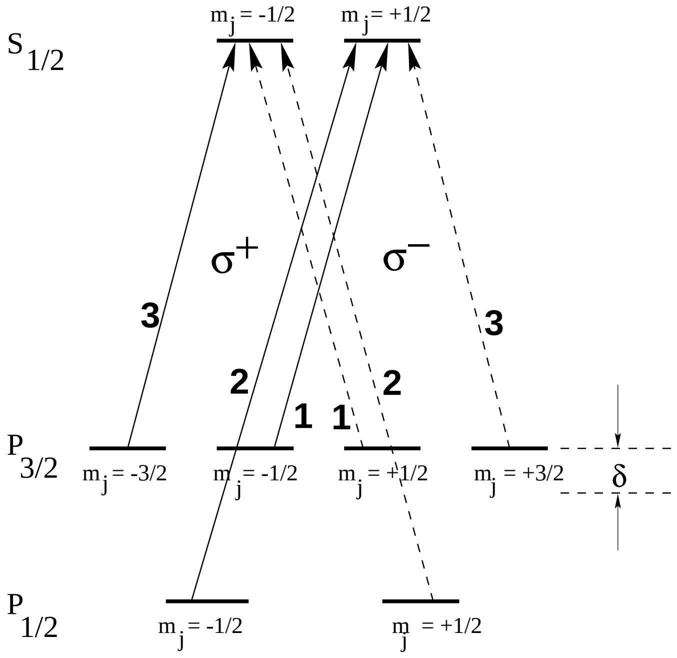

Figure 2.3: **Transition Diagram for GaAs** The transitions for σ^+ and σ^- excitations are shown for unstrained GaAs. The degeneracy in the sub-states of the $P_{3/2}$ valence band in unstrained GaAs is broken in the strained GaAs case by a downward shift in the $m_j = \pm 1/2$ levels by an amount δ. $\Delta E_{(S_{1/2}-P_{3/2})} = 1.43$ eV, $\Delta E_{(P_{3/2}-P_{1/2})} = 0.34$ eV and $\delta = 0.05$ eV.

the crystal. This field changes the degenerate levels in the $P_{3/2}$ band and allows one to optically pump each level separately using the correct laser frequency. Although the break in degeneracy increases the theoretical maximum polarization to 100%, a polarization of about 80% was achieved during E155.

For our experiment, the Ti-Sapphire laser provided 10 μs pulses onto the source crystal at 119 Hz allowing the linac injector to provide a 119 Hz main pulsed beam, where each pulse was about 300 ns in length and contained about 3.5×10^9 electrons. The injector also provided a 1 Hz higher intensity scavenger beam to allow for proper beam control via the linac feedbacks [50]. This 1 Hz beam was steered away from the beamline into a dump before entering the experimental station.

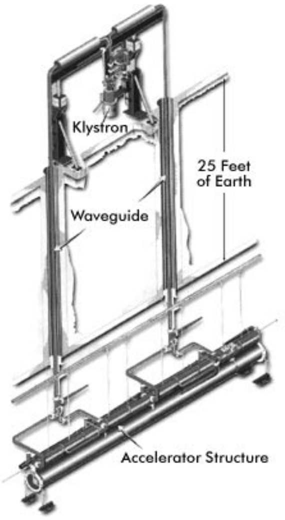

Figure 2.4: **Linac Waveguide** The above figure illustrates the underground linac structure which is fed with microwaves by way of klystrons located directly above on the ground level.

2.1.2 Linac

Figures (2.4) and (2.5) show the 2-mile long linac structure into which the polarized electrons from the source were injected and accelerated via 240 klystrons. Each klystron produced high power RF at 2.9GHz which was coupled into the beamline's copper resonant cavity structure. The RF frequency and cavity dimensions were matched to the electron speed such that the relative phases of the oscillating electric fields continuously provided an accelerating field to the beam electrons.

2.1.3 A-line

Upon reaching the end of the linac, the beam was steered 24.5° into ESA through the beam switch yard and the A-line. The switch yard had a pair of pulsed magnets that removed the 1Hz witness pulse from the main beam and directed it to a beam dump. A pair of dipoles steered the 119Hz main beam 0.5° into the A-line which consisted of

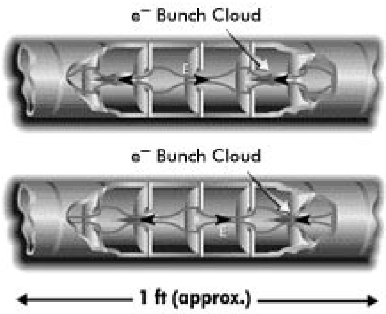

Figure 2.5: **Linac Structure** Electron bunches are accelerated through the accelerator's copper structure.

6 pairs of dipoles that each bent the beam 4.0°. An adjustable collimator sandwiched between each set of the 6 dipoles maintained the fractional energy spread of the beam to $\Delta E/E \approx 0.8\%$ FWHM. The 12 dipoles were wired in series with an identical 13th dipole which sat outside the accelerator structure next to the accelerator control center. A flip coil continuously measured the field of the reference magnet, hence the field of the A-line dipoles and hence the energy of the electron beam.

While traversing the A-line bend, the electrons lose an amount of energy ΔE by giving off synchrotron radiation equal to [51]

$$\Delta E_{sych} = \frac{2\Delta\theta_{bend}}{3}\frac{e^2}{\rho}\left(\frac{E}{m}\right)^4 \tag{2.1}$$

where $\Delta\theta_{bend}$ = angle in radians, e = electron charge, $\rho = 85.927$ m bending radius [52], E = electron energy and m = electron mass. Traversing the A-line bend also causes the electrons to experience a spin precession of

$$\Delta\theta_{prec} = \frac{E}{m}\left(\frac{g-2}{2}\right)\Delta\theta_{bend}. \tag{2.2}$$

where $(g-2)/2 \approx 0.00116$ is the anomalous magnetic moment of the electron.

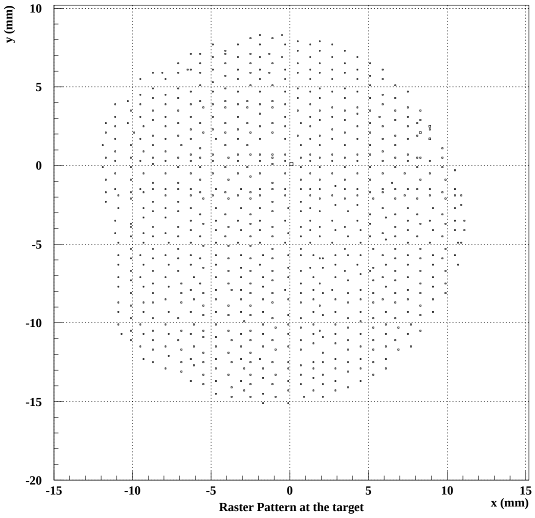

Figure 2.6: **Beam Raster Pattern** The typical pattern as seen by the foil array. Each dot represents the location of a beam pulse traversing the target volume.

In order to preserve the electron's spin orientation parallel or antiparallel to the beamline, the electrons must be allowed to precess an integer number of π radians. This was accomplished by adjusting the beam energy until $\Delta\theta_{prec} = n\pi$ radians, assuming a fixed bend of $\Delta\theta_{bend} = 24.5°$. For E155, synchrotron losses for an incident beam of 48.75 GeV (38.93 GeV) were $\Delta E \approx 400$MeV (≈ 160MeV) with a precession of 15π (12π) for longitudinal (transverse) running resulting in a beam energy at the target of 48.37 GeV (38.77 GeV) [53].

2.1.4 Beam Raster

At the experimental station entrance, a pair of Helmholtz coils varied the beam position at the target face on a spill by spill basis. The beam pulses were spread in a circular grid pattern 10mm in radius and 0.3mm in step size, a typical pattern shown in figure (2.6). The so-called *rastering* of the beam reduced the average number of e^-

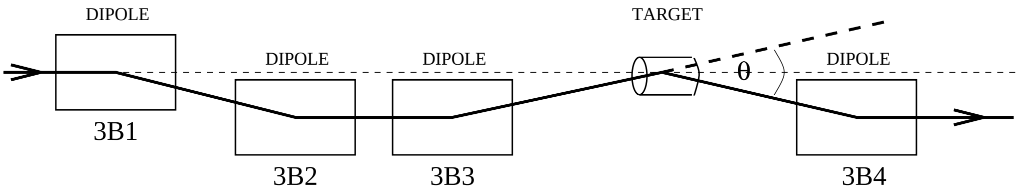

Figure 2.7: **Chicanes** Chicane system used during perpendicular mode running. The light dotted line represents the beam axis while the solid thick line represents the path taken by the unscattered beam electrons. Diagram not to scale.

deposited at a given point on the target face over time. Since the beam pulses were deposited over a larger volume, it helped decrease the effects of beam heating and radiation damage, both of which result in target depolarization.

2.1.5 Chicane

During *perpendicular mode* running, the target magnet was oriented 90° to the beamline. As a result, the beam electrons experienced a force from the target field $\vec{F}_{targ} = -e \cdot \left(\vec{v} \times \vec{b}\right)$. To compensate for this force, a collection of dipoles called a *chicane* were used to steer the beam such that the beam electrons made it through the center of the target and the unscattered electrons made it along the beamline to a water-cooled beam dump just outside the endstation. As shown in figure (2.7), three dipoles were located upstream and a fourth downstream from the target.

2.1.6 Beam Monitors

The experiment monitored the current, energy, polarization and position profile of the electron beam using toroids, dipoles, Møller detectors and foil arrays, respectively. A pair of toroids, each an iron ring wrapped with a coil of wire, measured the beam charge by detecting the current induced in the coil windings from each passing beam spill. The toroids were calibrated several times a day by passing a known current through them. The beam energy was measured by way of a flip-coil in the bore of the line-A reference magnet. The beam polarization was measured by detecting Møller scattered electrons off thin magnetized foils, described in more detail in the next section.

Beam quality was also measured by *good* and *bad* spill monitors. Each monitor consisted of a large scintillator paddle with a phototube which detected particles scattered from the beam. The good spill monitor was positioned close to the polarized target, while the bad spill was located further upstream in the alcove region, the entrance tunnel to the endstation. For each beam pulse, the monitors detected scattered particles and produced a signal which was integrated by an ADC and recorded as part of the experimental data. The same signal from each monitor was also displayed on oscilloscopes so that experimenters can visually inspect the signals in real time. A large signal at the good spill and a small signal at the bad spill indicated a properly steered and focused beam. Large signals from both monitors indicated beam scraping the beampipe or some other object upstream.

Roller screens, thin fluorescent screens which were placed in the path of the beam upstream and downstream of the target while the experiment was not taking data, gave a visual inspection of the position and spread of the beam during beam tuning. The screens glowed at the location hit by the electrons.

Downstream from the spill monitors, a foil array electronically measured the position and spread of the beam pulses. The array consisted of x and y planes of 48 thin brass foil strips, separated by 1 mm. The spacing of the foils allowed for a position and spread determination of the beam spot within ±1 mm.

2.2 Møller Polarimeter

Spin dependent elastic electron-electron scattering (Møller scattering) is a commonly used technique for beam polarization measurements at energies in the MeV and GeV range [54]. The longitudinal electron beam polarization P_b for E155 was measured by way of Møller scattering, in which beam electrons are scattered off polarized atomic electrons in ferromagnetic foil targets. The scattered electrons were detected via two detector systems, a single-arm detector that detected only one of the final state electrons and a double-arm detector that detected both electrons in coincidence, a method that considerably reduces background since we are more certain we are detecting Møller scattered electrons.

The fact that the beam and Møller target electrons are polarized introduces an asymmetry in the scattering cross-section which for longitudinally polarized electrons scattering off atomic electrons polarized (anti-)parallel to the beam is given by

$$A_{zz} = -\left[\frac{(7+\cos^2\theta_{cm})\sin^2\theta_{cm}}{(3+\cos^2\theta_{cm})^2}\right]. \tag{2.3}$$

From measuring the asymmetry between (anti-)parallel electron rates

$$A_m = \left(\frac{\sigma^{\uparrow\uparrow}-\sigma^{\uparrow\downarrow}}{\sigma^{\uparrow\uparrow}+\sigma^{\uparrow\downarrow}}\right), \tag{2.4}$$

one can determine the beam polarization given a known target polarization P_{foil} via

$$P_b = \frac{A_m}{A_{zz}P_{foil}}. \tag{2.5}$$

The theoretical asymmetry is largest at a center of mass scattering angle of $\theta_{cm} = 90°$. At this angle, the unpolarized cross section is 0.179 b/sr and A_{zz} = -7/9. The typical measured asymmetry $A_m \sim 0.05$ assuming $P_{foil} \sim 0.08$ and $P_b \sim 0.80$ [55].

The two polarimeters shared a common target. Six polarized foil targets of thicknesses 20 μm, 30 μm, 40 μm and 154 μm were located upstream from the polarized nucleon target and were made of permendur (49% Fe, 49% Co and 2% V). The foils were moved in and out of position in the beamline via a remote control system. A ±100 gauss Helmholtz pair provided the magnetizing field in order to polarize the unpaired atomic electrons in the foils. The coil polarity was flipped between Møller data taking runs to minimize systematic errors. The foil electron polarization is related to the bulk magnetization of the material and was determined before the experiment.

About 10 m downstream of the foils was a 25 radiation length tungsten mask used to define the azimuthal and vertical acceptance of the polarimeters. The mask had a 45.7 mm hole in the center to allow the unscattered beam to pass unblocked, and two triangular shaped holes on either end, top and bottom, to allow only vertically scattered electrons to pass. A dipole magnet B0 set at 1050A deflected the vertically scattered electrons according to energy in the horizontal plane. This was done to direct the Møller scattered electrons away from the beamline and to keep them on the single-arm and double-arm detector packages. The B0 magnet contained an iron septum along the beamline to allow the beam electrons to pass straight through to the dump without being deflected by the dipole magnetic field.

The angle (mask) and energy (B0 magnet) selected scattered electrons traveled through He-gas boxes to reduce the chances of re-scattering before they were detected further downstream by both the single-arm and double-arm detectors. The single-arm used segmented silicon strip detectors while the double-arm used two sets of lead glass blocks.

2.3 Polarized Target

A solid dynamically polarized nucleon target was chosen for this experiment, since the collaboration required a nucleon target that could achieve and maintain a high nucleon polarization in a high intensity electron beam [56]. The E155 target was essentially the same as the one used in E143. The dynamic nuclear polarization (DNP) method was used to enhance the spin polarization of the protons in $^{15}NH_3$ and deuterons in ^6LiD. This was achieved by way of a 5.1T Oxford Instruments super-conducting Helmholtz pair magnet, a ^4He evaporation refrigerator that reached temperatures below 1K and a Varian extended interaction oscillator tube (EIO tube) that delivered 140 GHz microwaves to the target cells in order to drive the DNP process (about 28 GHz/T). An NMR system was used to measure the nucleon polarization.

2.3.1 Definition of Polarization

The polarization of a collection of nuclear spins I is given by

$$\boldsymbol{P} = \frac{< \boldsymbol{I}_z >}{I}. \tag{2.6}$$

E155 made use of proton and deuteron targets, where $I = \frac{1}{2}$ for protons and $I = 1$ for deuterons. In the case of the proton, there are two spin sub-levels $m_I = \pm\frac{1}{2}$. Hence, the *relative* populations or *polarization* can be denoted simply by the difference in populations over the total population [57]

$$P_{\mathrm{spin}\,\frac{1}{2}} = \frac{N_{+\frac{1}{2}} - N_{-\frac{1}{2}}}{N_{+\frac{1}{2}} + N_{-\frac{1}{2}}}. \tag{2.7}$$

In the case of the deuteron, there are three spin sub-levels whose populations can be fully specified by way of the two polarization parameters, *vector* and *tensor* polarizations. Equation (2.6) for the deuteron is known as the vector polarization. Specifically, the vector polarization can be denoted by

$$P_{\text{spin1}} = \frac{N_{+1} - N_{-1}}{N_{+1} + N_0 + N_{-1}} \tag{2.8}$$

the ratio of the difference in $m_I = \pm 1$ populations over the total population of all three sub-levels. The tensor polarization or *alignment* is defined by

$$A = \frac{< 3I_z^2 - I(I+1) >}{I^2} \tag{2.9}$$

$$A = 1 - 3\frac{N_0}{N_{+1} + N_0 + N_{-1}} \tag{2.10}$$

where (2.10) is the expression for spin 1 particles. The vector polarization ranges between -1 and +1, while the tensor polarization ranges between -2 and +1. If one assumes a Boltzmann distribution between spin sub-levels, the relationship between tensor and vector polarizations is given by

$$A = 2 - \sqrt{4 - 3P^2}. \tag{2.11}$$

Normally the tensor polarization is calculated from the measured vector polarization [58].

2.3.2 Dynamic Nuclear Polarization

Dynamic nuclear polarization (DNP) refers to the use of resonant microwave energy to help orient nuclear spins which are coupled with electron spins in the target material lattice. The ingredients needed to carry out DNP include the target material that is to be polarized, paramagnetic centers in the target material, a low temperature, a high magnetic field and microwave energy to excite spin state transitions, and a means to measure the enhanced spin populations.

Spin-1/2 Species

The following describes the theory for orienting proton spins or any other spin-1/2 species nucleon. Imagine the protons as a collection of identical nuclei fixed in the crystal lattice of ammonia with their spins oriented randomly. An external magnetic field **B** would orient their magnetic moments via a nuclear Zeeman interaction where the Hamiltonian can be given by [59]

$$H_p = -\boldsymbol{\mu_p} \cdot \mathbf{B}. \tag{2.12}$$

This interaction creates two energy levels, $E_{+\frac{1}{2}} = -\mu_p B$ and $E_{-\frac{1}{2}} = \mu_p B$ spaced apart by $\Delta E = 2\mu_p B$. The spins behave according to Maxwell-Boltzmann statistics, where for a given spin s, its population is given by

$$P_s = e^{-\mu B/kT} \tag{2.13}$$

where μ is the magnetic moment of the spin species, B is the magnetic field, k is Boltzmann's constant and T is the temperature. The lower energy state ($m = +\frac{1}{2}$) is slightly more populated than the higher state ($m = -\frac{1}{2}$) at the temperature and magnetic field of our target system, giving about 0.5% proton polarization at $B =$ 5T and $T =$ 1K [see table (2.8) for actual thermal equilibrium (TE) polarizations]. Section (2.3.10) contains more information on TE polarization.

By decreasing the temperature and increasing the external magnetic field, it is possible to enhance the polarization. Temperatures of a few millikelvin and magnetic fields > 10T are needed to obtain reasonable polarizations. This is called a *statically oriented* nuclear system. Targets that use this principle are *brute force* and were first proposed for frozen HD in 1967 [60].

Paramagnetic ions, which are localized free electrons whose spins couple with proton spins, are required to *dynamically orient* the target nucleons. Microwave energy is supplied to the target material in order to excite specific spin state transitions that help populate a preferred proton spin orientation. These paramagnetic centers are provided by several methods, one being the *pre-irradiation* of the target material. In the presence of external magnetic field, two energy levels are formed with a separation of $\Delta E = 2\mu_e B$. The TE polarization of the electrons is calculated the same way as for the proton. At the E155 target temperature and magnetic field, the electrons are nearly 100% polarized.

The Hamiltonian for the electron-nucleon spin coupled system is

$$H = H_e + H_p + H_{int} = -\boldsymbol{\mu_e} \cdot \mathbf{B} - \boldsymbol{\mu_p} \cdot \mathbf{B} + H_{int} \tag{2.14}$$

where μ_e is the electron magnetic moment, μ_p is the proton (nucleon) magnetic moment and H_{int} is the interaction Hamiltonian between the two spins.

The coupled system splits into four Zeeman energy levels, as shown in figure (2.8). Without the H_{int} term, the only transitions allowed are ones with a change in energy equal to $\Delta E_e = 2\mu_e B$ or $\Delta E_p = 2\mu_p B$. Transitions with $\Delta E_{e\pm p} = 2(\mu_e B \pm \mu_p B)$, represented by dashed and dotted lines in figure (2.8), are forbidden due to dipole selection rules. With the H_{int} term, the $\Delta E_{e\pm p}$ transitions are allowed, but have a smaller probability than the ΔE_e and ΔE_p transitions by a factor of about 10^{-3} [61].

The electron-proton spin interaction allowed for populating a specific proton spin

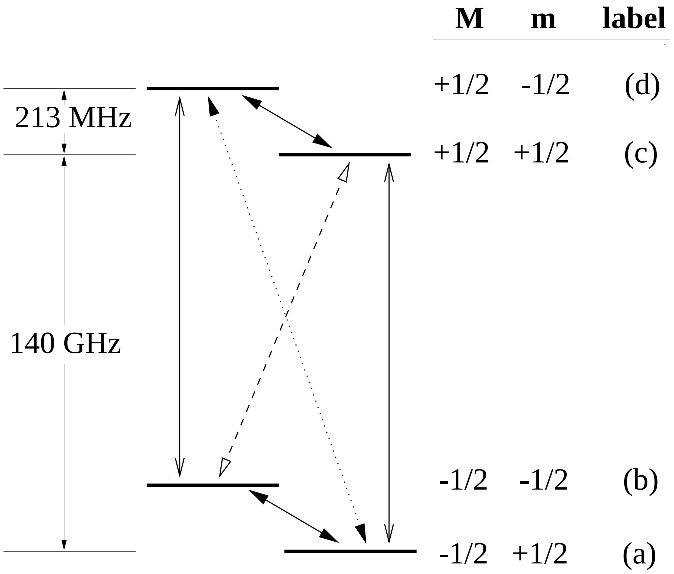

Figure 2.8: **Electron-Proton Spin Coupled System Energy Levels** Energy level diagram for the electron-proton spin coupled system in the presence of a 5T magnetic field. The energy spacing between states **a** $\rightleftharpoons$ **b**, **c** $\rightleftharpoons$ **d** is given by $2\mu_p B$ (213MHz) and for **a** $\rightleftharpoons$ **c**, **b** $\rightleftharpoons$ **d** is given by $2\mu_e B$ (140GHz).

orientation by exposing the material to microwaves with an energy of $2(\mu_e B \pm \mu_p B)$. Transitions were excited where *both* electron and proton spins were flipped. The relaxation time for the electron spin is much shorter than for the proton spin; therefore, the $\Delta E_e = 2\mu_e B$ relaxation transition is favored, where only the electron spin flips and the proton spin remains in the previous excited state orientation. Now the system is in a preferred lower energy state where the microwave energy is not matched to any transitions possible from that level. Hence, we've accomplished flipping the proton spin to a desired orientation. Microwaves with energy $2(\mu_e B - \mu_p B)$ were used for *positive* enhancement (spin-up protons) while those with energy $2(\mu_e B + \mu_p B)$ were used for *negative* enhancement (spin-down protons). Figure (2.8) outlines the steps required for positive enhancement. Microwaves of frequency 140GHz–213MHz excite the **b** $\longrightarrow$ **c** transition. Then the system relaxes through the **c** $\longrightarrow$ **a** transition.

The flipped proton spin then flops back to its original orientation by transferring its spin to a nearby proton. Then the flip-flop continues as a domino effect diffusing the spin through the target material. The *flip-flop* mechanism is known as *spin diffusion.* This process continues as long as the target material is exposed to microwaves of the proper energy.

The large difference in relaxation rates for electron and proton is the key to DNP's mechanism. The relaxation time for the electron spin is very short due to spin-lattice coupling between the electrons. The electron magnetic moment is much larger than that of the proton. Therefore, the electron prefers to reorient itself anti-parallel with the magnetic field direction. On the other hand, the relaxation time for the proton spin is very long due to a very weak spin-lattice coupling between protons at low temperatures and the proton's small magnetic moment.

The *dynamic nuclear polarization* process requires an electron spin coupled with a proton spin and occurs only near the paramagnetic centers in the material. Since these centers make up a *dilute* system, DNP is not the process alone that provides significant enhanced polarizations. The key to attaining appreciable polarizations relies on the diffusion of the proton spin through the target material via spin diffusion. Each time we flip the spin of a proton, that proton can transfer its spin state to a neighboring proton by a proton-proton spin coupling or flip-flop mechanism. Once the original proton is back in the original spin state, it's ready to be excited once again by microwaves, repeating the process. Eventually, the preferred spin orientation is diffused throughout the material.

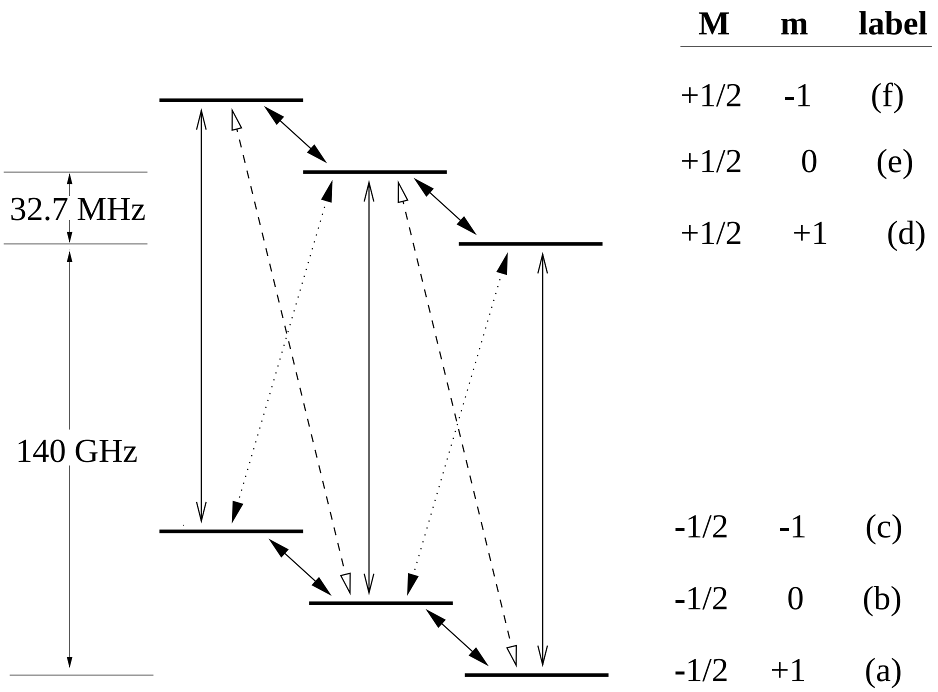

Figure 2.9: **Electron-Deuteron Spin Coupled System Energy Levels** Energy level diagram for the electron-deuteron coupled spin system in the presence of a 5T magnetic field. The energy spacing between states **a** $\rightleftharpoons$ **b**, **b** $\rightleftharpoons$ **c**, **d** $\rightleftharpoons$ **e**, **e** $\rightleftharpoons$ **f** is given by $\mu_d B$ (32.7MHz) and for **a** $\rightleftharpoons$ **d**, **b** $\rightleftharpoons$ **e**, **c** $\rightleftharpoons$ **f** is given by $2\mu_e B$ (140GHz) [62].

Spin-1 Species

The main differences between DNP for proton versus deuteron can be discussed as follows. The deuteron is a spin-1 nucleon with a magnetic moment that is about three times smaller than the proton magnetic moment. The interaction between deuteron and magnetic field results in a three level Zeeman splitting with an energy gap that is more than six times smaller than that for the proton in a 5T field.

A similar approach is used to populate one of the deuteron spin states $m = \pm 1$. Figure (2.9) shows the electron-deuteron coupled spin system. For positive enhancement, one delivers 140GHz–32.7MHz microwaves to the target material which excites the **c** $\longrightarrow$ **e** or **b** $\longrightarrow$ **d** transition. Then the system relaxes through the **e**

material	**dopant**	***f***	P_1	P_2	P_6	**B (Tesla)**	**T (Kelvin)**
$^{14}NH_3$	irradiation	0.18	0.96			5.0	1
			0.66			2.5	0.5
$^{15}NH_3$	irradiation	0.17	0.96			5.0	1
$^{14}ND_3$	irradiation	0.30		0.49		2.5	0.20
$^{15}ND_3$	irradiation	0.29		0.42		5.0	1.05
^{6}LiD	irradiation	0.50		0.32	0.40	2.5	0.25

Table 2.1: **Dilution and Polarization Characteristics of Some Materials** The fourth thru sixth columns indicate typical maximum polarizations that have been achieved with that material, temperature and magnetic field [56, 63].

$\longrightarrow$ **b** and **d** $\longrightarrow$ **a** transition. Effectively the spins of $m = -1$ go to $m = 0$, then $m = 0$ changes to $m = +1$. The flipped deuteron spin then transfers its spin through spin diffusion.

2.3.3 Target Material

Important properties necessary for a good polarized target material consist of a large proton or deuteron content, high polarization, fast build up time, type and degree of doping, good radiation resistance and low presence of other polarizable nuclei. Both ammonia and lithium deuteride have reasonable dilution factors, high polarization capabilities and have good resistance to radiation. Both materials must be radiation doped to facilitate DNP. When placed in the electron beam, additional radicals are created by the radiation which serve to degrade the material's polarization performance. With increased radical density, the relaxation processes are affected, shortening the nucleon relaxation time and lowering the polarization. For both materials, the polarizability is recoverable by annealing [56], a process where the $^{15}NH_3$ (^6LiD) material is warmed from ∼1K to ∼80K (∼180K). Heating the target material allows the beam created radicals to recombine, improving the doping situation.

% by weight	element	g/cm^2
10.7	^{1}H	0.26501
53.3	^{15}N	1.32507
25.1	^{4}He	0.62338
9.3	^{27}Al	0.23246
0.8	^{14}N	0.01935
0.6	^{64}Cu	0.01595
0.2	^{59}Ni	0.00666

Table 2.2: **Typical Proton Target Composition**

% by weight	element	g/cm^2
17.9	^{2}H	0.32233
53.5	^{6}Li	0.96699
14.4	^{4}He	0.25965
10.7	^{27}Al	0.19374
2.4	^{16}O	0.04400
1.1	^{14}N	0.01935

Table 2.3: **Typical Deuteron Target Composition**

SLAC experiment E143 used $^{15}NH_3$ and $^{15}ND_3$ as proton and deuteron targets, respectively. However, the E155 collaboration decided to use ^{6}LiD as the deuteron target for its experiment, since the effective dilution factor, the fraction of polarizable nucleons of interest, is considerably larger for ^{6}LiD than for $^{15}ND_3$ [63]. The naive dilution factor for ^{6}LiD is 0.50 as compared to 0.29 for $^{15}ND_3$. See section (3.3.6) for a detailed explanation of the dilution correction factor. Table (2.1) lists dilution factors for some commonly used solid polarized target materials. E155 is the first time ^{6}LiD was used as a polarized deuteron target in a high energy electron beam experiment.

The total target compositions included the aluminum (^{27}Al) vacuum windows upstream and downstream of the polarized target cell, liquid ^{4}He, $^{15}NH_3$ or ^{6}LiD polarized target material, air (^{14}N) and polyethylene (C_2H_4). The proton and deuteron

% by weight	element	g/cm^2
60.6	^{12}C	1.51593
30.9	^{4}He	0.77476
7.7	^{27}Al	0.19374
0.8	^{14}N	0.01935

Table 2.4: **Typical Carbon Target Composition**

% by weight	element	g/cm^2
56.4	^{9}Be	1.27650
34.2	^{4}He	0.77476
8.6	^{27}Al	0.19374
0.8	^{14}N	0.01935

Table 2.5: **Typical Beryllium Target Composition**

polarized target compositions are described in tables (2.2) and (2.3), as well as the carbon and beryllium solid target compositions in tables (2.4) and (2.5). Carbon and beryllium were used for spectrometer calibration and polarized target thickness determination [section (3.3.7)].

2.3.4 Pre-irradiation of Target Material

Paramagnetic centers were introduced in the target material to provide the mechanism to transfer spin to the nucleons. These centers are ions which have a net angular momentum from unpaired electrons. The magnetic moment of the odd electron will align anti-parallel to an applied magnetic field. The *locally free electrons* are nearly 100% polarized at 5T and 1K. This electron spin polarization is transferred to the appropriate nucleons in the material via DNP.

A dilute system of paramagnetic centers was introduced into the ^{15}NH$_3$ and ^{6}LiD material by way of *pre-irradiation*, with a density of $\approx 10^{19}$centers/cm^3 [64]. Pre-irradiation was achieved by exposing the target material to a low energy electron beam, such as was carried out by the E155 target group at the 30MeV electron linac of the SUNSHINE facility at Stanford University. The electrons passed through the target material and knocked out some protons. This created $^{15}NH_2^-$ radicals where the extra electrons served as the paramagnetic centers while the material was kept cold. Therefore, irradiations were done under a liquid cryogen such as argon at 90K. Typically, our E155 $^{15}NH_3$ material was exposed to $1.0 \times 10^{17} e^-/cm^2$ with 30 MeV electrons at SUNSHINE, while two target loads consisted of E143 $^{15}NH_3$ material with a dose of $2.0 \times 10^{16} e^-/cm^2$ and $4.0 \times 10^{16} e^-/cm^2$ with 65MeV electrons at the Naval Postgraduate School in Monterey California. All the ^6LiD material was exposed from $1 \times 10^{17} e^-/cm^2$ to $5 \times 10^{17} e^-/cm^2$ to 30MeV electrons at SUNSHINE.

2.3.5 Magnet

The experiment used a 5.1T super-conducting Helmholtz pair coil manufactured by Oxford Instruments. The basic magnet cryostat, coil package and high power helium-4 evaporation refrigerator design was based on the University of Michigan solid polarized proton target system [56]. Some important properties that were considered when designing the superconducting magnet include coil material, coil bore clearance, field homogeneity and stability, mechanical stress and thermal stability, lead design, quench protection and power supply.

The magnet coils were immersed in a 4 K liquid helium (LHe) bath with a 1.5 W evaporation refrigerator oriented vertically along the center axis of the cryostat assembly as in figure (2.10). The coils were wound with a multi-filamentary superconducting wire made of niobium titanium (NbTi) filaments surrounded by a stabilizing matrix of copper [65]. The multi-filament property of the coil material allowed for redistribution of currents in case there was a local change in flux or if a short length

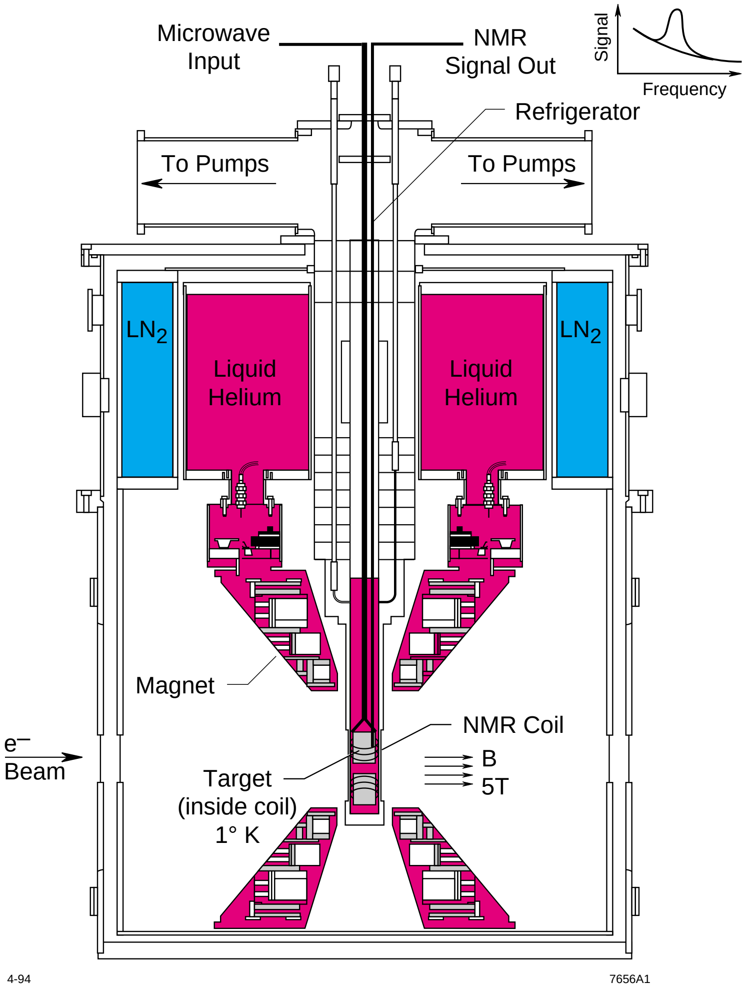

Figure 2.10: **Polarized Target Magnet & Refrigerator** The E155 target utilized an Oxford Instruments super-conducting split-Helmholtz coil magnet that ran at 5.004T and a ^{4}He evaporation refrigerator that cooled to about 1K with beam.

of NbTi became normal. Typically, NbTi alloys have a critical temperature of about $T_c \approx 10$K, hence LHe was the cryogen of choice to maintain the super-conducting wire at 4.2K [66]. Clearance for incoming and outgoing particles was a 100° cone in the bore axis (longitudinal running) and 34° along the split axis in a horizontal plane (transverse running) with a vertical aperture of 50°. The magnet design allowed for a 80 mm x 80 mm vertical access for the bottom *tail-piece* section of the refrigerator. The field was homogeneous to 1 part in 10^4 over a 20 mm diameter by 20 mm long cylindrical area. Field stability was 1 part in 10^6 per hour.

The magnet included a *quench protection* circuit which consisted of resistors and diodes that could help prevent large voltage drops from forming between the sets of coil windings in case the coils go normal.

Typical operation of the magnet system required an isolation vacuum, a cold LN_2 shield and cold LHe/magnet can that kept the coils at 4.2 K. The following describes the cool-down procedure. The cryostat isolation vacuum was pumped with a mechanical-turbo pump station. Once a vacuum $\sim 10^{-5}$ torr at room temperature was attained, the cryostat was pre-cooled by filling both the LN_2 shield reservoir and the LHe magnet can with LN_2. After the coils came to thermal equilibrium with the LN_2 bath, the LN_2 and any nitrogen gas were forced out by pressurizing the can with He gas. The magnet can was filled with LHe after making sure that no nitrogen was left. The coil temperature was maintained at 4.2K. Then, the main magnet coil was energized to 77 A by a 10 V power supply. During normal target operations, the magnet was placed into persistent mode for added stability, a state in which the coil package was a closed circuit and disconnected from the power supply.

2.3.6 Refrigerator

The target used a ^{4}He evaporation refrigerator to cool and maintain the target temperature in the range 1K-2K. The refrigerator operated by pumping on the surface of a LHe bath in the tailpiece region of the target thus lowering the vapor pressure above the liquid which decreased its temperature [67]. Figure (2.11) illustrates the main components of the refrigerator.

During the typical operation of the refrigerator, LHe was delivered from the magnet reservoir to the refrigerator separator via a transfer-line coupled to the LHe input port. The separator can contained a sintered bronze wall that had a low (high) impedance for helium liquid (gas), which served to separate the liquid from gas and deliver mostly LHe to the target. Also, the separator provided a 4K heat sink for the target insert [figure (2.12) and (2.13)] which held the target materials in the refrigerator space. The helium gas was removed from the separator by pumping it through an upper set of radiation baffles by way of a mechanical "separator" pump. The separator provided a reservoir of LHe whose delivery to the target region was controlled by the run and bypass valves. With the run valve open, LHe was allowed to flow through a heat exchanger and collect in an aluminum cylinder called the "tailpiece" where the beam windows and targets were situated. The liquid level in the tailpiece was kept full by adjusting the run valve. A vapor flow was established in the main refrigerator space and through the holes of both sets of heat-exchange baffles by pumping on the surface of the LHe bath in the tailpiece with a set of large Roots blowers. This "main" vapor flow cooled the baffles as the cold vapor expanded and absorbed heat on its way out of the refrigerator via the main pump-out assembly. By adjusting the "main" and "separator" flows, an operating mode was established which provided cold LHe to the tailpiece and maintained the temperature $\sim$1K at $\sim$1W.

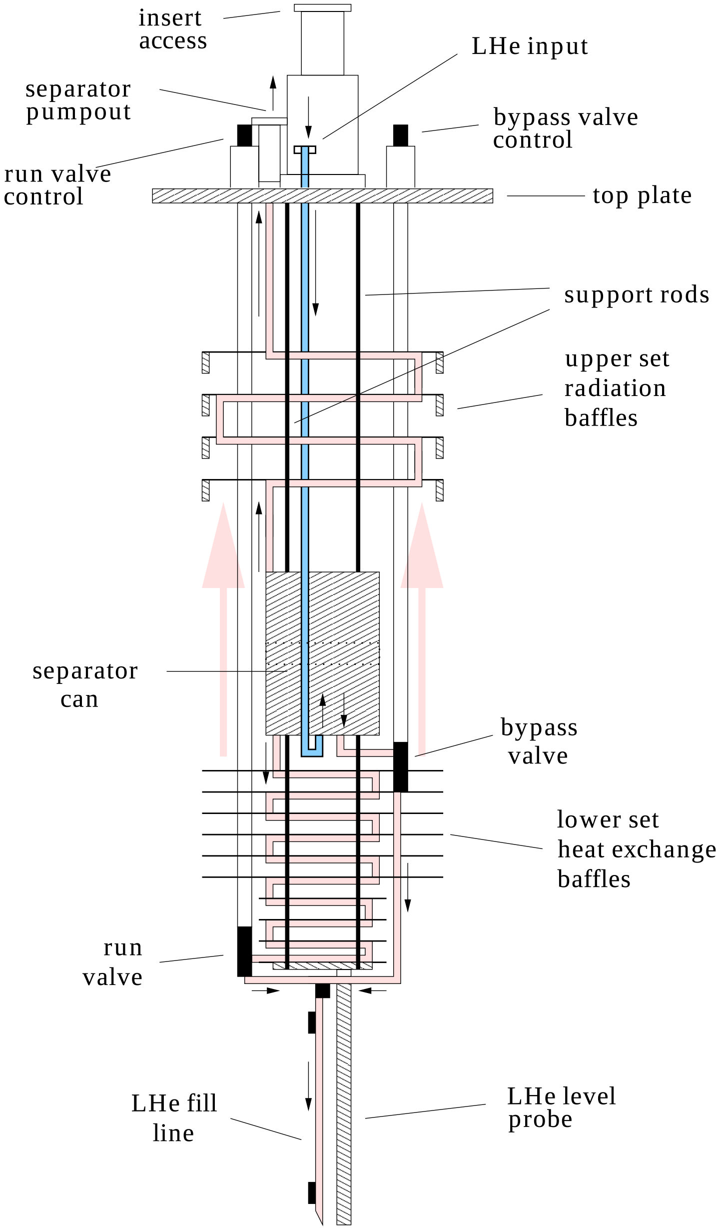

Figure 2.11: **Target ^{4}He Refrigerator** The vapor pressure above the pool of LHe in the "tailpiece" region is lowered by pumping on it with a collection of Roots blowers thus reducing the temperature of the target. The small black arrows indicate the direction of LHe flow through the various copper and stainless refrigerator tubing, while the large lightly shaded arrows show the direction of the evaporating He gas within the refrigerator space. Drawing not to scale.

2.3.7 Target Insert

The E155 polarized target utilized four inserts, each of which was five feet long and held the targets within the refrigerator LHe bath. The inserts served as a means to hold the target material in the target magnetic field and correct location in the beamline and to easily install and remove the targets from the low temperature environment. Figures (2.12) and (2.13) show a slice of the insert.

The insert was constructed with materials of favorable thermal conduction and magnetic properties. Care was taken in the design to keep heat leaks into the refrigerator space at a minimum. Such heat leaks involve thermal conduction between the top of the target cryostat at 300K and the pool of LHe in the tailpiece section at 1K. Only non-magnetic materials were used such as stainless steel, copper, copper-nickel, beryllium-copper and nylon, since any small ferromagnetic parts would compromise the uniformity of the 5T magnetic field. Stainless steel was used where thermal conduction barriers were necessary. Stainless 316 was used whenever possible, since the more common stainless 304 could become slightly magnetic when welded and then exposed to an external magnetic field. The 4K heat-sink of the insert was constructed of copper because of its high thermal conductivity. The heat sink was surrounded by the refrigerator separator which collected and delivered LHe to the target space. Also, the heat sink provided a heat intercept between the upper and lower halves of the refrigerator center bore. Copper baffles between the top plate and heat-sink and between the heat-sink and target ladder acted as barriers as well. Precision Tube brand 70/30 copper nickel tubing of $\frac{3}{16}$inch O.D. and 0.010" wall was used as waveguide which ran down the entire length of the insert. Precision Tube brand coaxial-cable with beryllium-copper outer conductor, solid Teflon dielectric and copper wire center conductor was used as part of the transmission line between the Q-meters and coils

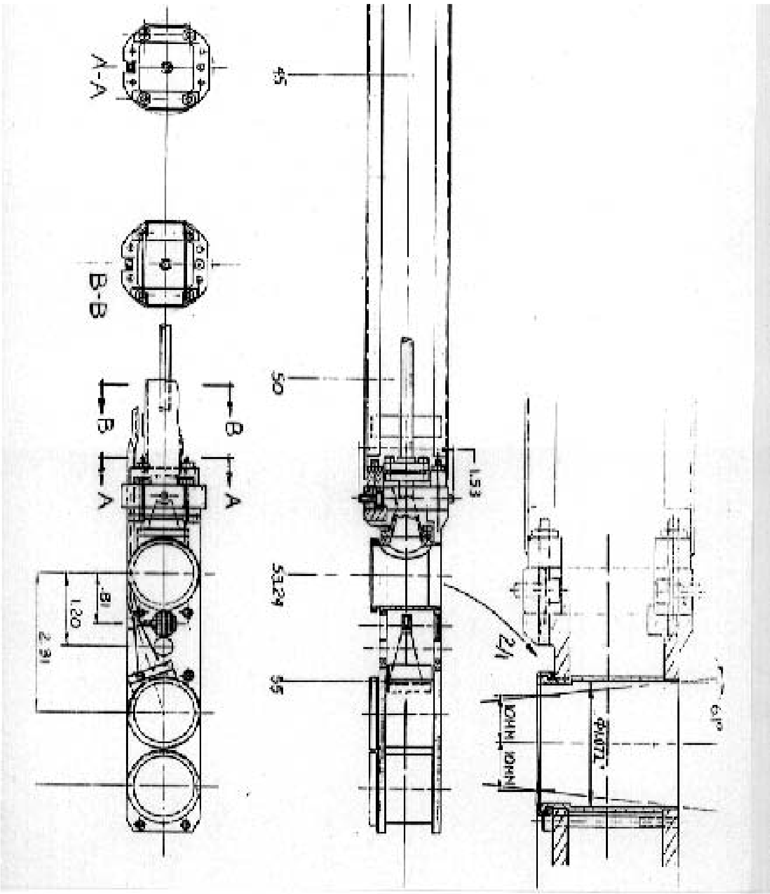

Figure 2.12: **Target Insert Assembly** Inserts were constructed to hold our cryogenic polarized targets. The inserts contained the transmission lines and the inductive coil for measuring the target polarization, waveguides and horns to deliver 140GHz microwaves to facilitate DNP and instrumentation that monitored the target temperature and position.

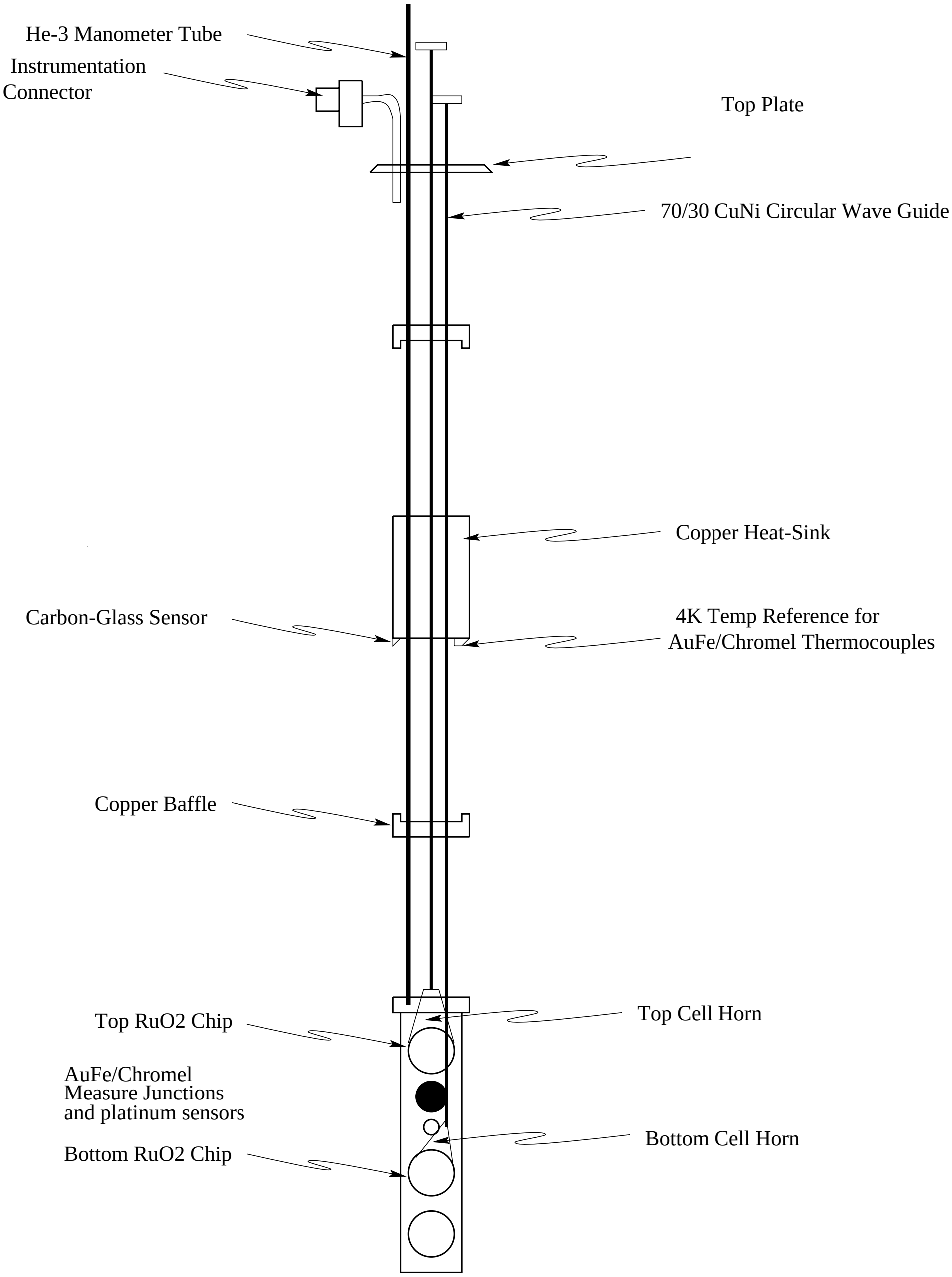

Figure 2.13: **Target Insert Instrumentation** Resistors, thermocouples and vapor pressure manometers were used to monitor the temperature of the insert and targets. The top and bottom cells held the polarized targets while the lowest cell held ^{9}Be or ^{12}C solid disks. Drawing not to scale.

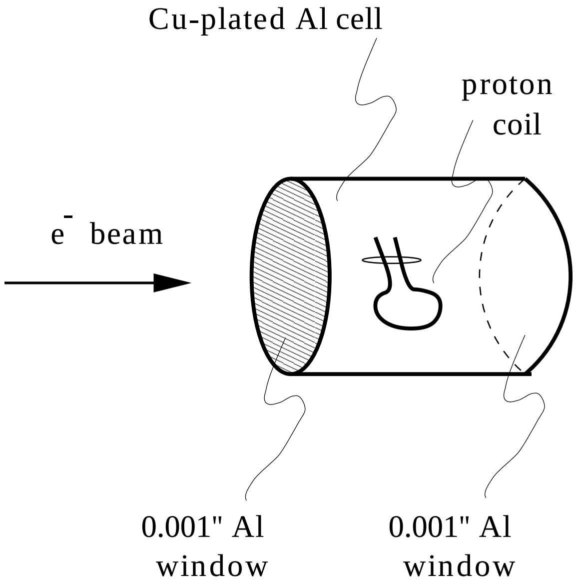

Figure 2.14: **Target Cell with Proton NMR Coil** The 3 cm long by 1 inch diameter cylindrical target cell with the single loop CuNi coil used for measuring the proton polarization. Drawing not to scale.

for the NMR LCR circuit used to measure the target polarization. Beryllium-copper has poor thermal conduction properties and is non-magnetic.

In order from top to bottom, the target ladder structure consisted of five locations: upper target cell, solid target, hole, lower target cell and dummy target cell. The two target cells, which were fed by microwave horns, were used to hold and polarize the proton and deuteron target materials. CuNi tubing and copper-plated aluminum wire were used as the NMR coil material. Various coil configurations were used depending on the nucleon polarization being measured. A straight or single loop coil in the horizontal plane of the cell, as in figure (2.14), was used to measure the proton signal. A four turn loop, as in figure (2.15), was used in the deuteron case. The coils were embedded in the target material which were held inside copper-plated aluminum cylinders with thin aluminum windows on the either end to allow beam access. The dummy cavity contained a carbon (beryllium) solid target disk of known thickness,

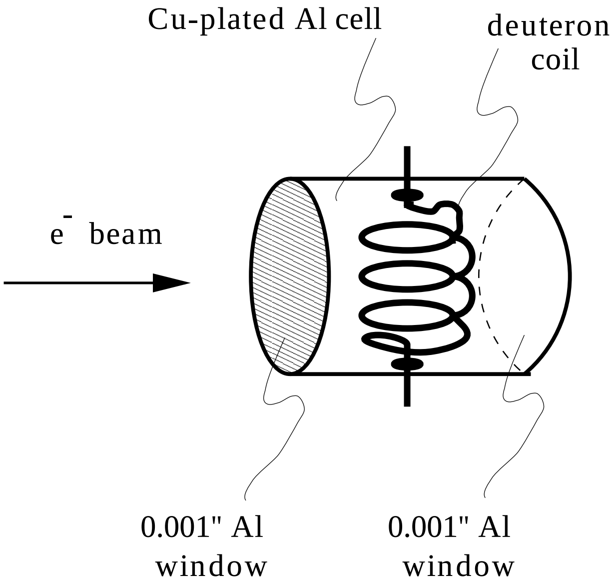

Figure 2.15: **Target Cell with Deuteron NMR Coil** The 3 cm long by 1 inch diameter cylindrical target cell with the four-turn copper-plated aluminum wire coil used for measuring the deuteron polarization. Drawing not to scale.

while the small solid target was of the counterpart beryllium (carbon) material. The solid targets and hole were used for rate, target thickness and spectrometer calibration studies.

Various resistors and vapor pressure manometers monitored the temperature of various parts of the insert and the target material. Rated at 1%, RuO_2 chip resistors monitored the target cavity temperature. At room temperature, the RuO_2 resistance was about 1kΩ, while at 1K it was about 2kΩ. Although these chip resistors could be calibrated to measure temperature within a couple of percent, the more accurate vapor pressure manometers were used to measure the actual target temperature. A ^{3}He vapor pressure manometer system, with an Edwards model 570A Barocel Absolute Pressure Sensor head rated at 100 torr full scale, was placed near the targets in the LHe bath via the insert. A ^{4}He manometer monitored the He-gas pressure in the refrigerator space. Both manometers gave temperature information from the pressure measurement using standard helium pressure versus temperature curves.

The inserts also helped perform target anneals, a procedure to regain the polarizability of the targets by warming up ^{15}NH$_3$ (^{6}LiD) to ∼80K (∼180K) for ∼5 minutes after receiving $\sim 10^{16}e^-$ from the beam. During an anneal, all the LHe in the tailpiece was boiled away via a 40Ω heater wire wrapped around each target cell. After all the gas was pumped away, one could not determine the target temperature by way of the helium vapor pressure measurements. Therefore, platinum resistors and AuFe/Chromel thermocouples were used to monitor the target cavity temperature locally during the anneal warm-up and cool-down of the target. The AuFe/Chromel thermocouple measuring junction was placed inside the target cavity while the reference junction was placed at the 4K heat-sink. The heat-sink temperature fluctuated according to refrigerator operating conditions, hence there was no stable reference temperature. Therefore, a calibrated carbon-glass sensor supplied by LakeShore Cryotronics was used to monitor the heat-sink temperature so that a proper reference temperature can be used to calculate the actual target cavity temperature via the thermocouple system. The platinum resistors were used as an alternative, since their standard resistance versus temperature relationship was well known. Experience during E143 and E155 showed that the AuFe/Chromel thermocouples were more difficult to use successfully than the platinum resistors.

2.3.8 Microwaves

The target utilized an extended interaction oscillator (EIO) tube as the source for 140GHz microwaves. The tubes were supplied by the Electron Devices Division of Varian, Canada (now CPI, Canada). E155 used a Varian VKT2438P5 with a VPW2838A2 high voltage power supply, with typical operating parameters listed in

Freq. (GHz)	**RF Power (Watts)**	**Cathode Voltage (kV)**	**Cathode Current (mA)**	**Body Current (mA)**	**Anode Voltage (kV)**	**Collector Voltage (kV)**
139.5	17.4	-9.60	85	2.1	+4.22	+9.56
140.0	17.1	-9.68	85	2.1	+4.22	+9.64
140.5	17.1	-9.75	85	2.1	+4.22	+9.71

Table 2.6: **EIO Tube Operating Parameters** The above numbers reflect typical tube operating conditions with a heater voltage and current of 6.35V and 0.865A. The emission voltage and currents were 500V and 3.94mA, with cooling water flow rate of 1.5 l/min.

table (2.6).

The EIO tube operates much like an electron accelerator, but in reverse [61]. The microwaves were produced by passing an electron beam through a resonant cavity structure inside the tube. The vacuum innards of the EIO tube contained a metallic ladder structure through which an electron beam traveled, exciting RF energy between the structure. The frequency of the microwaves produced is a function of the spacing between the resonant cavity walls. The tube produced nearly 17W of microwave radiation, which decreased to about 1W of total delivered energy to each target cavity after passage and attenuation through the waveguide system. The EIO apparatus also contained a motor driven assembly that allowed the operator to change the size of the resonant cavity. This allowed for adjustment of the microwave frequency. By running the motor back and forth, the proper frequency was attained to polarize protons or deuterons in the positive or negative direction. Fine adjustment was realized by changing the cathode voltage.

Once the microwaves were generated, they were delivered to the target cavities by way of an assembly of waveguides and couplers. Figure (2.16) illustrates the configuration used during E155. The system contained a switch that allowed for delivery to

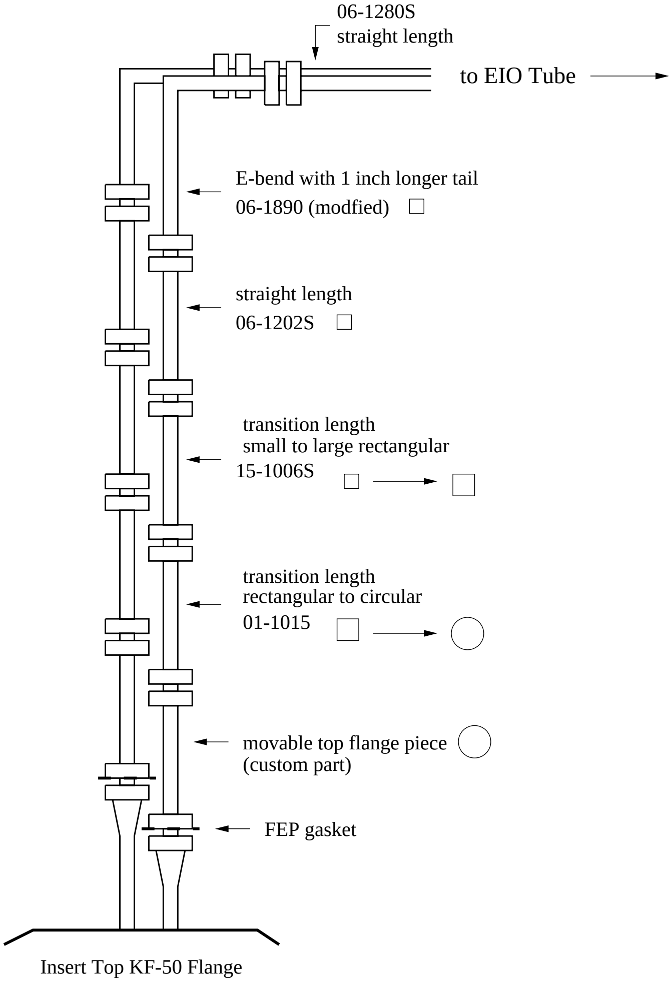

Figure 2.16: **EIO Tube Wave Guides** The above illustrates the dual wave guide assembly used during E155 [69]. Drawing not to scale.

the upper or lower target cavity. This design delivered microwave energy to each target cavity separately. Attenuated amounts of the microwave energy were coupled out for power and frequency measurements. During E155, frequency modulation of the high voltage in order to vary the microwave frequency improved polarization buildup rate and maximum polarizations for both protons and deuterons, used to great effect in the SMC experiment [68].

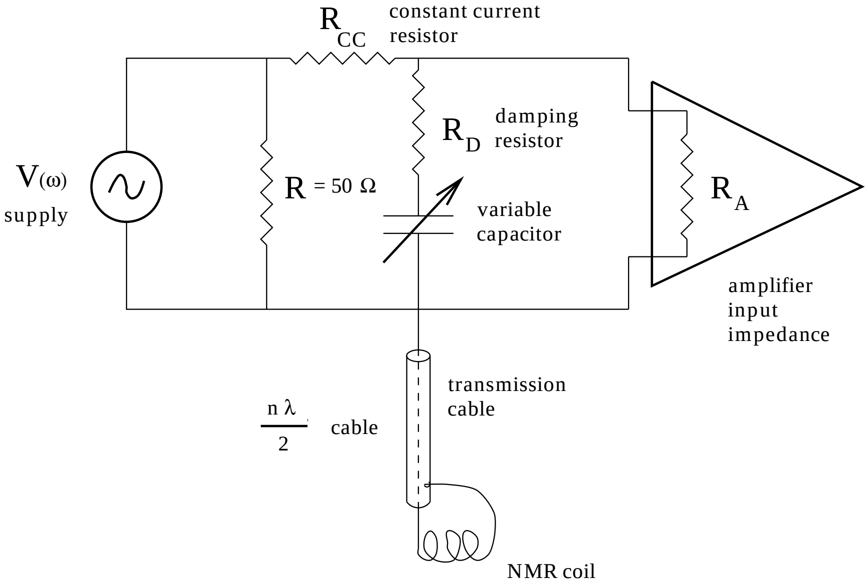

Figure 2.17: **Constant Current Series Tuned LCR Circuit** The basic circuit used by the Liverpool Q-meter modules [70]. The Q-meter circuit provides a signal with an area proportional to the target nucleon polarization.

2.3.9 NMR System

The target polarization was measured using a series-tuned LCR resonant circuit and Q-meter NMR system. Aluminum and CuNi coils embedded in the target cell provided the inductive component to the circuit. Specifically, the E155 target NMR system utilized Liverpool type Q-meters [70] by way of a constant current series tune. The circuits were tuned to the corresponding Larmor frequency of the spin species being measured. In a 5.004T magnetic field, these frequencies are 213MHz and 32.7MHz for the proton and deuteron respectively. Figure (2.17) shows the typical LCR circuit.

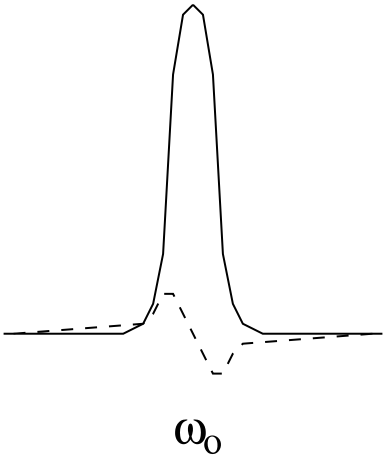

Figure 2.18: **Complex Susceptibility** The above plot shows the typical shape of the real (dispersive) and imaginary (absorptive) parts of the RF susceptibility. The solid (dashed) line represents the absorptive (dispersive) part.

NMR Measurement Theory

Polarized nucleons have a complex RF susceptibility

$$\chi(\omega) = \chi'(\omega) - i\chi''(\omega) \tag{2.15}$$

which is a function of the applied RF frequency ω. As shown in figure (2.18), the real $\chi\prime(\omega)$ and imaginary $\chi\prime\prime(\omega)$ parts have large values only near resonance and vanishingly small values at all other frequencies [71]. Given a Q-meter circuit with coil of inductance $L_\circ$, the change in inductance produced by polarized nucleons around the coil is given by

$$L = L_\circ \Big[1 + 4\pi\eta\chi(\omega) \Big] \tag{2.16}$$

where η is the *filling factor* which relates the coupling of the coil with the material. A greater filling factor results in a larger NMR signal. The nucleon polarization is proportional to the integral of the imaginary part of the susceptibility

$$P = k \int_0^\infty \chi''(\omega) d\omega. \tag{2.17}$$

Since it is difficult to calculate the susceptibility constants, it becomes necessary to calibrate the NMR signal using a measurement with a known polarization. This is achieved by taking a thermal equilibrium measurement [section (2.3.10)]. Generally, the nucleon polarization can be calculated by way of

$$P = \frac{\int_{(\omega_o - \delta)}^{(\omega_o + \delta)} \chi''(\omega) d\omega}{\int_{(\omega_o - \delta)}^{(\omega_o + \delta)} \chi''(\omega)_{TE} d\omega} \tag{2.18}$$

where 2δ is the RF frequency scan width which goes through the Larmor frequency ω_o of the spin species. More specifically, the target polarization is calibrated according to the procedure given in section (2.3.10) and equation (2.30). If the tuned circuit is fed with a constant RF current, the polarization of the target can be measured via the voltage drop across the circuit as the RF frequency is swept through the proton or deuteron resonance line. Typical proton and deuteron signal shapes observed during E155 are shown in figures (2.19) thru (2.22).

In order to extract the area of the NMR signals, "baseline" and "background" subtractions were applied to the raw measurements. The baseline measurement was made by ramping the target magnetic field down $\sim$ 1% ($\sim$3%) so that the proton (deuteron) resonance would not show up in the frequency sweep. This left a "clean" baseline Q-curve, which was then deducted from all subsequent NMR measurements. To further clean up the signal, a polynomial curve was fitted to the background

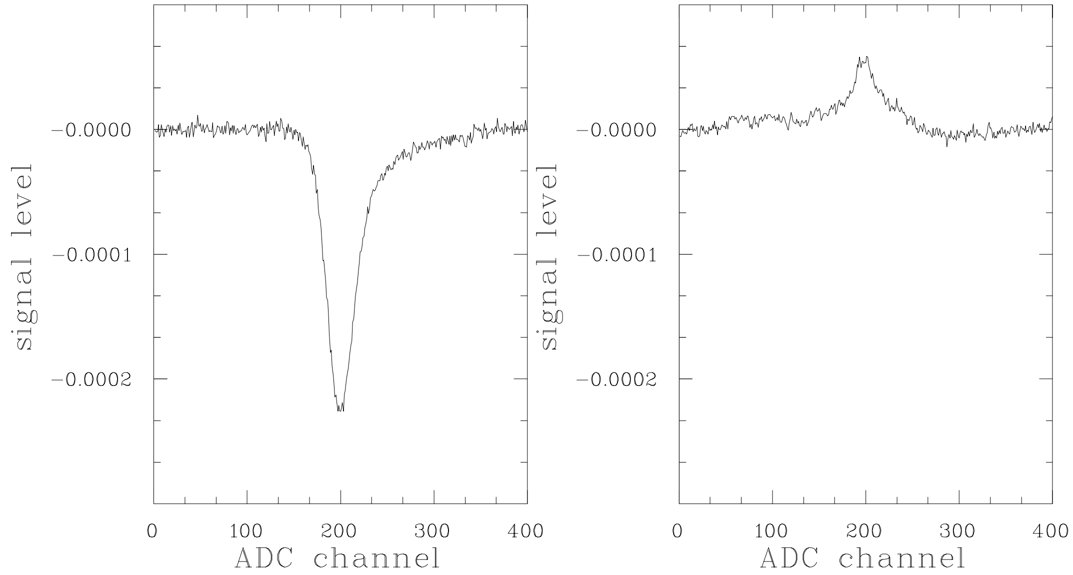

Figure 2.19: **Typical E155 Proton and Nitrogen TE Signals** The left plot shows a typical ^{1}H (proton) and the right shows a ^{15}N (nitrogen) thermal equilibrium signal with baseline and polysubtraction [72]. Note that the proton thermal equilibrium signal is inverted due to the undesirable pseudo-parallel tune of the E155 target NMR system.

on either side of the "baseline-subtracted" scan, and then removed to give the final "polynomial-subtracted" signal which was used in the area determination to give the polarization [see figure (2.21)].

^{6}LiD provides a cleaner, more obvious deuteron signal than ^{15}ND$_3$. There is no electric field gradient in ^{6}LiD that would cause line splitting in the NMR scan [see figure (2.22)]. The absence of any nuclear electric quadrupole interactions is a consequence of the face-centered cubic crystal lattice symmetry of lithium deuteride.

However, ^{15}ND$_3$ has a broad double-peaked signal due to the interaction of the deuteron quadrupole moment with the electric field gradient of the ^{15}ND$_3$ lattice, as can be seen in figures (2.23) and (2.24). Note the difference in the double-peak heights when comparing the ^{2}H TE signal with the enhanced ^{2}H signal. When the polarization is close to zero, as in the case for thermal equilibrium, the peak heights are

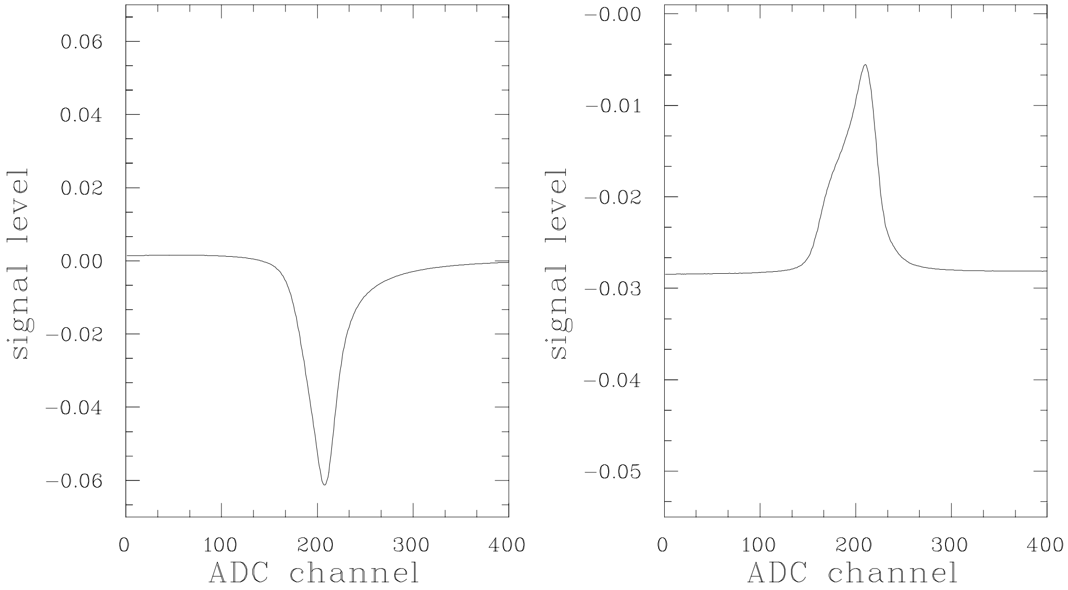

Figure 2.20: **Typical E155 Proton and Nitrogen Enhanced Signals** The left plot shows a typical ^{1}H (proton) NMR signal with baseline subtraction only and a high polarization, while the right plot illustrates an enhanced ^{15}N (nitrogen) signal with baseline subtraction only and a polarization of about -11.6%. The bumped shape of the ^{15}N peak is typical for ^{15}NH$_3$ nitrogen signals which results from two very closely situated NMR peaks from ^{15}N due to two slightly different electric fields from ^{15}NH$_3$ alignment. One peak results from ^{15}NH$_3$ molecules with three hydrogen spins aligned and the other from ^{15}NH$_3$ molecules with one hydrogen spin anti-aligned with respect to the other two.

very nearly the same. When the polarization is enhanced, the peak height difference increases. This difference can be used as an additional method to determine deuteron polarizations above about 20%, although it may not be as accurate as the preferred TE calibration method.

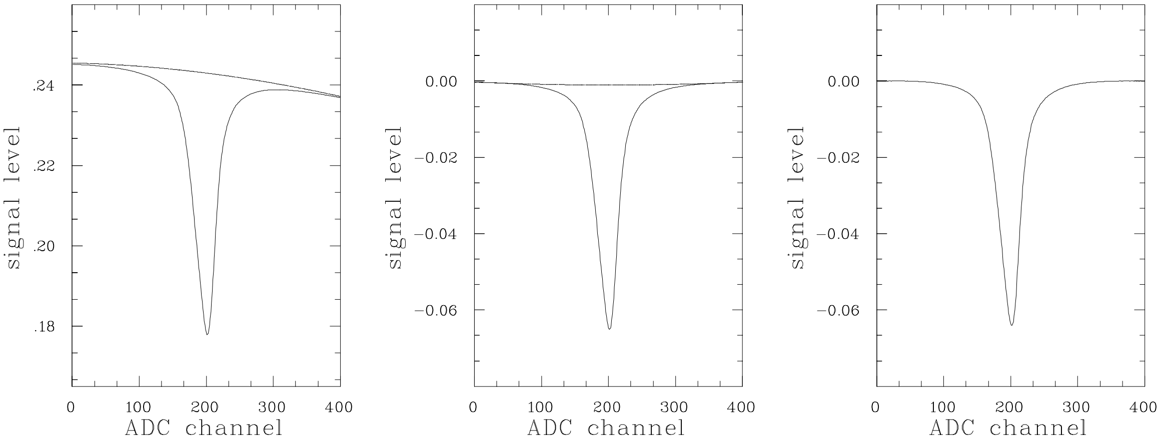

Figure 2.21: **Target Online NMR Signal Processing** The three plots illustrate the typical method used to process the NMR signals measured with the target system. This is an example of a maximum proton polarization just under 100% after a buildup. From left to right, plot a: raw proton signal with baseline, plot b: raw signal minus baseline with a quadratic fit to channels 5-50 and 350-395, plot c: final signal with the quadratic fit curve subtracted out of the baseline subtracted signal [73].

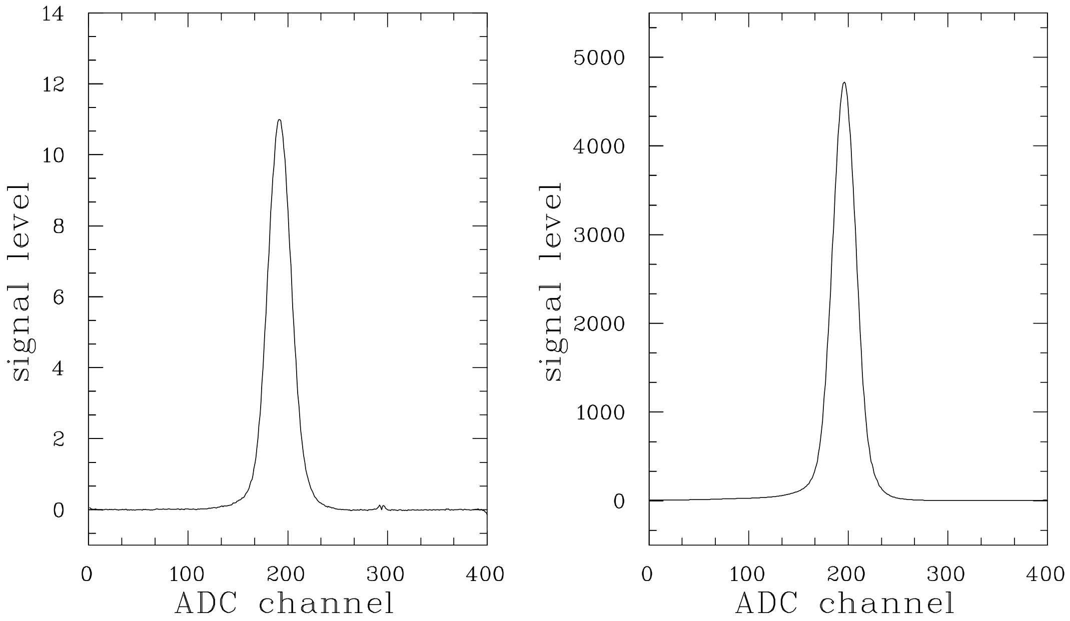

Figure 2.22: **Typical Deuteron TE and Enhanced Signals in ^{6}LiD** The left plot shows a typical deuteron TE and the right shows an enhanced deuteron NMR signal. Note its clean undistorted shape unlike for $^{15}ND_3$. Also note the scale difference between the TE and enhanced signals.

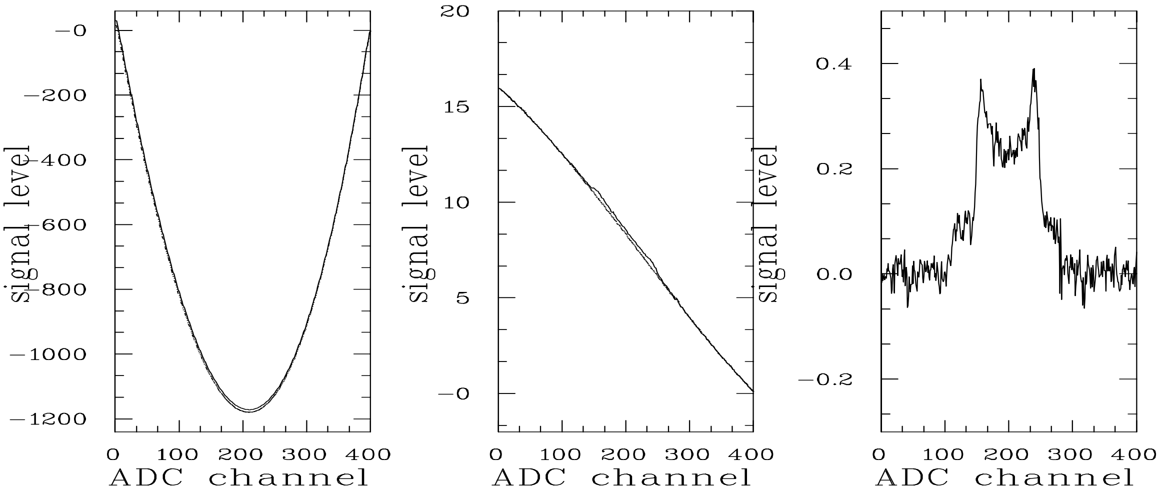

Figure 2.23: **Typical Deuteron TE Signal in ^{15}ND$_3$** The left plot shows a typical raw ^{2}H TE (deuteron) NMR signal plotted together with the baseline Q-curve, the middle shows a baseline subtracted signal with a polynomial fitted to the background, and the right shows the final polysubtracted signal. Note how small the signal is before any background subtractions are applied.

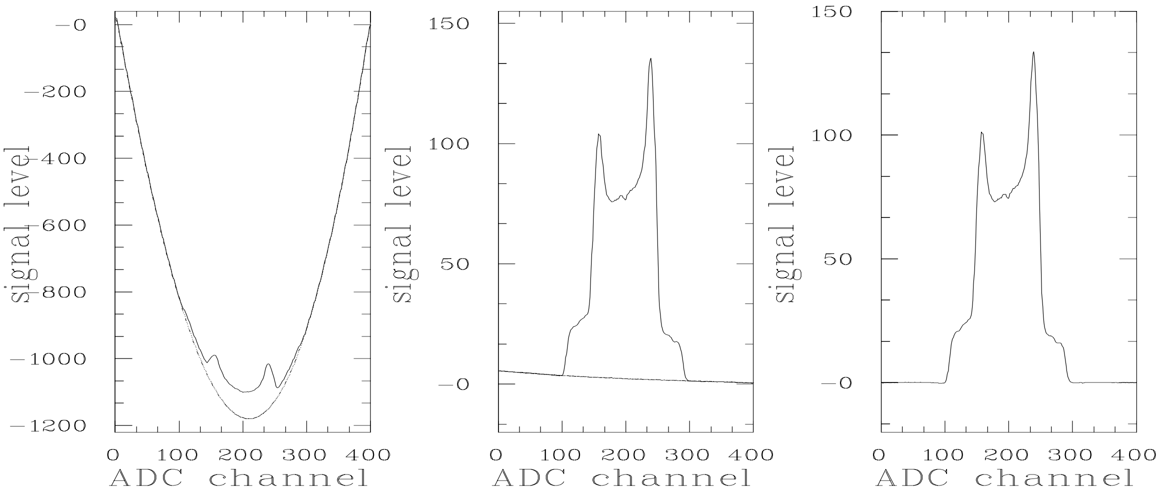

Figure 2.24: **Typical Positive Enhanced Deuteron Signal in ^{15}ND$_3$** The left plot shows a typical raw ^{2}H (deuteron) NMR signal plotted together with the baseline Q-curve, the middle shows a baseline subtracted signal with a polynomial fitted to the background, and the right shows the final polysubtracted signal.

2.3.10 NMR Calibration

The NMR signals were calibrated by making thermal equilibrium (TE) measurements at 1.4-1.6K and 5.004T. This required running the target without beam, at a stable temperature and magnetic field. The integrated area under the NMR signal was proportional to the polarization which can be calculated using the Boltzmann statistics. For a system made up of a large number N of spins in equilibrium, each spin of energy E is populated according to the Boltzmann distribution [74]:

$$N(E) = N \cdot \exp\bigl(-E/k_B T\bigr) \tag{2.19}$$

where $k_B = 1.38 \times 10^{-23}$ J/K = 86.2 MeV/K is the Boltzmann constant and T is the absolute temperature in degrees Kelvin. Hence, a system of N spins I in the presence of a magnetic field B will have each m level populated via:

$$N_m = \frac{N}{2I+1} \cdot \exp\left(\frac{m\mu B}{I k_B T}\right) \tag{2.20}$$

where μ is the magnetic moment of the nucleus of interest and B is the magnetic field in Tesla. Table (2.7) gives the magnetic moments for the electron and various nuclei. From equation (2.20), one can calculate the populations of spins in the target field and temperature in order to extract the TE polarization. See the sections below. Some sample TE NMR signals are shown in figures (2.19) thru (2.24). At E155 TE conditions, the spin orientation of the nucleons were nearly random. However, there was a small difference between the number of nucleons in each spin state, resulting in a small (less than 1%) polarization.

species	**spin**	$\frac{\mu}{\mu_{nuc}}$	**Larmor freq. at 5T**
proton	1/2	2.793	213.0MHz
neutron	1/2	−1.193	91.0MHz
deuteron	1	0.857	32.7MHz
lithium-6	1	0.822	31.3MHz
lithium-7	3/2	3.256	82.8MHz
nitrogen-15	1/2	−0.283	21.6MHz

Table 2.7: **Magnetic Moments of Selected Nuclear Species** The above table lists the moments in the third column as number of nuclear magnetons $\mu_{nuc} = 3.152 \times 10^{-14} \frac{MeV}{T}$. The electron magnetic moment is $\mu_e = 9.27 \times 10^{-24}$ J/T $= -57.94$ MeV/T. The last column lists the Larmor frequencies for each species at 5.004T.

Spin-1/2 TE Polarization Calculation

In order to calculate the nuclear polarization at the given temperature and magnetic field, we define the polarization as the difference between the numbers of nuclei in spin-up and spin-down states over the total number of nuclei:

$$P_{\text{spin}\frac{1}{2}} = \frac{N_{+\frac{1}{2}} - N_{-\frac{1}{2}}}{N_{+\frac{1}{2}} + N_{-\frac{1}{2}}}. \tag{2.21}$$

The number of nuclei in each spin state can be represented by the populations given by equation (2.20). For $I = 1/2$ species, such as the hydrogen nucleus (proton), the

Species	**TE Polarization**	**Pol. (5T/1.0K)**	**Pol. (5T/1.5K)**
electron	$P_e = \tanh\left(\frac{\mu_e B}{k_B T}\right)$	-0.998	-0.978
proton	$P_1 = \tanh\left(\frac{\mu_p B}{k_B T}\right)$	0.0051	0.0034
deuteron	$P_2 = \frac{4\tanh\left(\frac{\mu_d B}{2k_B T}\right)}{3+\tanh^2\left(\frac{\mu_d B}{2k_B T}\right)}$	0.0010	0.0007
lithium-6	$P_6 = \frac{4\tanh\left(\frac{\mu_6 B}{2k_B T}\right)}{3+\tanh^2\left(\frac{\mu_6 B}{2k_B T}\right)}$	0.0010	0.0007
lithium-7	$P_7 = \frac{5\tanh\left(\frac{\mu_7 B}{3k_B T}\right)+\tanh^3\left(\frac{\mu_7 B}{3k_B T}\right)}{3\left(1+\tanh^2\left(\frac{\mu_7 B}{3k_B T}\right)\right)}$	0.0033	0.0022
nitrogen-15	$P_{15} = \tanh\left(\frac{\mu_{15} B}{k_B T}\right)$	-0.0005	-0.0003

Table 2.8: **TE Properties of the Target** The above table lists the general expressions and actual numbers for the thermal equilibrium polarizations at 5T and 1K (1.5T). Note that μ_e, μ_p, μ_d, μ_6, μ_7 and μ_{15} are the magnetic moments for electron, proton, deuteron, lithium-6, lithium-7 and nitrogen-15, respectively.

populations are given by

$$N_{+\frac{1}{2}} = \frac{N}{2}\exp\left(+\frac{\mu B}{k_B T}\right) \tag{2.22}$$

$$N_{-\frac{1}{2}} = \frac{N}{2}\exp\left(-\frac{\mu B}{k_B T}\right) \tag{2.23}$$

Plugging the above expressions into equation (2.21), one obtains the result:

$$P_{\mathrm{spin}\frac{1}{2}} = \frac{\exp\left(+\frac{\mu B}{k_B T}\right) - \exp\left(-\frac{\mu B}{k_B T}\right)}{\exp\left(+\frac{\mu B}{k_B T}\right) + \exp\left(-\frac{\mu B}{k_B T}\right)} = \tanh\left(\frac{\mu B}{k_B T}\right). \tag{2.24}$$

The above equation is valid for calculating the proton and ^{15}N TE polarizations. The proton TE polarization for 5T and 1.5K is about 0.03%. Table (2.8) presents typical TE polarizations for all the E155 polarized target spin species.

Spin-1 TE Polarization Calculation

A similar approach is followed for $I = 1$ nuclear spin species, such as for the deuterium nucleus (deuteron). In this case, there are three possible spin states with vector polarization:

$$P_{\text{spin1}} = \frac{N_{+1} - N_{-1}}{N_{+1} + N_0 + N_{-1}}. \tag{2.25}$$

where the number of nuclei in each spin state can be given by:

$$N_{+1} = \frac{N}{3} \cdot \exp\Big(+ \frac{\mu B}{k_B T}\Big) \tag{2.26}$$

$$N_0 = \frac{N}{3} \tag{2.27}$$

$$N_{-1} = \frac{N}{3} \cdot \exp\Big(- \frac{\mu B}{k_B T}\Big) \tag{2.28}$$

From equation (2.25) one obtains the result:

$$P_{\text{spin1}} = \frac{\exp\big(+ \frac{\mu B}{k_B T}\big) - \exp\big(- \frac{\mu B}{k_B T}\big)}{\exp\big(+ \frac{\mu B}{k_B T}\big) + \exp\big(- \frac{\mu B}{k_B T}\big) + 1} = \frac{4 \tanh\big(\frac{\mu B}{2 k_B T}\big)}{3 + \tanh^2\big(\frac{\mu B}{2 k_B T}\big)}. \tag{2.29}$$

The above equation is valid for calculating the deuterium and ^{6}Li polarizations. A thermal equilibrium deuterium polarization is about 0.07%.

Once the TE measurements were done, the target material was dynamically polarized and the area under the enhanced signal was measured. The TE area, TE polarization and enhanced signal area were then used to determine the enhanced polarization:

$$P_{\mathrm{enh}} = \frac{P_{\mathrm{TE}}}{A_{\mathrm{TE}}} A_{\mathrm{enh}}. \tag{2.30}$$

The above expression also contained a “calibration constant” that corrected for the difference in the signal areas since the larger enhanced signals were measured with much less amplifier gain than the small TE signals.

Proton NMR Signal Anomaly

During E155, there was evidence indicating that there was a problem with the NMR measurements to determine the proton polarization. Problems observed included difficulty in tuning the NMR circuit (adjustment of the capacitance and length of phase cable in order to center the circuit resonance on the proton Larmor frequency), inverted Q-curve and signal, distortion in the wings of the NMR signal, polarizations above 100% and significant difference in spin asymmetry obtained from high versus low proton polarization runs. For a detailed explanation of these symptoms and subsequent correction, refer to McKee [75, 76].

In normal operation, one would expect to see a Gaussian-like shaped proton signal; however, distorted and inverted ones were observed as illustrated in figure (2.25). The target cells were made of copper-plated aluminum instead of the non-metallic torlon material as used in E143. The proton signals were inverted regardless of the material composition of the sampling coils; although, the aluminum coils did produce more distorted and attenuated proton signals than did the CuNi coils (amplitudes from aluminum coils were six times smaller than from CuNi). Fortunately, no problems were observed with the ^{15}N (21.59 MHz), ^{6}Li (31.3 MHz), deuteron (32.7 MHz) and

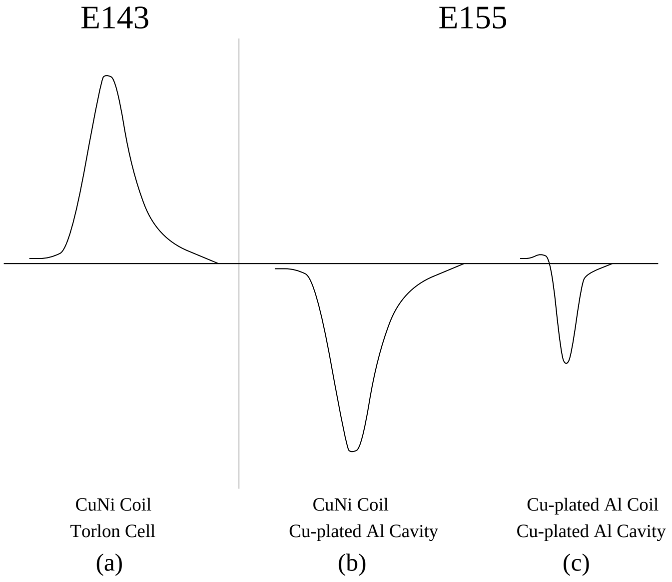

Figure 2.25: **Typical Proton NMR Signals** (a) The typical normal proton signal expected and seen during E143. (b) The actual anomalous proton signal observed during E155 for ammonia targets with CuNi coil and Cu-plated Al cavity. (c) The actual anomalous proton signal observed during E155 with Cu-plated Al coils and Cu-plated Al cavity.

^{7}Li (82.8 MHz) signals, which were typically much smaller in amplitude and tuned to a much lower Larmor frequencies than the proton (213 MHz) in a 5 T magnetic field. Moreover, technical runs performed after the experiment further indicated that the signal anomaly was a frequency-dependent effect. Using a microwave tube that oscillated at half the frequency (70 GHz) of the tube used during the experiment (140 GHz), the target magnetic field was also halved (2.5T). This required the NMR circuit to be tuned to a proton Larmor frequency of 106.5 MHz. The resulting measurements showed that all the problems previously seen with the proton signal were no longer present.

Court and Holden of Liverpool [77] modeled the NMR circuit used during E155 and argued that it must have contained too much stray capacitance across the sampling coil due mainly to the metal target cavities [see figure (2.26)]. According to the

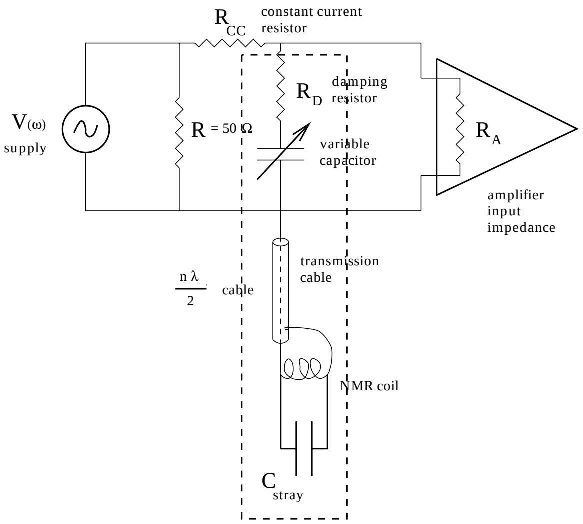

Figure 2.26: **LCR Circuit with Stray Capacitance**

model, the effect of stray capacitance becomes more significant with increasing frequencies and larger signal size. It was found that the Q-curve flips when an E155-type circuit is tuned to 213MHz with stray capacitance > 18 pF (when total impedance of the coil and parallel C_{stray} is greater than 50 Ω) [see section (B.1)]. At such high stray capacitances, the constant-current conditions ($Z_{res} \gg R_A$) are no longer satisfied and the circuit actually operates in a so-called "pseudo-parallel" tune-mode. The main factors that contributed to the undesirable capacitance include the metal cavities, the copper-plating, an incorrect length of $n\lambda/2$ cable and ammonia's large dielectric constant ($\epsilon > 18$). Technical runs performed after the experiment showed that the transmission cable length was the main factor that caused the problems seen with the NMR system tuned to 213MHz [78].

Although the non-linear behaviour of the NMR circuit was qualitatively understood, there was insufficient information on critical RF parameters to correct for the non-linear circuit performance [79] on the RF level. Instead, the correction to the E155 proton polarization problem used data on the polarization decay due to in-beam

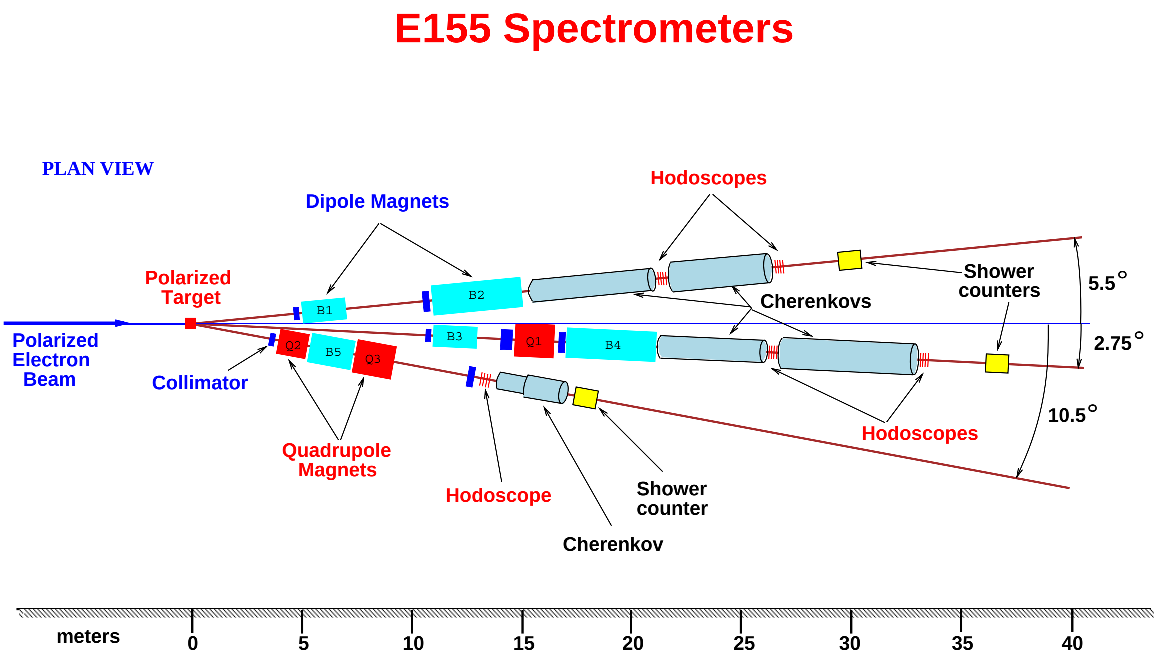

Figure 2.27: **Plan View of the Spectrometers**

radiation damage [75, 76]. The accumulated dose was used as a link between the incorrect measurements of E155 and the correct measurements of E155X. A functional form was not fitted to data, but a binning and averaging method was used to create the correction curves, since an average is free to follow the data. No constraints were put on the correction which amended the proton polarizations as one would expect but with larger error than a pure NMR measurement.

2.4 Spectrometers

The scattered electrons from the DIS process were detected in three independent fixed angle magnetic spectrometers as shown in figures (2.27) and (2.28). The 2.75 and 5.5 degree spectrometers were the same as used in E154, whereas the 10.5 degree was new for E155. The 10.5 degree extended the kinematic range of the experiment,

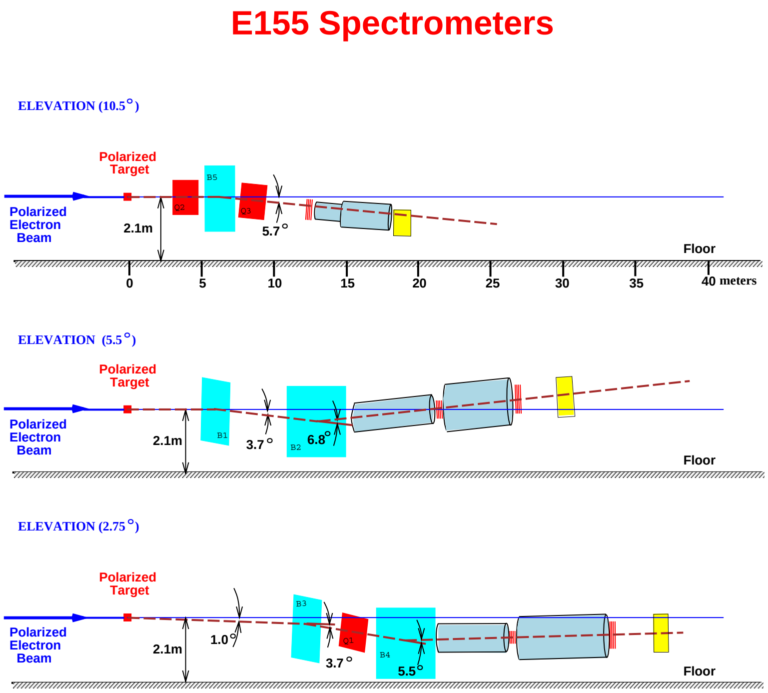

Figure 2.28: **Side View of the Spectrometers**

roughly doubling the range in Q^2. The kinematic coverage of the spectrometers is shown in figure (2.29). The spectrometers were designed to identify the type and determine the energy, momentum and path of charged particles scattered from the target region. Dipole and quadrupole magnets bent and focused the charged particles in order to reduce background from high energy photons (from which various particles such as π, K, e^+ and e^- are produced) and spread particles out according to momentum. Cherenkov counters provided particle identification to distinguish electrons from other charged particles. Hodoscopes provided track information from which particle momentum and scattering angle could be determined. Shower counters were also used for particle identification by measuring particle energy.

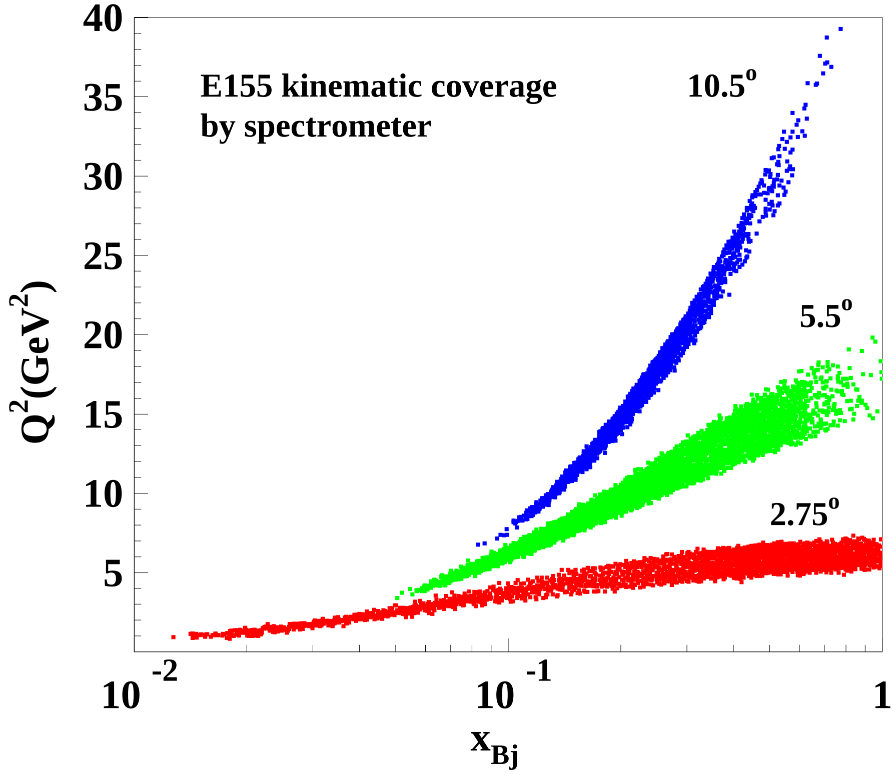

Figure 2.29: **Kinematic Coverage of the E155 Spectrometers**

2.4.1 Magnets

The E155 spectrometers utilized different combinations of dipole and quadrupole magnets to steer and focus scattered charged particles on a path that removed any straight line of sight between target and the detectors. The purpose was to cut out photon background at small angles due to bremsstrahlung, Møller scattering and π-meson decay [80]. Specifically, the 2.75 and 5.5 degree systems each contained two dipoles that bent particles vertically in opposite directions to create a "double-bounce" system that greatly suppressed the photon background. Only after scattering from the walls twice could photons make it through the entire spectrometer. The 2.75 degree system also used a quadrupole magnet between the dipoles to refocus the momentum spread of particles in the vertical plane and defocus in the horizontal

Spectrometer	**Mode**	**Horizontal** θ **(mr)**	**Vertical** ϕ **(mr)**
2.75°	large	48.0 ± 5.0	$-28.5 \leq -13.25 \leq +2.0$
	medium	48.0 ± 5.0	$-28.5 \leq -15.25 \leq -2.0$
	small	48.0 ± 5.0	$-28.5 \leq -16.25 \leq -4.0$
5.5°	normal	96.0 ± 8.85	$-23.4 \leq -9.2 \leq +5.0$
10.5°	normal	183 ± 34	$-20 \leq 0.0 \leq +20$

Table 2.9: **Nominal Acceptances for the 2.75, 5.5 and 10.5 degree Spectrometers**

plane for better overall coverage over the shower counter detectors. The 5.5 degree did not use a quadrupole and only contained the two dipoles.

The 10.5 degree used a “single-bounce” system since it was constructed on limited funds and available equipment. It contained one dipole sandwiched between two quadrupoles. The first quadrupole focused particles in the horizontal plane, the dipole bent them downward and the last quadrupole focused in the vertical plane to optimize particle spread over the detectors downstream.

Table (2.9) shows the nominal acceptances for the 2.75, 5.5 and 10.5 degree spectrometers.

2.4.2 Cherenkov Counters

Particle identification was made using two threshold gas Cherenkov counters in each of the small angle spectrometers while only a single counter was used in the 10.5 degree. When a charged particle traverses a medium with speed greater than the

Spec Angle	**Pressure (psia)**	π **threshold momentum**	K **threshold momentum**	p **threshold momentum**	e^- **detection efficiency**
2.75°	1.3	20 GeV/c	~50 GeV/c	>100 GeV/c	95%
5.5°	1.9	16 GeV/c	~50 GeV/c	>100 GeV/c	95%
10.5°	2.8	13 GeV/c	~50 GeV/c	>100 GeV/c	70%

Table 2.10: **Thresholds for the Cherenkov Counters**
The thresholds are for pions, kaons and protons, below which, all electrons were above threshold.

speed of light in the medium, Cherenkov radiation is emitted which can be detected using a photo-multiplier (PMT or “phototube”) detector [81]. This speed is given by

$$v = \frac{c}{n}, \tag{2.31}$$

where c is the speed of light in vacuum and n is the index of refraction. E155 used a gas mixture of 90% N_2 and 10% CH_4. Nitrogen is a typical gas used for Cherenkov counters for electrons at energies of this experiment. Methane was used to suppress scintillation light created by N_2 in the counter. Adjustment of the pressure determined the index of refraction of the gas medium and hence the threshold velocity for a particle before Cherenkov light would be produced. Since particles have different masses, the threshold momentum will be different depending on mass. Therefore one can set a momentum range in which only electrons will cause Cherenkov light production but other particles will not (ie. the momentum window for only electrons emitting light with a background of pions was 50 MeV/c to 13-19 GeV/c). Table (2.10) shows the gas parameters used to allow mostly electrons to emit light in the tank with a background of pions, kaons and protons [82, 83]. The Cherenkov light was detected by redirecting the light by way of mirrors to Hamamatsu R1584 phototubes situated outside the acceptance of the spectrometers [84].

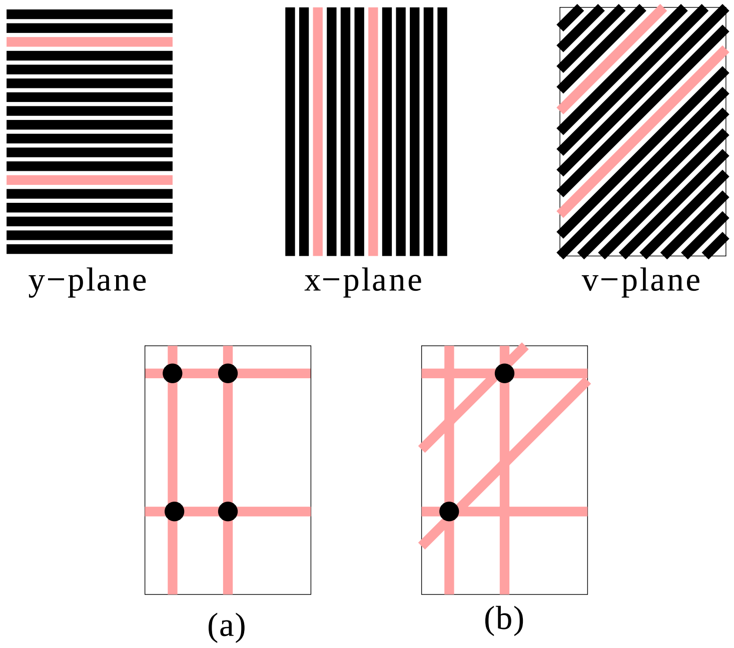

Figure 2.30: **Multiple Hit Ambiguity** An example of two particles traversing simultaneously the hodoscope with two hits registered in each x, y and v-plane. (a) If only x and y-plane information is used, four positions are possible. (b) The addition of v-plane information helps resolve the two particle positions.

2.4.3 Hodoscopes

The hodoscopes were thin detector arrays oriented in the plane perpendicular to the predicted path of the charged particles that traveled through the spectrometers. They consisted of thin and narrow fingers of scintillators with photo-multipliers attached at one end, all in a light tight package. Charged particles that traveled through these fingers excited the atoms and molecules in the material which caused a small flash of light to be emitted from de-excitation. The “scintillation” light was then detected by the phototube. The spectrometers had several planes of hodoscopes with the fingers aligned in various orientations. Consider a right-handed rectangular coordinate system to describe the experiment where the direction of the beamline is considered to be the $+z$ direction. Each hodoscope plane measured the z-coordinate and one transverse dimension. Sets of vertical fingers (x-plane) determined the x-coordinate while sets of horizontal fingers (y-plane) determined the y-coordinate of the traversing particle. Together, the x and y-planes provided horizontal and vertical coordinates for the particle path. Also, there were so-called u and v-planes with fingers angled at $\pm 15°$ ($\pm 45°$) for the 2.75 degree (5.5 degree) spectrometers which helped remove ambiguity in the particle position due to multiple hits. Figure (2.30) offers an example where two hits in each x and y-plane can be interpreted as four possible track positions. The addition of v-plane information removes the uncertainty. The 2.75 degree had two sets with a total of ten planes, (u, v, x, y, y, x) in front and (x, y, y, x) in back of the second cherenkov counter 2C2. The 5.5 degree had two sets with a total of eight planes, (u, x, y, v) in front and (u, x, y, v) in back of the second Cherenkov counter 5C2. The 10.5 degree had one set with four planes (y, y, y, y) in front of the single Cherenkov 10C1. These hodoscopes provided particle position information from which particle tracks were reconstructed which allowed extraction of particle momentum information.

2.4.4 Shower Counters

The total absorption (TA) shower counters were used to determine the total energy of the scattered particle that made it through the entire length of the spectrometer. The TA shower detectors were organized in grids where each lead-glass block had a front face of dimensions 6.2cm x 6.2cm and length of 75cm length. The block material had an index of refraction $n \approx 1.6$ and radiation length $x_o = 3.17$ cm for a total of ~ 24 radiation lengths long. An Amperex XP2212PC phototube was coupled to the downstream end with everything contained in a light tight package [82].

When a charged particle deposits energy into the lead-glass block, light is generated and detected by the phototube. A high energy electron will create an electromagnetic shower of photons and positron-electron pairs via bremsstrahlung and pair-production, respectively. The photons decay to positron-electron pairs, which, in turn, radiate more photons. This shower continues until the electron's energy drops below a critical value ($\sim$ 10 MeV), the point at which ionization and excitation losses are equal to bremsstrahlung radiation losses. The positrons and electrons in the shower (traveling faster than the speed of light in the glass) emit Cherenkov radiation (light) which is detected by the phototube. The combination of all these processes produce an amount of light whose intensity is proportional to the energy of the electron since it gets totally absorbed by the lead-glass. Most hadrons (mainly π for this experiment) will deposit a small fraction of their energy in the blocks since they create mostly hadronic rather than electromagnetic showers. The more massive hadronic particles are less likely to radiate via bremsstrahlung. Instead, they produce secondary hadrons via nuclear collisions. The length of material needed for hadrons to deposit all their energy in the lead-glass is much greater than the shower counter design. Moreover, most of the energy the hadrons lost in the block was in the form of nuclear interactions that did not produce light. Therefore, the ratio of shower energy to tracking momentum ($E^{'}/p$) helped distinguish electrons from pions. $E^{'}/p \sim 1$ ($E^{'}/p < 0.2$) would most likely be an electron (pion). More information on particle identification can be found in section (3.2) on event analysis.

The 2.75 and 5.5 degree shower counters consisted of a 10 x 20 block grid oriented with the front face plane perpendicular to the particle path or z-axis of each spectrometer. The 10.5 degree shower counters consisted of a 6 x 5 grid of TA detectors with a layer of 10 thin pre-radiators (PR) covering its front plane. The purpose of the PRs was to supplement position information due to the lack of hodoscope planes in the 10.5 degree system. Since the PRs were thin, they had a very small effect on the energy measurement made by the TAs. For the experiment, the total energy was calculated as the sum of TA + PR.

2.5 Detector Electronics

The experiment used a trigger-less data acquisition system (DAQ) which was designed to process every detector event that occurred within the time of a beam spill. The signals from the hodoscope, Cherenkov and shower counter phototubes were processed by discriminator (DISC), time-to-digital converter (TDC) and analog-to-digital converter (ADC), NIM and CAMAC modules and flash-ADC (FADC) VME module electronics. The beam source provided the electronics with a signal that let it know when to start and stop collecting the event data according to the beginning and end of each beam pulse. In the time between each pulse, the event data was transferred to disk buffers and eventually written to tape.

Figure (2.31) is an overview of the electronics. The processing of the hodoscope signals required knowledge of the time a specific finger fired. This was accomplished by first sending the phototube signal through a DISC to set a minimum level for dark current and background events. Then the signal was processed by a TDC to record the time it occurred relative to the start of the spill. In addition to sending them through a set of DISCs and TDCs, the shower counter signals were also passed through a set of ADCs in order to determine the integrated signal amplitude. The Cherenkov detector information was processed by two systems: a primary FADC and a secondary TDC system. Each Cherenkov phototube anode signal was sent to a FADC which provided a digitized version of the phototube output with 1ns resolution. This provided pulse

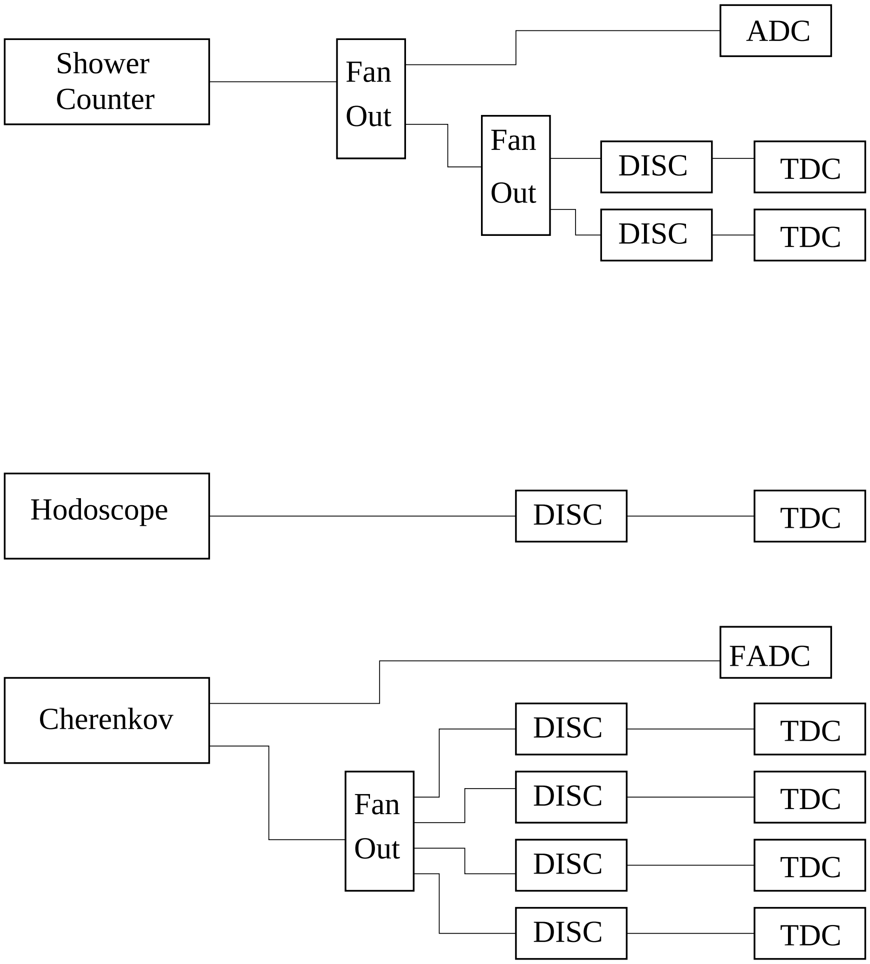

Figure 2.31: **Electronics Overview**

shape information to help identify electrons from pions. Each dynode output was split to four TDCs via discriminators set at different thresholds. The DISC/TDC system provided limited pulse height information by way of the combination of which TDC levels fired. The TDC system provided a backup to the primary FADC system. During E155, the FADCs timing often shifted relative to the data acquisition start which was corrected using the backup TDC timing information.

2.6 Data Acquisition

The raw signal data from the detectors of all three spectrometers and information from the beam monitoring devices were read into a VME-based computer system (hardware DAQ) [82, 85], which served as an interface between the detector electronics and the software DAQ that stored the data on 1GB tapes. All data from each and every beam spill was recorded as more than 4000 runs on roughly 2000 1GB tapes. There were different types of runs: *normal raw data runs* to record the DIS data for scattering off the polarized targets (^{15}NH$_3$ and ^{6}LiD), *solid target runs* to record the DIS data for scattering off the unpolarized solid targets (^{9}Be and ^{12}C), *Møller runs* to record the polarized e-e scattering data used to determine the beam polarization, *Flashlamp (LED) calibration runs* to measure detector ADC response to known signals generated by xenon light (light emitting diodes), *Pedestal calibration runs* to determine the background in all the detectors while the beam was suppressed and *Toroid calibration runs* to adjust the beam charge measurement by sending a known current through the toroid coil devices. Each normal raw data run lasted until a 1GB tape became full, typically 25 minutes in duration with $\sim 175,000$ spills worth of information; whereas, the solid target and calibration runs lasted anywhere from a few seconds to several minutes, depending on the type of run.

Chapter 3

Data Analysis

This chapter discusses the steps that were required to extract the measured asymmetry from the raw data. The process involved converting the raw detector data into particle identification, trajectory, energy and momentum information from which a raw asymmetry was determined. Then various experimental equipment-based and physics-based corrections were applied to the raw asymmetry to arrive at a Born asymmetry from which the spin structure functions were extracted.

3.1 Raw to Summary Tapes

The raw data tapes were processed to make data summary tapes (DSTs) which contained shower cluster, Cherenkov hit and particle track information (described in more detail below) in addition to relevant beam charge, position and quality information. The raw detector information from each run was processed spill by spill in the following manner. The raw shower counter TDC and ADC hits were *clustered*, a process that determined the energy E' of a particle event by grouping and adding the energy of adjacent blocks hit at nearly the same time. The pulse height and area information of each Cherenkov counter hit were determined from the raw FADC spectra. In a procedure called *tracking*, the raw hodoscope TDC hits were associated with shower clusters and Cherenkov hits that occurred at nearly the same time and were consistent with a straight line trajectory through the spectrometer. Such particle path information allowed the experiment to determine whether or not the particle originated from the target cell. Details on the tracking procedure can be found in [82].

The resultant DSTs were about a third of the size of the original raw data for each run. More important, the time to process the data from a run on a DST took only 20 minutes as opposed to over 20 hours from the raw data tapes. This is because the reconstruction of the particle events (clustering and tracking) from the large number of raw detector events was the most compute intensive part of the analysis. The DSTs allowed for reanalysis of the electron candidates to determine an asymmetry without unnecessarily repeating the particle reconstruction each and every time.

3.2 Event Analysis

From the DSTs, the data were examined to determine the particle type. This *particle identification* process required each particle event to pass a set of beam, kinematic and spectrometer criteria (cuts) in order to be considered an electron (positron or pion). Typically, a coincidence between a hodoscope-based track, shower cluster and Cherenkov hit qualified as an electron event. The tracks required a minimum number of hits from each hodoscope package, the track momentum p and shower energy $E^{'}$ had to be close in value and the Cherenkov signals be within a defined range. Once identified, the electron events would enter into the determination of the raw asymmetry; whereas, positron and pion events were used to determine various corrections to the asymmetry.

3/4 hits in each hodoscope package*

$0.8 < E^{'}/p < 1.2$

$\sqrt{V_{peak}(\mathrm{C1}) * V_{peak}(\mathrm{C2})}$

$Q^2 > 1\mathrm{GeV}^2$ and $W^2 > 4\mathrm{GeV}^2$

Table 3.1: **Electron Definitions for 2.75 and 5.5 Degree** Kinematic and spectrometer cuts for the small angle spectrometers. *The upstream 2.75 degree package requires 4 hits out of 6 planes for an electron ID.

For the 2.75 and 5.5 degree spectrometers, electron tracks were identified by way of the cuts presented in table (3.1). The shower energy $E^{'}$ had to be close in value to the track momentum p since electrons are expected to deposit all their energy in the shower blocks, but pions are not. Both Cherenkovs were required to have a signal with the product of their peak voltages falling in a specified range to maximize electron detection and pion rejection. The $Q^2 > 1\mathrm{GeV}^2$ and $W^2 > 4\mathrm{GeV}^2$ cuts assured DIS events, excluding any quasi-elastic and resonance region scattering events. For the 10.5 degree spectrometer, a more complex definition was required since it contained less hodoscope tracking information and only one Cherenkov detector signal. Details on the 10.5 degree electron track criteria can be found in [82, 86, 87].

Additional cuts based on beam quality and polarization state were required and are outlined in table (3.2). Data taken with raster positions outside the target area and poor beam focusing, determined via the spill monitors and foil array, were not used since such conditions typically resulted in excessive background rates due to beam clipping the beampipe or other materials. The beam charge, as measured by the toroid devices, had to fall within a few giga-electrons for each spill. Moreover, events were discarded anytime the state of the beam polarization was in doubt. The polarization state was realized via four sets of measurements called PMON, MACH,

good spill:	$0 < \text{ADC} < 2000$
bad spill:	$0 < \text{ADC} < 2000$
foil array x:	-20.0 mm $< x <$ 15.0 mm
	0.2 mm $< dx <$ 5.0 mm
foil array y:	-20.0 mm $< y <$ 15.0 mm
	0.1 mm $< dy <$ 5.0 mm
toroids 2&3:	0.5 Ge $< Q_{beam} <$ 5.0 Ge
polarization bits:	all 4 bits agree

Table 3.2: **Beam Cuts** The spill monitor cuts are in ADC units. The beam charge values are in Ge $\equiv 10^9 e^-$/spill.

SCALAR and VETO [88]. Each measurement was reported by two bits, with the bit patterns 00, 01, 10, and 11 representing unpolarized, left helicity, right helicity and error, respectively. The polarization state was considered known only if all four measurements agreed.

3.3 Asymmetry Analysis

This section describes how the raw asymmetry was extracted from the electron event information and the various corrections that were applied to arrive at a final Born asymmetry.

3.3.1 Raw Asymmetries

The Born asymmetries $A_{\parallel}$ and $A_{\perp}$ are defined in terms of the cross-sections given in equations (1.23) and (1.24). These asymmetries were measured using the difference in electron scattering rates for left and right helicity states. Since the cross-sections were measured for both helicity states with the same spectrometer simultaneously, the measured asymmetries had only a small dependence on the acceptance and efficiency of the detectors. For longitudinally polarized electrons and longitudinally (transversely) polarized nucleons, the nucleon asymmetry $A_{||}$ $(A_{\perp})$ is defined:

$$A_{||}(A_{\perp}) = \left(\frac{R_L^{nuc} - R_R^{nuc}}{R_L^{nuc} + R_R^{nuc}}\right) \tag{3.1}$$

where the electron event rate is given by:

$$R_{L(R)}^{nuc} = \frac{N_{L(R)}^{nuc}}{Q_{L(R)}} d_{L(R)}. \tag{3.2}$$

N^{nuc} is number of polarized electrons scattered from polarized protons or deuterons for longitudinal or transverse running

$$N_L = N^{\downarrow\Uparrow} \;\text{ or }\; N^{\downarrow\Leftarrow} \tag{3.3}$$

$$N_R = N^{\uparrow\Uparrow} \;\text{ or }\; N^{\uparrow\Leftarrow} \tag{3.4}$$

Q is the incident electron beam charge for the same helicity orientations

$$Q_L = Q^{\downarrow\Uparrow} \;\text{ or }\; Q^{\downarrow\Leftarrow} \tag{3.5}$$

$$Q_R = Q^{\uparrow\Uparrow} \;\text{ or }\; Q^{\uparrow\Leftarrow} \tag{3.6}$$

and d is the dead time correction to the measured rate. In the above equations, the *left* thin arrow represents the electron helicity while the *right* thick arrow represents the nucleon helicity.

Equation (3.1) would be correct if we had a pure proton or deuteron target. However, the actual electron rates *measured* include scattering from unpolarized non-target nucleons and non-target residual polarized nucleons which dilute the asymmetry. Hence, our measured or *raw* asymmetry is actually

$$A_{raw} = \left(\frac{R_L^{tot} - R_R^{tot}}{R_L^{tot} + R_R^{tot}}\right) = \frac{\left(\frac{N_L^{tot}}{Q_L} d_L - \frac{N_R^{tot}}{Q_R} d_R\right)}{\left(\frac{N_L^{tot}}{Q_L} d_L + \frac{N_R^{tot}}{Q_R} d_R\right)} \tag{3.7}$$

where N^{tot} is number of electrons scattered from *all* materials in our target.

Various corrections must be made to A_{raw} to obtain the Born asymmetry. Internal radiative and electroweak asymmetry corrections account for non-DIS electrons. External radiative corrections consider energy loss processes before and after scattering. Target polarization, dilution factor and nuclear corrections correct for scattering off unpolarized and non-target nucleons; whereas, the beam polarization accounts for beam helicity < 1. Positron-electron pair and pion contamination corrections account for electrons which did not originate from the beam or pions misidentified as electrons, respectively. Positron asymmetry runs were taken during the experiment to determine this particle contamination correction. Track identification errors, rate and resolution effects must also be considered. With the above corrections, the measured asymmetry A_{raw} can be related to the Born asymmetry by way of the following set of relations [83, 89]:

$$A_{meas_i} = \frac{A_{raw_i} - \Delta A_{rate_i} - P_{b_i} A_{EW_i}}{f_i C_{1_i} P_{b_i} P_{t_i}} + C_{2_i} A_{nuc_i} \tag{3.8}$$

$$A_{Born} = \frac{1}{n_{e^-} f_{RC}} \left(\langle A_{meas} \rangle - \frac{n_{e^+}}{1 - n_{\pi^+}} \left[A_{e^+} - n_{\pi^+} A_{\pi^+} \right] - n_{\pi^-} A_{\pi^-} \right) + A_{RC}. \tag{3.9}$$

where $\langle A_{meas} \rangle$ is the statistically weighted average of the asymmetries over i runs:

$$\langle A_{meas} \rangle = \frac{\sum\limits_i A_{meas_i} / \delta^2 A_{meas_i}}{\sum\limits_i 1/\delta^2 A_{meas_i}} \tag{3.10}$$

A_{EW}	electroweak asymmetry
ΔA_{rate}	rate dependence
P_b	beam polarization
P_t	target polarization
f	dilution factor
$C_1, C_2,\ A_{nuc}$	nuclear corrections
A_{e^+}	positron asymmetry
$A_{\pi^\pm}$	pion asymmetries
A_{RC}, f_{RC}	radiative corrections

Table 3.3: **Corrections to A_{raw}** The top set of corrections were applied to each run, while the bottom set were applied after combining all runs. The quantities, n_{e^-}, n_{e^+}, n_{π^-} and n_{π^+} represent the fraction of events coming from DIS electron events, the fraction of events coming from positrons created in pair-symmetric processes and -(+) charged pions, respectively.

The correction terms are identified in table (3.3) and explained in detail in the sections that follow. The raw asymmetry A_{raw} was determined and the corrections ΔA_{rate}, A_{EW}, f, P_b, P_t, C_1, C_2, and A_{nuc} were applied on a run-by-run basis. After combining these partially corrected asymmetries, the final set of corrections A_{e^+}, A_{π^+}, A_{π^-}, f_{RC} and A_{RC} were applied to get the final Born asymmetry.

The raw asymmetries were measured on a run-by-run basis by counting the number of electrons detected per incident electron beam charge for each of the helicity orientations. The statistical error on the number of events is given simply by $\sigma_N = \sqrt{N}$ while the error on the incident beam charge was neglected. The error on the raw asymmetry can be expressed by

$$\sigma_{A_{raw}} = \frac{2\sqrt{N_L N_R (N_L + N_R)}}{Q_L Q_R \left(\frac{N_L}{Q_L} + \frac{N_R}{Q_R}\right)^2}. \tag{3.11}$$

3.3.2 Electroweak Correction

There is an asymmetry A_{EW} in DIS of left and right polarized electrons off unpolarized nucleons which is due to an interference between the weak (neutral current) and electromagnetic scattering amplitudes [90]. Since the electroweak effect does not depend on the target polarization, equal amounts of data collected with the target polarized in each direction would cancel it out. The A_{EW} correction turned out to be small, resulting in $\sim 1\%$ ($\sim 5\%$) increase in the proton (deuteron) asymmetry.

3.3.3 Rate Dependence

The design of the spectrometers made sure rate dependent detector efficiency effects were kept at a minimum. However, small variations did exist and a model of each spectrometer helped determine a kinematic-dependent correction to the measured asymmetry. Moreover, the track construction algorithm added an element of rate dependence, since any increase in rate would increase the tracking complexity. The correction method utilized a program called "pulse fiction" which was identical to the one used for E154. The particle tracking efficiency was determined at twice the normal experimental rate by merging raw data hits from successive spills, rerunning the tracking code and comparing the whole process to the tracking at the normal rate. The final correction increased the asymmetries by $\sim 1\%$.

3.3.4 Beam Polarization

The beam polarization was determined using two different measurement techniques: single-arm and double-arm Møller polarimetry. Measurements were taken several times during the experiment and it was found that the beam polarization was very stable throughout the entire experiment [see figure (3.1)]. The results from both

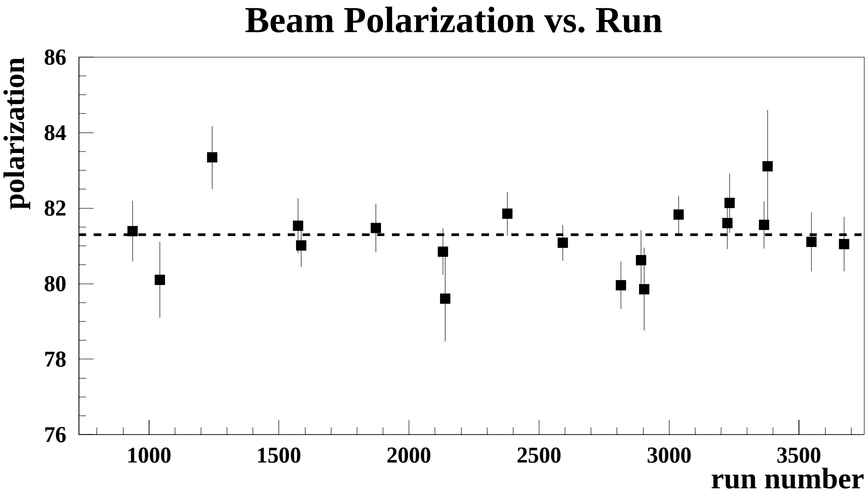

Figure 3.1: **Beam Polarization versus Run**

polarimeters were averaged to give $P_{beam} = 0.810 \pm 0.02$ for the entire experiment. The measured asymmetry can be overestimated by a few percent due to the motion of the atomic electrons in the magnetized iron foil targets and is known as the Levchuk effect [91]. Detector resolution, detector gap, bremsstrahlung and Levchuk effects were taken into account in the Møller analyses.

3.3.5 Target Polarization

The fact that the polarized targets were not 100% polarized was corrected for by applying the target polarization factor P_t to the raw asymmetry. During the course of the experiment, the protons in $^{15}NH_3$ and deuterons in ^6LiD were polarized along (against) and right (left) transverse to the electron beam helicity. The whole target magnet system was simply rotated 90° to switch between longitudinal and transverse running. Figure (3.2) shows the target polarization versus run number for parallel running. Typical target polarizations were $-1.0 < P_p < -0.60$ and $0.60 < P_p < 0.85$ for the proton and $-0.26 < P_d < -0.10$ and $0.10 < P_d < 0.30$ for the deuteron.

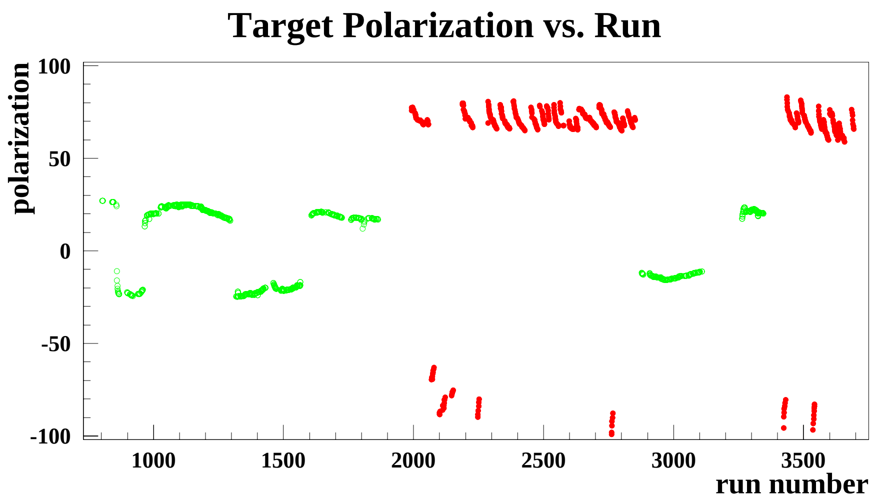

Figure 3.2: **Target Polarization versus Run** The open circles represent the proton polarization in $^{15}NH_3$ ($> 60\%$) and the solid circles represents the deuteron polarization in ^6LiD ($< 30\%$) during parallel running.

3.3.6 Dilution Factor

The goal of this experiment was to measure the scattering of polarized electrons off polarized protons or deuterons. However, our polarized target did not consist of *pure* protons or deuterons. What our spectrometers actually saw were scattering events off the target protons (deuterons) diluted with scattering events off the ^{15}N (^6Li) nuclei in the target material and other unpolarized materials in the beamline and target apparatus (aluminum windows, LHe, and other materials). The materials found within the acceptance of the spectrometers are listed in table (3.4). These unpolarized materials served to *dilute* the physics asymmetry. The ratio of scattering events from the proton (deuteron) in ammonia (lithium deuteride) over the total number of events from all materials within the acceptance of our spectrometers is

Component	**Material Length**	**Z-Range (cm)**	$Z_{C(2)}$	$Z_{C(5)}$	$Z_{C(10)}$
beam exit	0.00300in Al	-59	0.90	0.53	0.20
air entr	10.00000cm Al	$-59 < air < -49$	0.90	0.56	0.30
ovc entr	0.00325in Al	-49	0.90	0.61	0.40
LN2 shield	0.00150in Al	-42	0.95	0.67	0.60
4K shield	0.00100in Al	-4	1.00	1.00	1.00
tail#3	0.00500in Al	-1.69	1.00	1.00	1.00
LHe	0.07550in He	$-1.69 < LHe < -1.5$	1.00	1.00	1.00
endcap entr	0.00100in Al	-1.5	1.00	1.00	1.00
^{6}Li(^{15}N)	pf×3.0cm tgt	$-1.5 < tgt < +1.5$	1.00	1.00	1.00
^{2}H(^{1}H$_3$)	pf×3.0cm tgt	$-1.5 < tgt < +1.5$	1.00	1.00	1.00
^{7}Li(^{14}N)	pf×3.0cm tgt	$-1.5 < tgt < +1.5$	1.00	1.00	1.00
^{2}H(^{1}H$_3$)	pf×3.0cm tgt	$-1.5 < tgt < +1.5$	1.00	1.00	1.00
^{6}Li(^{15}N)	pf×3.0cm tgt	$-1.5 < tgt < +1.5$	1.00	1.00	1.00
^{1}H(^{2}H$_3$)	pf×3.0cm tgt	$-1.5 < tgt < +1.5$	1.00	1.00	1.00
^{7}Li(^{14}N)	pf×3.0cm tgt	$-1.5 < tgt < +1.5$	1.00	1.00	1.00
^{1}H(^{2}H$_3$)	pf×3.0cm tgt	$-1.5 < tgt < +1.5$	1.00	1.00	1.00
LHe	(1-pf)×3.0cm tgt	$-1.5 < tgt < +1.5$	1.00	1.00	1.00
NMR coil Al	varies	$-1.5 < tgt < +1.5$	1.00	1.00	1.00
NMR coil Cu	varies	$-1.5 < tgt < +1.5$	1.00	1.00	1.00
NMR coil Ni	varies	$-1.5 < tgt < +1.5$	1.00	1.00	1.00
endcap exit	0.00100in Al	$+1.5$	1.00	1.00	1.00
LHe	0.07550in He	$+1.5 < LHe < +1.69$	1.00	1.00	1.00
tail#3	0.00500in Al	$+1.69$	1.00	1.00	1.00
4K shield	0.00100in Al	$+4$	1.00	1.00	1.00
LN2 shield	0.00150in Al	$+42$	0.95	0.67	0.20
ovc exit	0.00400in Al	$+49$	0.90	0.61	0.10
air exit	5.00000cm Al	$+49 < air < +54$	0.90	0.58	0.00
He bag entr	0.00100in Al	$+54$	0.90	0.56	0.00
He gas	27.00000cm He	$+54 < gas < +81$	1.00	0.60	0.00

Table 3.4: **E155 Target's Typical Components** The Z position is given along the beamline, negative values representing upstream and positive values representing downstream components in centimeters from the center of target cell. The last three columns contain factors by which the material thickness is effectively reduced due to variation in spectrometer acceptance along the beamline for the 2.75, 5.5 and 10.5 degree, respectively.

called the dilution factor:

$$f = \frac{N_t \sigma_t}{N_t \sigma_t + \sum\limits_i N_i \sigma_i} \cdot \frac{U_{RC}^{\text{all}}}{U_{RC}^{\text{H}}} \tag{3.12}$$

where N_t is the number of free target nucleons and σ_t is the unpolarized Born cross-section for the target nucleons, whereas N_i and σ_i are the sum over all the non-target nucleons, which include the nucleons in ^{15}N in the proton target and the nucleons in other materials such as the beam windows and the target LHe bath. U_{RC}^{all} and U_{RC}^{H} are unpolarized radiative corrections which serve to "radiate" each Born cross-section σ to the experimental conditions of the measured raw asymmetry. The concept behind these corrections are discussed in more detail in sections (3.3.10) and (C.1). The unpolarized radiative corrections used in the dilution factor calculation are shown in figures (3.5) and (3.6).

Table (3.4) also shows the factors (last three columns) by which the thickness of each material had to be effectively reduced due to variation in acceptance along the beam path for each spectrometer. The Z-factor correction increased the dilution factor by 0.5%, 2% and 5% for the 2.75, 5.5, and 10.5 degree spectrometers, respectively. In addition, the dilution factor for ^{6}LiD included a 3.3%±1.5% correction due to oxygen contamination [see section (D.4)] which decreased the value of f. The fully corrected dilution factors for $^{15}NH_3$ and ^{6}LiD are shown in figures (3.3) and (3.4) and a derivation of the dilution factor is presented in section (C.1).

3.3.7 Target Thickness

The dilution factor calculation required knowledge of the target thickness. However, this thickness was not readily known since the frozen targets existed in the form of

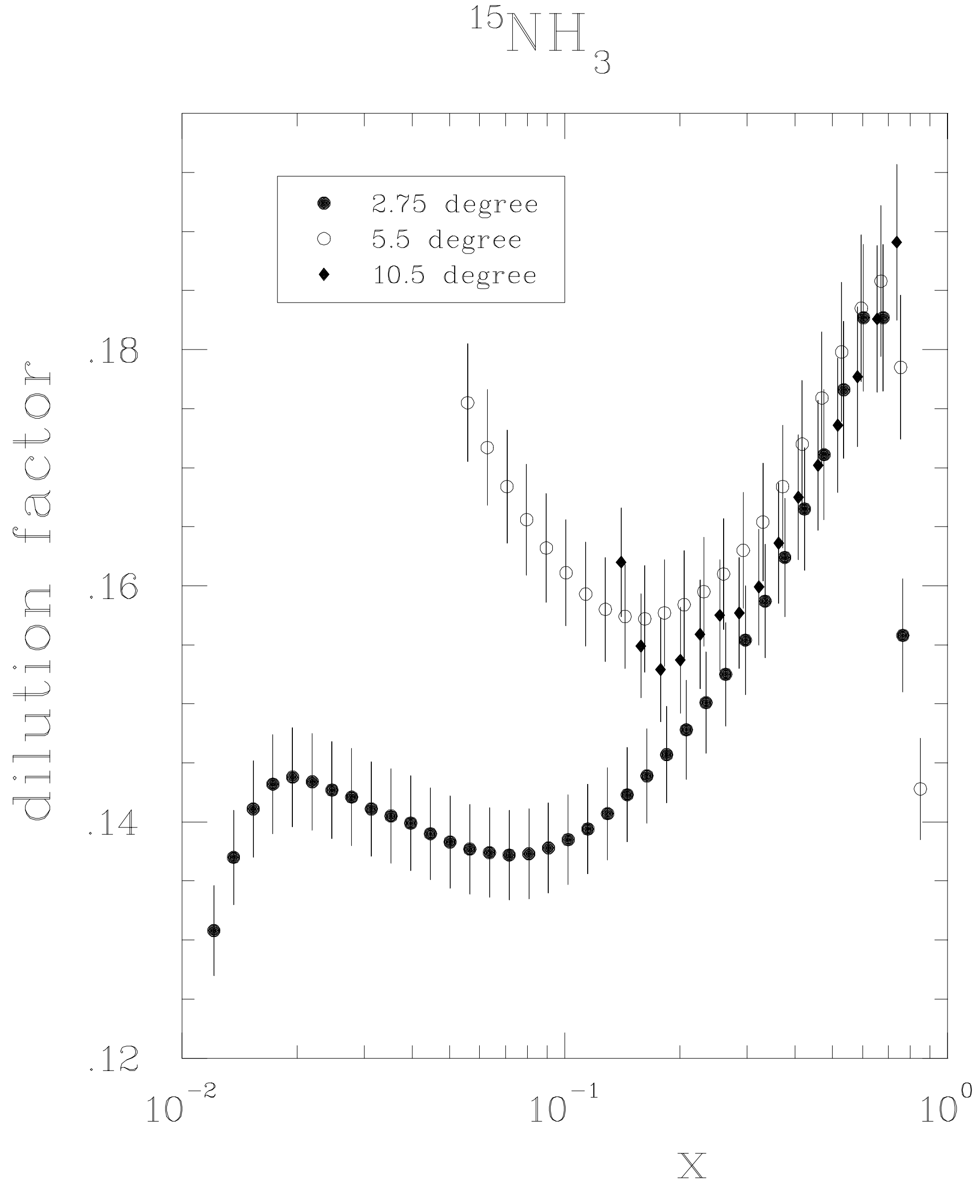

Figure 3.3: **Dilution Factor for Ammonia** The $^{15}NH_3$ f calculation, plotted against fine-x-bins. For clarity, the 2.75 (10.5) degree results are offset from the central x-bin value by -(+)0.1 x.

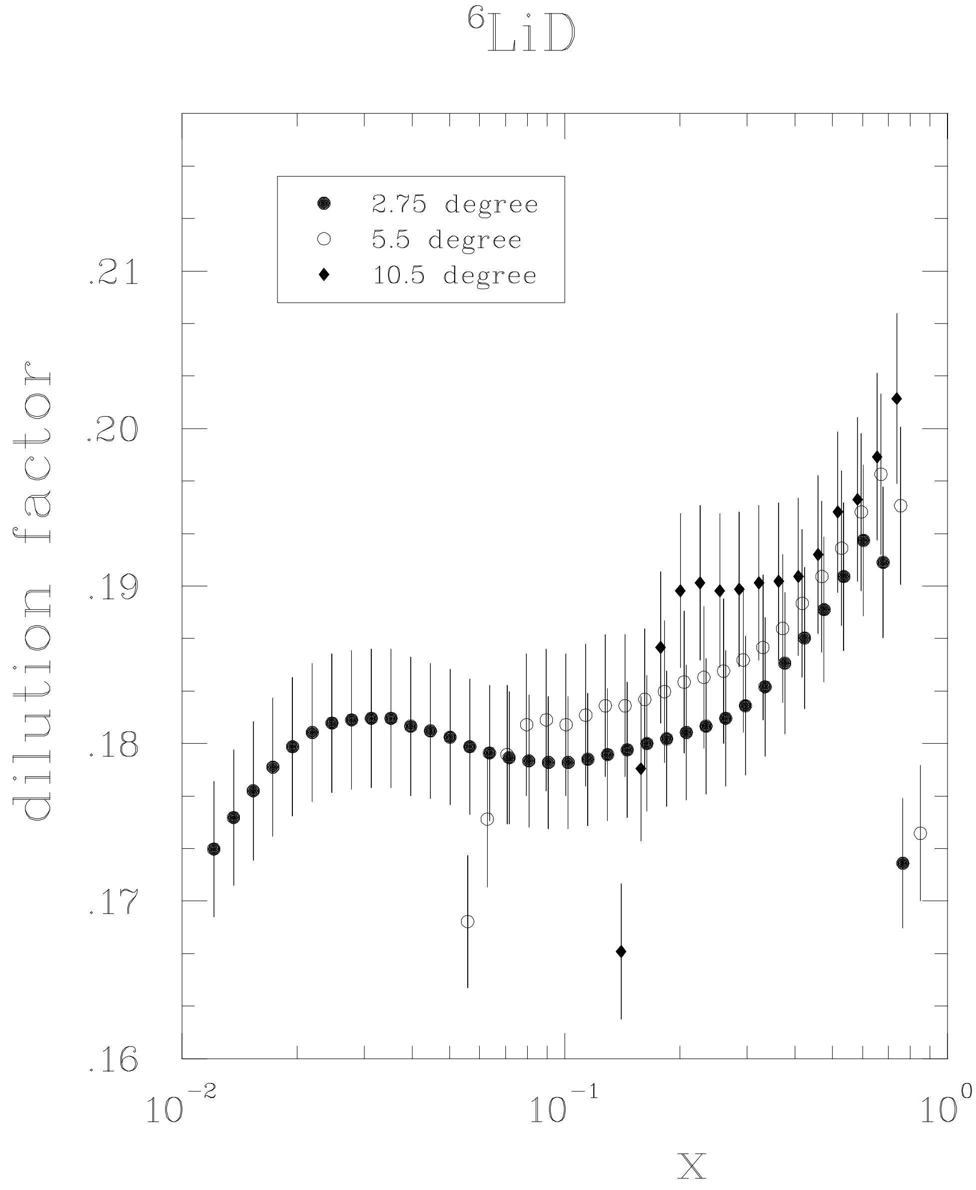

Figure 3.4: **Dilution Factor for Lithium Deuteride** The ^{6}LiD f calculation, plotted against fine-x-bins. For clarity, the 2.75 (10.5) degree results are offset from the central x-bin value by -(+)0.1 x.

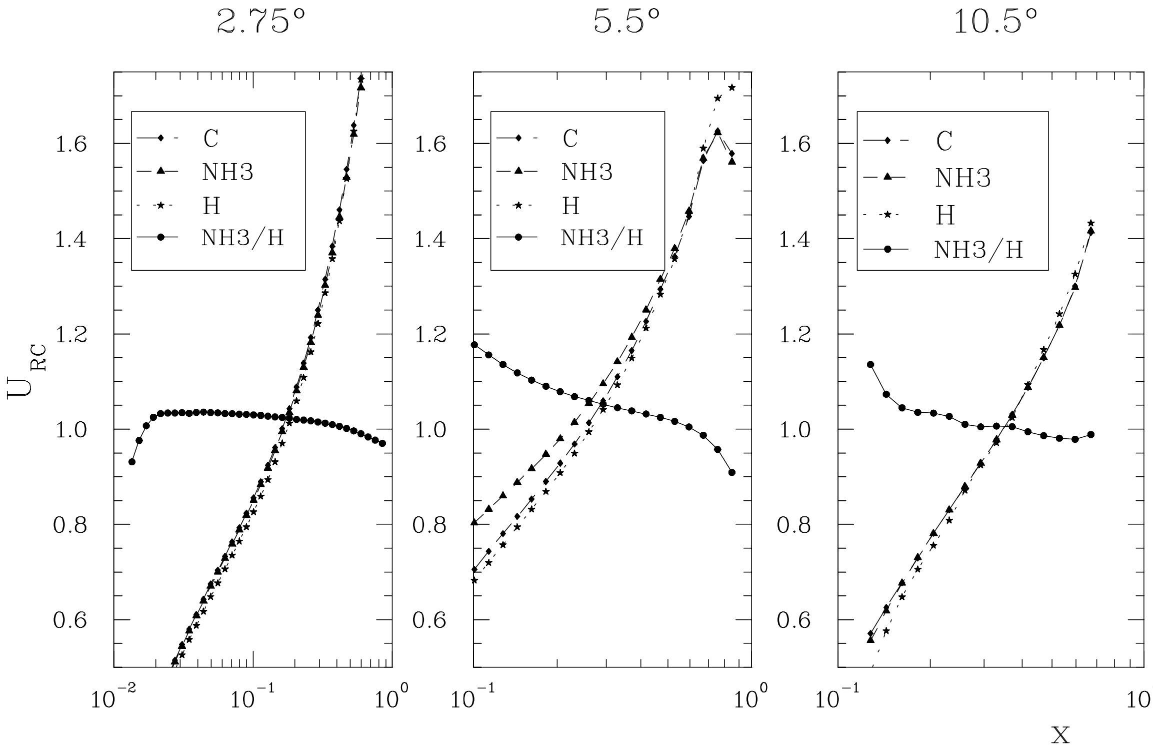

Figure 3.5: **Unpolarized Radiative Corrections for Ammonia**

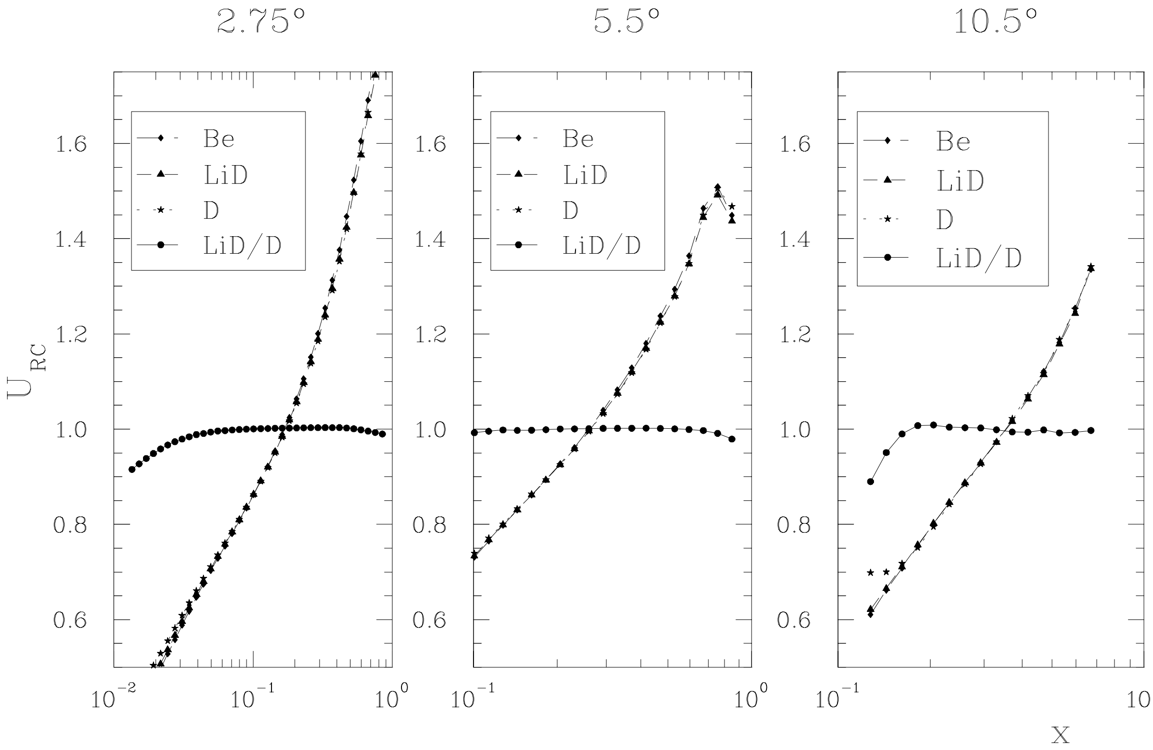

Figure 3.6: **Unpolarized Radiative Corrections for Lithium Deuteride**

irregularly shaped granules loaded in cells that were immersed in liquid ^{4}He. The fraction of the target cell that was occupied by ^{15}NH$_3$ or ^{6}LiD was defined as the *packing fraction* for the target.

The packing fraction could not be determined directly by geometry, so a "rate method" was employed which determined the ratio of measured rates off ^{15}NH$_3$ (^{6}LiD) targets and the measured rates off reference carbon (beryllium) disks and compared it to a rate model similar to that used in the dilution factor calculation [see section (C.1)] [61]:

$$\frac{R_{\mathrm{NH3}}}{R_{\mathrm{12C}}} \cdot \frac{U_{RC}^{\mathrm{NH3}}}{U_{RC}^{\mathrm{C}}} = \frac{R_p + R_{\mathrm{15N}} + R_{\mathrm{4He}} + R_{\mathrm{coil}} + R_{\mathrm{unpol}}}{R_{\mathrm{12C}} + R'_{\mathrm{4He}} + R_{\mathrm{unpol}}} \tag{3.13}$$

$$\frac{R_{\mathrm{LiD}}}{R_{\mathrm{9Be}}} \cdot \frac{U_{RC}^{\mathrm{LiD}}}{U_{RC}^{\mathrm{Be}}} = \frac{R_d + R_{\mathrm{6Li}} + R_{\mathrm{4He}} + R_{\mathrm{coil}} + R_{\mathrm{unpol}}}{R_{\mathrm{9Be}} + R'_{\mathrm{4He}} + R_{\mathrm{unpol}}} \tag{3.14}$$

where R_{4He} is the event rate from the LHe in the target cell, R'_{4He} is the rate from LHe when the reference target was used, R_{coil} is the rate from the Al or CuNi NMR coils that were embedded in the target cell, R_{unpol} is the rate from all the other materials in the beamline and U_{RC}^{X} is the unpolarized radiative corrections for material X. The packing fraction (pf) is included in expressions for the modeled rates R_p (R_d), R_{15N} (R_{6Li}) and R_{4He} by defining the thickness of ^{15}NH$_3$ (^{6}LiD) as 3.0 cm×pf and the thickness of LHe as 3.0 cm×(1-l_{coil}-pf), where l_{coil} is the NMR coil thickness.

Each reference target was matched as closely as possible in grams of material and radiation length to its polarized target partner in order to minimize the differences in radiative corrections and rate dependent spectrometer efficiency. Unpolarized radiative corrections were applied to the measured (radiated) rates so they can be directly compared to the calculated Born rates via: $R_{Born} = R_{rad} \cdot U_{RC}$. More information on radiative corrections can be found in section (3.3.10).

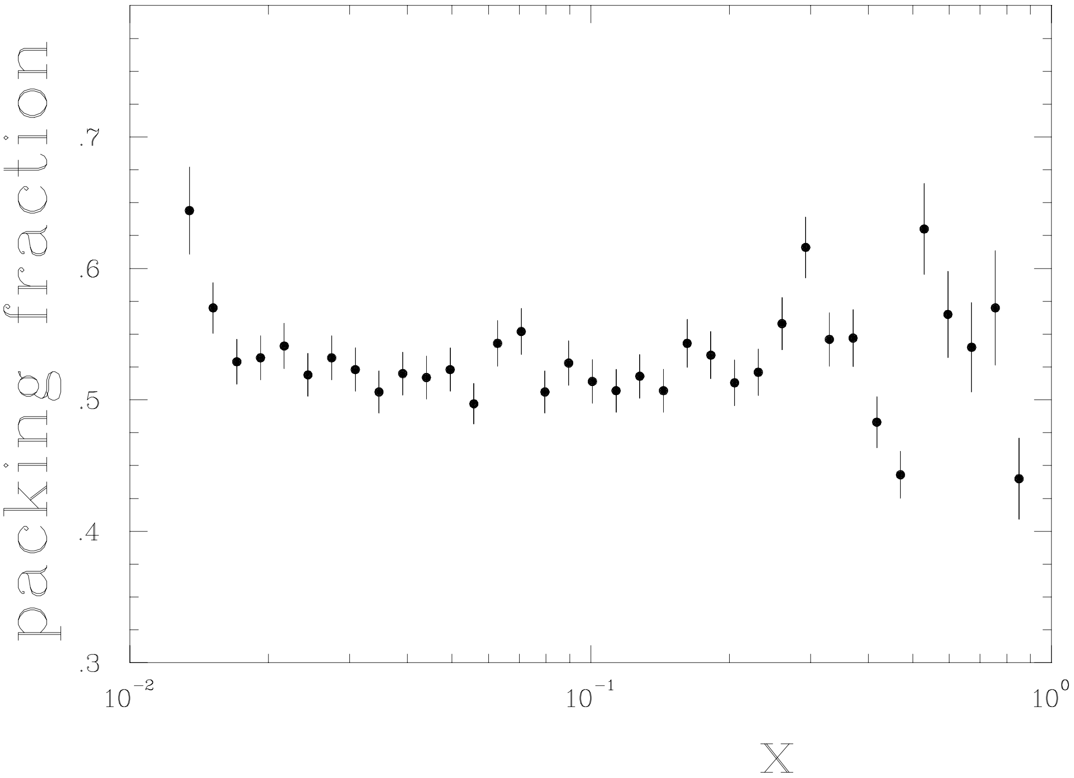

Figure 3.7: **Packing Fraction Measurement vs. x-bin** This plot shows a typical distribution of extracted packing fraction values vs. x using rate studies for LiD in the 2.75 degree spectrometer.

Equation (3.13) or (3.14) can be solved for the packing fraction in terms of the measured and calculated rates. Since the packing fraction is a measure of the target thickness, it should not depend on x. Therefore, a plot pf vs. x should ideally be flat. Figure (3.7) shows a typical packing fraction distribution against x. The final packing fractions for each target cell were determined by averaging the packing fractions over all the x-bins for several runs for each spectrometer, and then averaging the spectrometer results which are given in table (3.5). Table (C.2) presents a history of the target cells used during E155.

Insert	Cup	Matl	Packing Fraction
1	Upper	LiD	$0.526 \pm .013$
1	Lower	LiD	$0.575 \pm .013$
2	Lower	NH3	$0.584 \pm .031$
3	Upper	NH3	$0.570 \pm .019$
3	Lower	NH3	$0.555 \pm .015$
4	Upper	NH3	$0.540 \pm .033$
4	Lower	NH3	$0.586 \pm .021$
5	Upper	LiD	$0.534 \pm .017$
5	Lower	LiD	$0.554 \pm .014$
6	Upper	NH3	$0.594 \pm .017$
6	Lower	NH3	$0.610 \pm .021$
10	Upper	LiD	$0.522 \pm .026$
10	Lower	NH3	$0.583 \pm .040$

Table 3.5: **Combined 2.75 and 5.5 degree Packing Fractions**

3.3.8 Nuclear Corrections

Our solid target materials contain polarizable nuclei other than the intended target proton or deuteron. Nuclei such as ^{15}N in ammonia and ^{6}Li in lithium deuteride can be significantly spin aligned and contribute to the measured spin asymmetries. Therefore, the spin properties of these additional nuclear species must be known and corrected for before a pure electron-proton (deuteron) spin asymmetry can be extracted from the measured asymmetry. These effects are handled using the nuclear correction terms C_1 and C_2 via:

$$A_p^{corr} = \frac{A_{raw}}{f P_b P_t C_1} + C_2 A_d \tag{3.15}$$

$$A_d^{corr} = \frac{A_{raw}}{f P_b P_t C_1} + C_2 A_p \tag{3.16}$$

where C_1 modifies the measured asymmetries for additional polarized nucleons that are the *same* type as the target nucleon, C_2 takes into account additional polarizable nucleons that are *different* from the target nucleon, A_d (A_p) is the asymmetry expected from the *other than target* polarizable nucleons and A_p^{corr} (A_d^{corr}) is the corrected asymmetry *before* any backgrounds are subtracted and the radiative corrections are applied. Details on how to derive the correction factors used for the E155 analysis can be found in the article by Rondon [92]. Some spin properties of the nuclear species found in the E155 target materials are listed in table (2.7).

Ammonia Nitrogen Correction

The proton target $^{15}\mathrm{NH}_3$ consisted of $^1\mathrm{H}$, $^{14}\mathrm{N}$ and $^{15}\mathrm{N}$. The three hydrogen nuclei of $^{15}\mathrm{NH}_3$ were considered the main nuclear target. However, additional polarized protons from the unpaired proton in $^{15}\mathrm{N}$ contributed to the measured asymmetry and was corrected for by way of the C_1 term:

$$C_1 = 1.0 - \left(1 - \eta_{14\mathrm{N}}\right)\left(\frac{1}{3}\right)\left(\frac{P_{15\mathrm{N}}}{P_p}\right)\beta_{15\mathrm{N}} g_{\mathrm{emc}}^{15\mathrm{N}} \tag{3.17}$$

$$C_2 = 0. \tag{3.18}$$

Nucleons that were not polarized protons entered by way of the C_2 term from a small two percent $^{14}\mathrm{N}$ contamination in $^{15}\mathrm{NH}_3$, which was set to zero since its effect was negligible. All the terms in the above expressions for C_1 and C_2 are described in table (3.6). For the ammonia target, $^{15}\mathrm{N}$ was chosen as the preferred nitrogen isotope over $^{14}\mathrm{N}$ since all the neutrons in $^{15}\mathrm{N}$ are paired, making a negligible neutron asymmetry, and the $^{15}\mathrm{N}$ NMR signal is more easily measured than the broad $^{14}\mathrm{N}$ signal. The polarization relationship between the proton and $^{15}\mathrm{N}$ was determined by measuring and comparing P_p and $P_{15\mathrm{N}}$ in technical runs performed by the target group after E143 [29] and E155:

$$P_{15\mathrm{N}} = -\biggl(0.136P_p - 0.183P_p^2 + 0.335P_p^3\biggr). \tag{3.19}$$

PROTON	VALUE	DESCRIPTION
$\eta_{14\mathrm{N}}$	0.02	concentration of ^{14}N in nitrogen
$P_{15\mathrm{N}}$	equation (3.19)	^{15}N polarization determined from P_{p}
P_p	measured	proton polarization
$\beta_{15\mathrm{N}}$	-1/3	effective proton polarization in ^{15}N
$g_{\mathrm{emc}}^{15\mathrm{N}}(x)$	~ 1	EMC effect for ^{15}N
1/3 term	1/3	ratio of nitrogen to hydrogen in ammonia
DEUTERON	**VALUE**	**DESCRIPTION**
η_p	0.025	contamination of ^{1}H in D
$\eta_{7\mathrm{Li}}$	0.046	concentration of ^{7}Li in lithium
P_{p}	0.04	proton polarization in ^{6}LiD
P_{d}	measured	deuteron polarization in ^{6}LiD
$P_{6\mathrm{Li}}$	$\sim P_{\mathrm{d}}$	^{6}Li polarization via EST
$P_{7\mathrm{Li}}$	$\sim 3P_{\mathrm{d}}$	^{7}Li polarization via EST
$\beta_{6\mathrm{Li}}$	0.866	effective deuteron polarization in ^{6}Li
$\beta_{7\mathrm{Li}}$	2/3	effective proton polarization in ^{7}Li
$g_{emc}^{6\mathrm{Li}}(x)$	≈ 1	EMC effect for ^{6}Li
$g_{emc}^{7\mathrm{Li}}(x)$	≈ 1	EMC effect for ^{7}Li
$F_2^p(x)/2F_2^d(x)$	x-dependent	ratio of spin averaged structure functions
ω_D	0.05 ± 0.01	D-state probability of the deuteron

Table 3.6: **Proton and Deuteron Nuclear Corrections**

Note that $P_{15\mathrm{N}}$ and P_p have opposite signs so that C_1 is positive.

Lithium Deuteride Nuclear Correction

The deuteron target ^{6}LiD is made up of ^{1}H, ^{2}H, ^{6}Li and ^{7}Li. Any polarized protons in ^{6}LiD due to the unpaired proton in ^{7}Li and the LiH contamination were corrected for by way of a significant C_2 term, whereas, the additional polarizable effective deuteron contribution from ^{6}Li was corrected for by way of the C_1 term:

$$C_1 = \left(1 - \eta_p\right) + \left(1 - \eta_{7\mathrm{Li}}\right)\left(\frac{P_{6\mathrm{Li}}}{P_d}\right)\left(\frac{1}{1 - \frac{3}{2}\omega_D}\right)\beta_{6\mathrm{Li}} g_{\mathrm{emc}}^{6\mathrm{Li}} \tag{3.20}$$

$$C_2 = -\frac{1}{C_1}\left[\eta_p \frac{P_p}{P_d} + \eta_{7\mathrm{Li}} \frac{P_{7\mathrm{Li}}}{P_d} \beta_{7\mathrm{Li}} g_{\mathrm{emc}}^{7\mathrm{Li}} \left(\frac{F_2^p}{2F_2^d}\right)\right] \tag{3.21}$$

The terms in the above expressions for C_1 and C_2 are described in table (3.6). To first order, ^{6}Li can be considered a polarized deuteron plus an unpolarized alpha. The effective deuteron polarization, $\beta_{6\mathrm{Li}} = 0.866$, in ^{6}Li was determined from an average of several models of the lithium nucleus [92].

3.3.9 Positron and Pion Contamination

This section is concerned with only the particle background in the electron and positron asymmetry measurements. In the electron runs, a fraction of the electron events detected in the spectrometers were not DIS electrons, but were either e^- created from charge-symmetric processes (positron-electron pairs) or charged hadrons (mostly π^-) produced through beam-target interactions. The electrons from non-DIS events had to be accounted for by detecting their pair-e^+ via positron runs. In these measurements, the positron events were contaminated by charged hadrons (mostly π^+). In both cases, most of the hadron background was distinguished from $e^-(e^+)$ by applying appropriate data cuts.

Positron Asymmetry

The charge-symmetric processes include the decay of real photons to positron-electron pairs and the decay of neutral pions to photons via

$$\gamma \longrightarrow e^{+}e^{-} \tag{3.22}$$

$$\pi^{0} \longrightarrow \gamma\gamma \longrightarrow \gamma e^{+}e^{-}. \tag{3.23}$$

In the first case, the real photons are produced by electrons emitting bremsstrahlung radiation as they travel through the target. The neutral pions are created from nuclear fragmentation of the target.

These pair-produced electrons cannot be distinguished from DIS electrons in the spectrometers and therefore had to be measured by reversing the polarity of the spectrometer magnets and detecting the rate of positrons. If one assumes the positrons detected came from $e^{+}e^{-}$ production only, then the fraction of pair-symmetric electrons in the total electron data pool ($n_{e^{+}}$) could be determined and used to correct the measured asymmetry. The measured ratio of positrons to electrons for each x-bin indicated a significant background at low x, but overall produced only a small charge-symmetric background asymmetry correction which would slightly increase the asymmetry.

Pion Asymmetry

In the process of DIS not only electrons are scattered but many particles are produced through nuclear fragmentation [hadron debris X from equation (1.5)]. As a result, hadrons (pions, kaons and protons) were produced at rates greater than DIS electrons. Hence, most of the track events in the spectrometers were not electrons, but hadrons, of which the electro-produced pions dominated. For a given x-bin, the ratio of hadron to electron tracks was about 3/1 (10/1) for the 2.75 (5.5) degree spectrometer. Since kaons and protons were produced at rates 10 times smaller than pions, this section refers to the hadron background as *pions*.

Most of the background was eliminated by applying appropriate cuts to the data that distinguished electrons from pions. However, there still was a small statistical chance that a fraction of the pion events might meet the electron definition cuts. To correct for this *pion contamination*, one had to determine the fraction of pions misidentified as electrons (n_{π_-}). This was accomplished by determining the distribution of pions in the spectrometer via a pion definition (similar to the electron definition, but did not require a Cherenkov hit and limited $E^{'}/p < 0.2$) and fitting to its shape. This fit was then normalized to the electron distribution in the range $0.2 \leq E^{'}/p \leq 0.4$ and subtracted from the full electron distribution. A similar procedure was carried out for the positron runs to determine the fraction of pions (n_{π_+}) that contaminated the positron event data set. Moreover, the pion asymmetries A_{π_-} and A_{π_+} were extracted using the same pion cuts defined above.

The pion and positron asymmetries and contaminations were then used to correct the measured electron asymmetry using [82, 93]:

$$A_{e^-}^{corr} = \frac{1}{n_{e^-}} \left[A_{e^-}^{meas} - \frac{n_{e^+}}{1 - n_{\pi^+}} \left(A_{e^+}^{meas} - n_{\pi^+} A_{\pi^+} \right) - \left(n_{\pi^-} A_{\pi^-} \right) \right] \tag{3.24}$$

where the measured electron and positron asymmetries were related to the true electron, positron and pion asymmetries as follows:

$$A_{e^-}^{meas} = n_{e^-} A_{e^-} + n_{e^+} A_{e^+} + n_{\pi^-} A_{\pi^-} \tag{3.25}$$

$$A_{e^+}^{meas} = (1 - n_{\pi^+}) A_{e^+} + n_{\pi^+} A_{\pi^+}. \tag{3.26}$$

3.3.10 Radiative Corrections

The final corrections to the measured asymmetry involved correcting the electron scattering data for any radiative energy losses and any high-order contributions to the Born DIS process. The formalism used to remove these energy losses and non-Born processes is known as *radiative corrections* (RC).

The RCs were used to correct the unpolarized cross-sections σ for computing the dilution factor [section (3.3.6)] and to correct the experimental asymmetries [equation (3.9)] for computing the spin structure functions. In both correction schemes, two types of processes, known as internal and external, were considered.

External Processes

Before and after the main DIS process, the scattered electrons travel through much material which results in radiative energy losses due mostly to bremsstrahlung. This decreases the effective initial and final energies, E and E', which has to be corrected for if we are to extract the true kinematics and asymmetry of the DIS-electrons. The loss in energy tends to shift the electron events into lower x-bins which will affect the measured asymmetry [61]. The prescription of Tsai [94] was used to calculate *external* radiative corrections to account for these energy loss processes.

Internal Processes

Interactions with the target nucleon which are not first-order (one-photon exchange) Born processes such as vacuum polarization, electron and nucleus vertex corrections and two-photon exchange are known as *virtual* processes. The electron or target nucleon can radiate a real photon during the DIS interaction and is known as internal bremsstrahlung or a *real* process. Figure (3.8) shows the internal processes that were

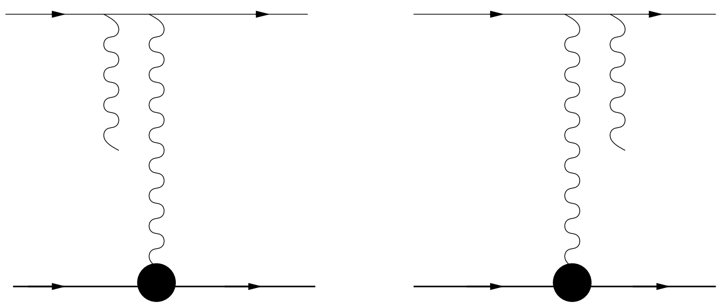

Internal Bremsstrahlung Internal Bremsstrahlung

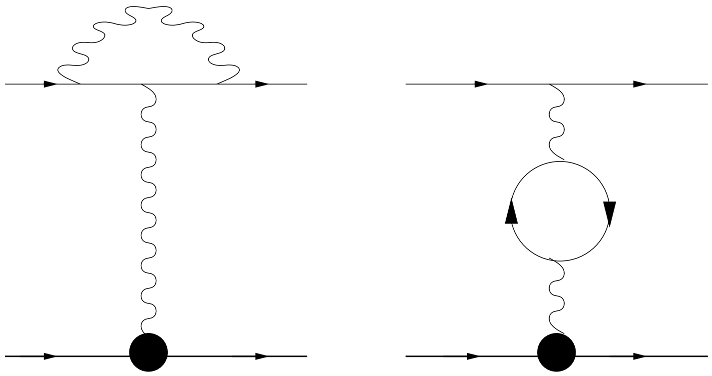

Vertex Correction Vacuum Polarization

Figure 3.8: **Internal Radiative Effects** The top two Feynman diagrams represent real photon processes, while the bottom two are for virtual photon processes.

considered in the calculation of the *internal* radiative corrections up to order α^3, which followed the method by Kuchto and Shumeiko [95].

The radiative corrections were applied to our measured asymmetry as two correction terms: a multiplicative term (f_{RC}) which could be interpreted as a *radiative dilution factor* and an additive term (A_{RC}). As shown in equation (3.9), these RCs were the last corrections applied to the measured asymmetry. The following describes a possible way to interpret the multipicative and additive terms: The radiative dilution factor contains the *unpolarized* RCs which corrects the rates seen in each x-bin due to electron events that were shifted down in x from radiative energy losses. The additive term contains the *polarized* RCs which corrects the spin asymmetry in each x-bin. The change in asymmetry was due to the bremsstrahlung processes which are polarization dependent since the radiation of a real photon changed the polarization state of the incoming electron before it interacted with the nucleon via an exchange of a virtual photon. Together, these RCs bring the radiated asymmetry measured in the experiment to a Born-level asymmetry one can use to extract the spin structure functions.

The radiative corrections were calculated using RCSLACPOL, a program developed by Linda Stuart at SLAC. The code determined the internal and external corrections at the same time. It used various models as input to calculate the Born asymmetry, and then applied radiative effects to determine the radiated asymmetry. The difference between these two effectively gave the desired correction.

Since the code required a Born asymmetry as input, a fit to world data of A_1 was made using the functional form

$$A_1 = x^{\alpha}\left(a + bx + cx^2\right)\left[1 + \frac{\beta}{Q^2}\right]. \tag{3.27}$$

The asymmetries for proton, neutron and deuteron were fit simultaneously using equation (4.7) to connect the proton/neutron to the deuteron. The fit results were used as the initial input to the code and the output fed back as input. The procedure was allowed to iterate (usually < 10 iterations) until the A_{RC} term

$$A_{RC} = A_{Born} - \frac{A_{rad}}{f_{RC}} \tag{3.28}$$

did not change significantly. The final output gave f_{RC} and A_{RC} corrections that

		proton	**deuteron**
Beam Polarization	P_b	2.5%	2.5%
Target Polarization	P_t	7%	4%
Dilution Factor	f	2.5%	2.9%
Nuclear Corrections	C_1	0.5%	2.7%
	C_2	—-	12.6%
π, e^+ Contamination		1%	1%
Radiative Corrections		2.3%	3.6%

Table 3.7: **Relative Contributions to the Systematic Error on** $A_{||}$

increased the asymmetries as much as 30% in the low-x region of the measurement. The details of this radiative corrections calculation can be found in references [83, 96, 97].

3.3.11 Systematic Errors

The error of each correction term was added in quadrature to make up the total systematic error on the final asymmetry measurement. The sources of the systematic error on $A_{||}$ are given in table (3.7), of which the largest contributions came from the target polarization and the radiative corrections. A detailed breakdown can be found in the references [82, 89].

Chapter 4

Results

4.1 Asymmetries

Particle counts are gathered by run and x-bin from which $A_{\|}$ and $A_{\perp}$ are calculated for each spectrometer. The fine binning (SLAC binning) consists of 38 bins over the x range $0.01 \longrightarrow 0.9$, split evenly in $\log(x)$-space. The average x and Q^2 is calculated for each bin along with the average asymmetry for each bin which constitutes the E155 asymmetry measurement. The results are shown for each of the three spectrometers separately in figures (4.1) thru (4.4).

4.2 The g_1 Structure Function

The extracted ratio g_1/F_1 and the structure function g_1 are obtained from the measured asymmetries at the measured x and Q^2 for each spectrometer by way of [16]

$$\frac{g_1}{F_1} = \frac{A_{\|}}{d} + \frac{g_2}{F_1} \cdot \left[\frac{2Mx}{(2E - \nu)} \right], \tag{4.1}$$

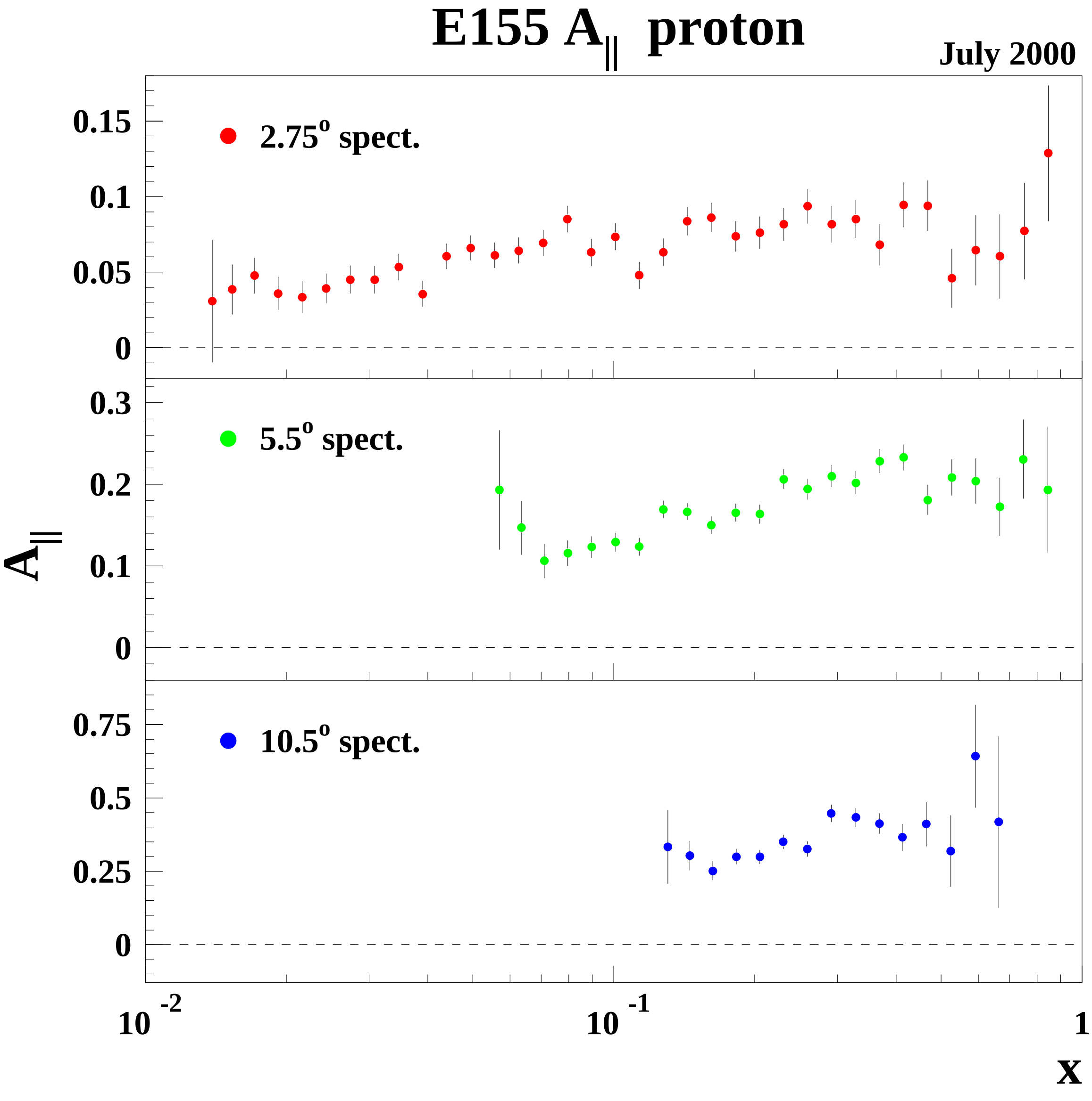

Figure 4.1: **E155 Asymmetry Results $A_{\|}$ Proton**

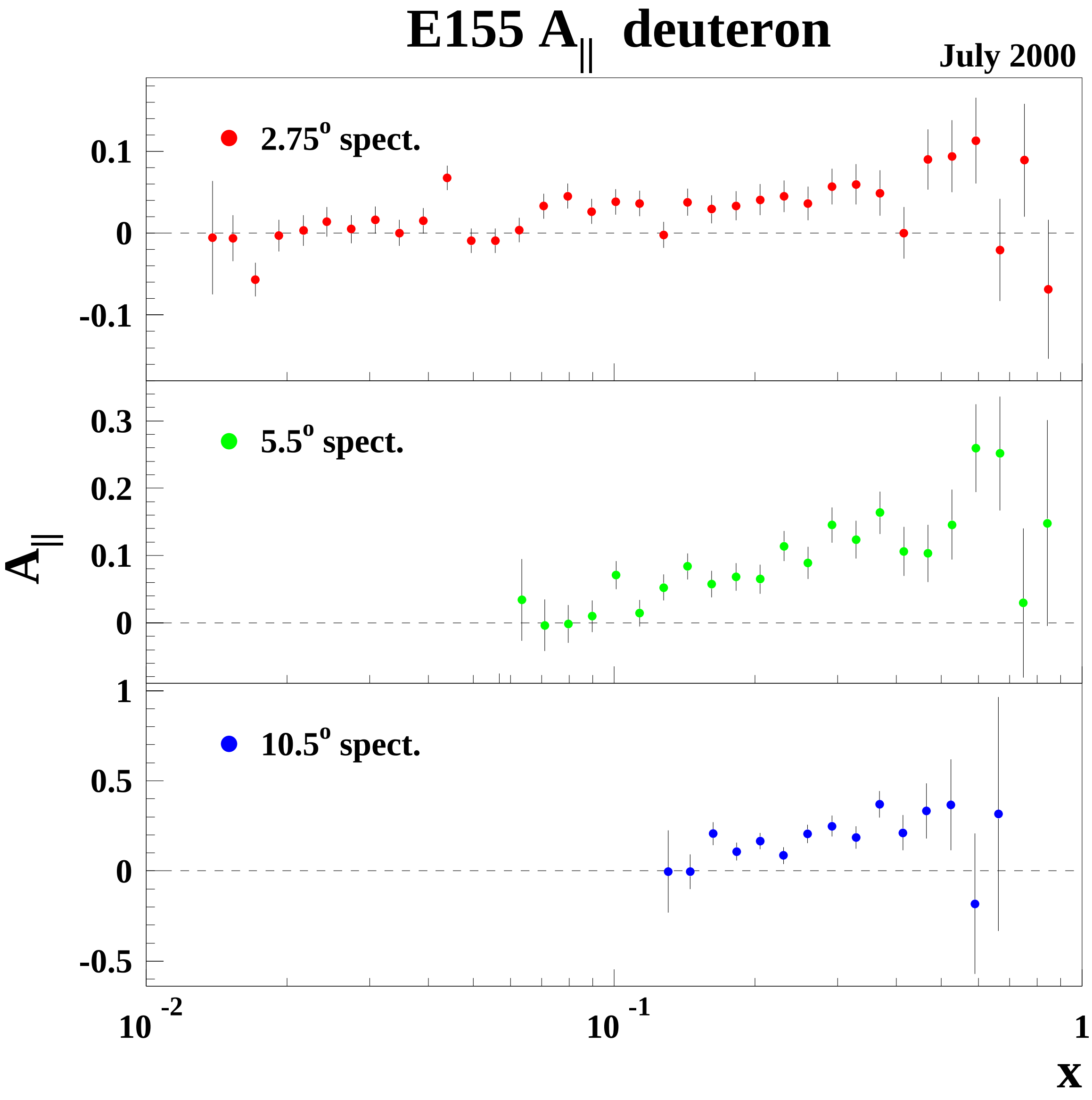

Figure 4.2: **E155 Asymmetry Results $A_{\|}$ Deuteron**

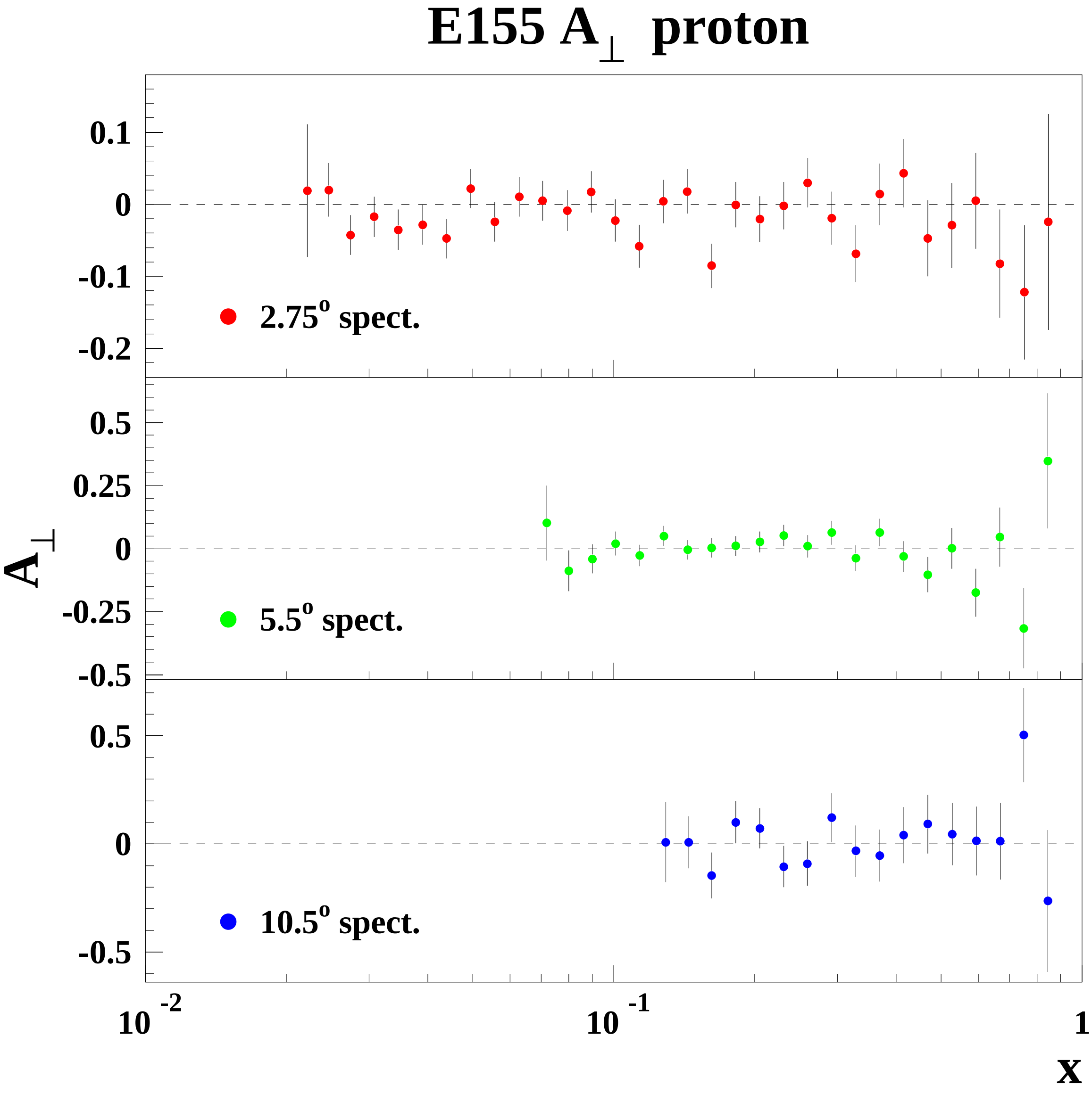

Figure 4.3: **E155 Asymmetry Results $A_\perp$ Proton**

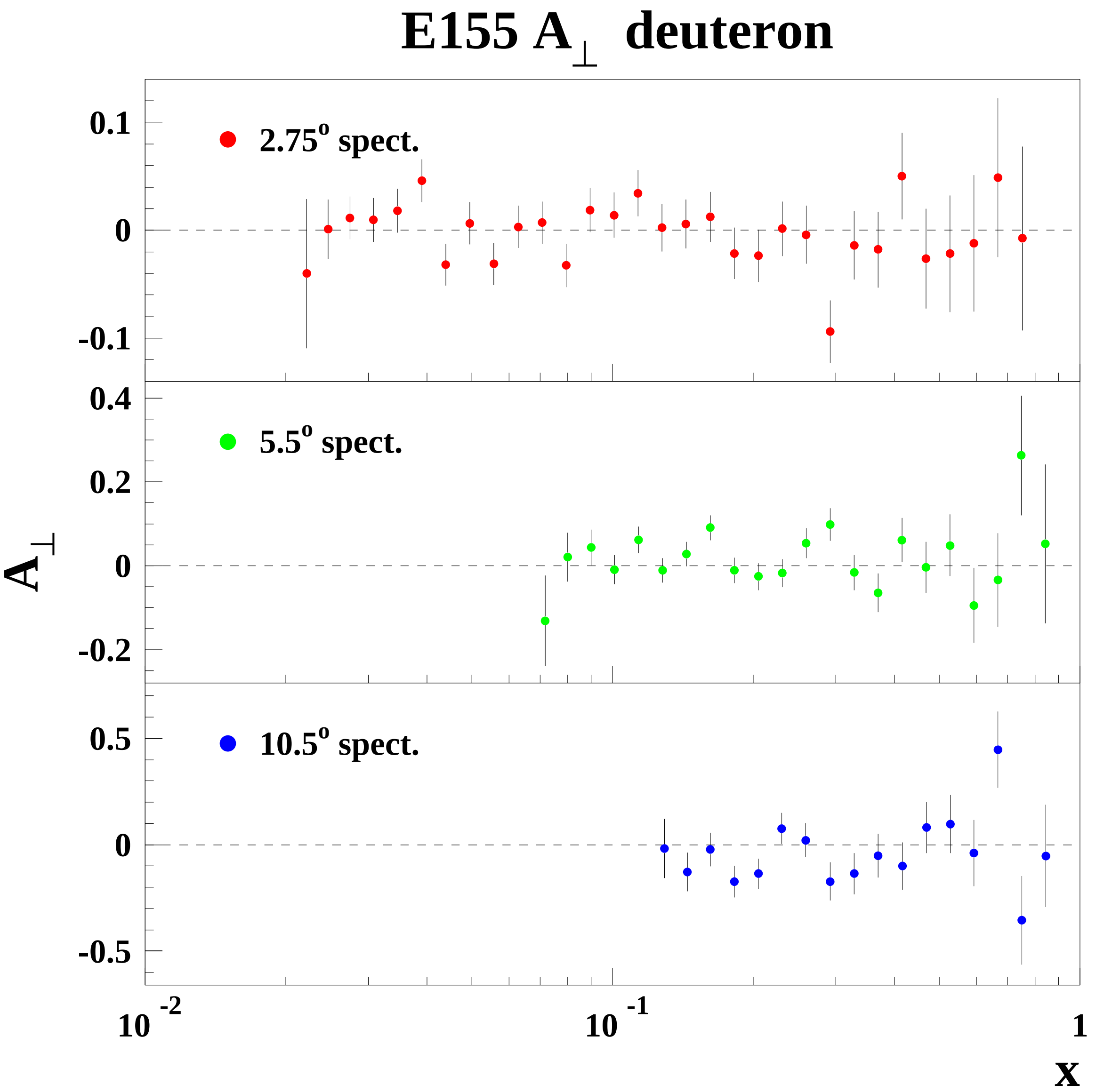

Figure 4.4: **E155 Asymmetry Results $A_\perp$ Deuteron**

where M, d, E and ν are defined in tables (1.1) thru (1.3). Since the E155 $A_\perp$ data was measured at different kinematics than $A_\parallel$, equation (4.1) uses only $A_\parallel$ to determine g_1 and uses the twist-two expression g_2^{WW} for g_2, as described in section(1.6) and equation(1.94). Figures (4.5) thru (4.6) show the extracted g_1 data after averaging the three spectrometers and evolving the data to a common $Q_o^2 = 5$ GeV^2.

Proton and Deuteron g_1 Data

After combining the data from the three spectrometers, the weighted averages $\langle x \rangle$, $\langle Q^2 \rangle$ and $\langle g_1/F_1 \rangle$ (weighted by the statistical error of g_1/F_1) for each of the 38 fine-bins are calculated under the assumption that g_1/F_1 is effectively Q^2-independent within each x-bin. This provides a fine-bin averaged set of data at measured-Q^2 which then is evolved to a common Q_o^2. Several methods can be employed to determine g_1 at a fixed Q_o^2.

- Assume the ratio g_1/F_1 is independent of Q^2. Determine g_1 from

$$g_1(x, Q_o^2) = \frac{g_1(x, Q^2)}{F_1(x, Q^2)} \cdot F_1(x, Q_o^2). \tag{4.2}$$

- Assume the ratio g_1/F_1 has some Q^2-dependence. Determine g_1 from

$$\frac{g_1(x, Q_o^2)}{F_1(x, Q_o^2)} = \frac{g_1(x, Q^2)}{F_1(x, Q^2)} + \left[\left(\frac{g_1}{F_1} \right)^{fit}_{(x, Q_o^2)} - \left(\frac{g_1}{F_1} \right)^{fit}_{(x, Q^2)} \right] \tag{4.3}$$

  where the additive term is determined from empirical fits to world g_1/F_1 data.

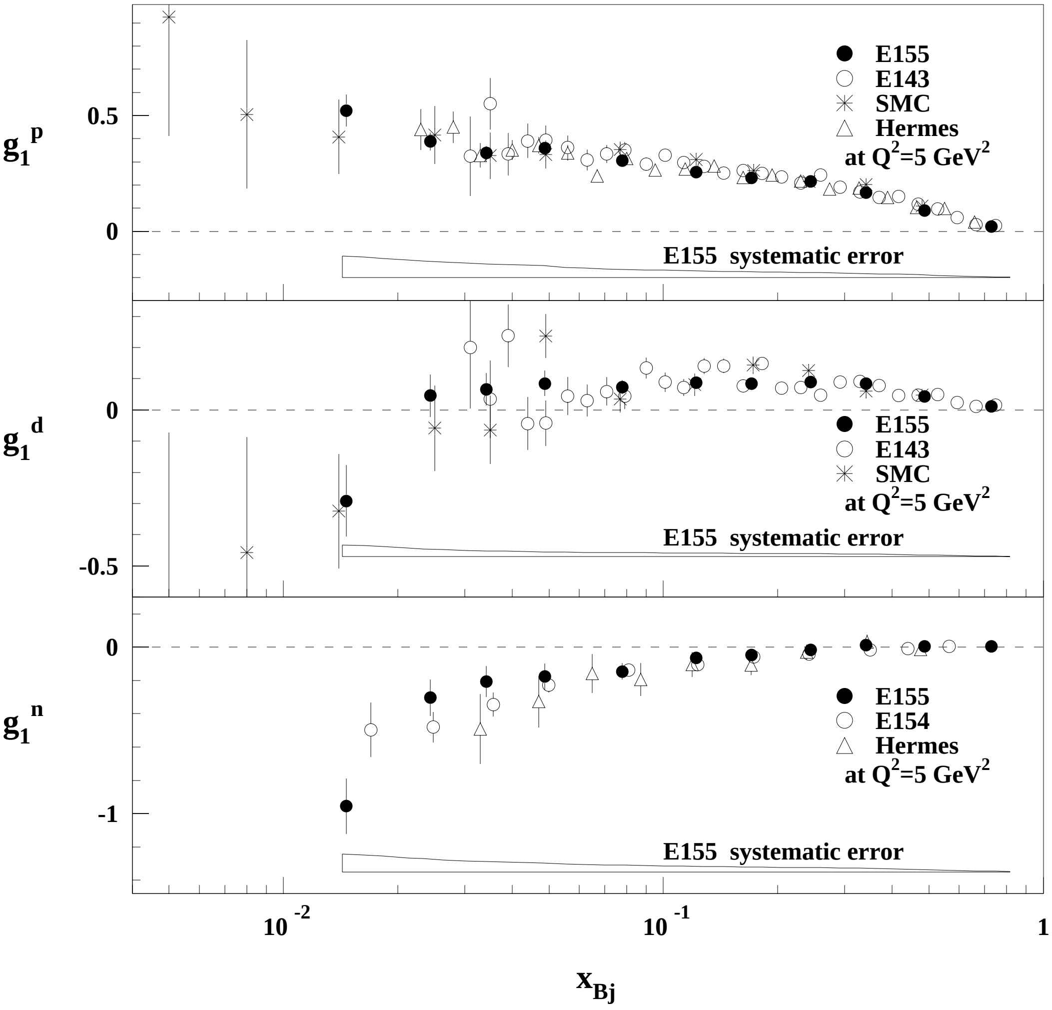

Figure 4.5: **E155 g_1 Results and World Data**

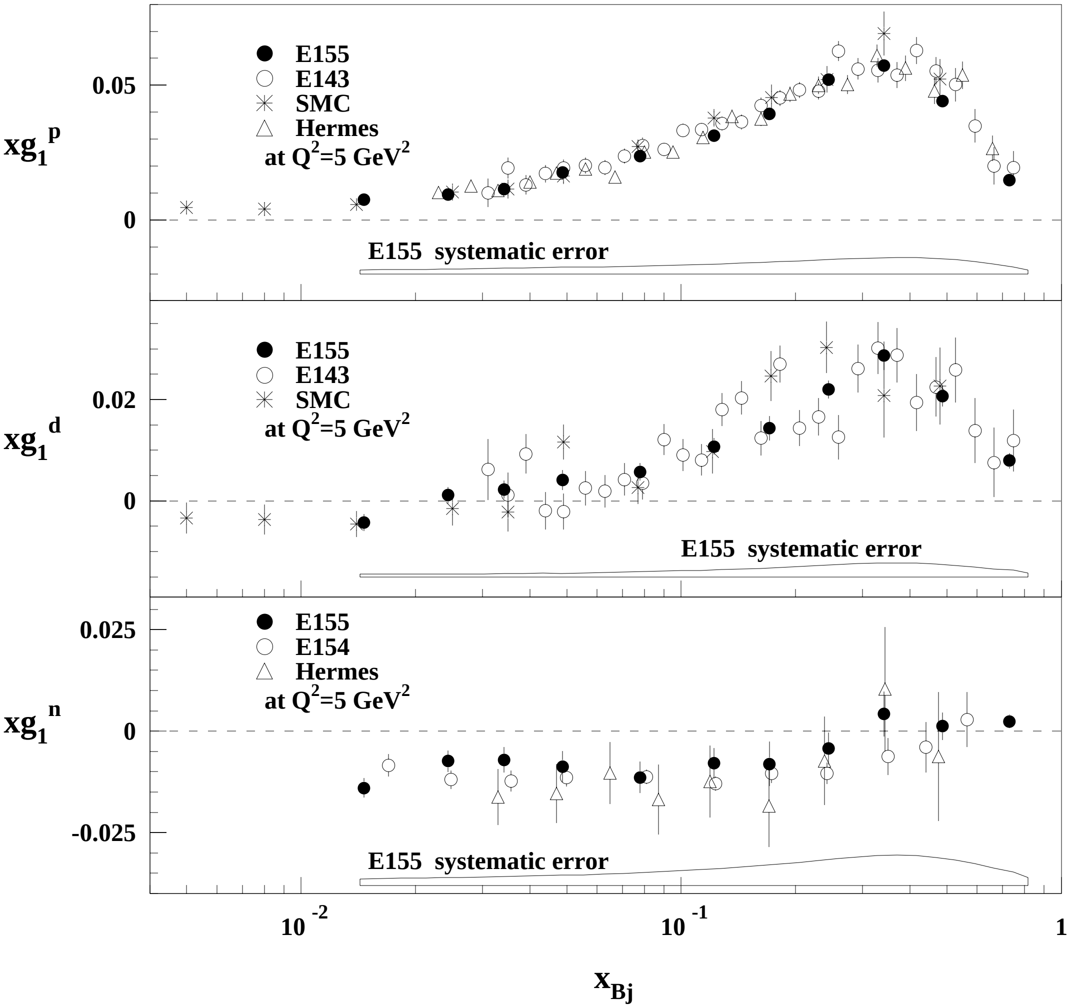

Figure 4.6: **E155 xg_1 Results and World Data**

- Perform an empirical fit to the experiment's g_1/F_1 data and determine g_1 at a fixed Q_o^2 from

$$g_1(x, Q_o^2) = \left(\frac{g_1}{F_1}\right)^{fit}_{(x,Q_o^2)} \cdot F_1(x, Q_o^2). \tag{4.4}$$

For this experiment, the Q^2 evolution of the g_1/F_1 data is accomplished by way of equation (4.3). An empirical fit to world proton, neutron and deuteron data at measured x and Q^2 is made using the form

$$\left(\frac{g_1}{F_1}\right)_{fit} = f(x, Q^2) = x^{\alpha}(a + bx + cx^2)(1 + \beta/Q^2). \tag{4.5}$$

The procedure required fitting the proton, neutron and deuteron data *simultaneously* [96, 97]. The proton and neutron data sets were fitted using equation (4.5) resulting in their own 5-parameter fitted functions. The fit to the deuteron data set was linked to the other two by using

$$\left(\frac{g_1^d}{F_1^d}\right)_{fit} = \frac{1}{2} \cdot \left(1 - \frac{3}{2} \cdot \omega_D\right) \cdot \left[\left(\frac{g_1^p}{F_1^p}\right)_{fit} \cdot F_1^p + \left(\frac{g_1^n}{F_1^n}\right)_{fit} \cdot F_1^n\right] / F_1^d. \tag{4.6}$$

The fit to all three data sets resulted in two functions with a total of only 10 parameters. The simultaneous fit to world proton (EMC, SMC, Hermes, E80, E130, E143, E155), world neutron (E154, E142, Hermes) and world deuteron (E155, E143, SMC) data sets resulted in the fit parameters given in table (4.1).

Extracted E155 g_1 Neutron

The E155 proton and deuteron g_1/F_1 data at measured Q^2 is rebinned into a set of coarse-bins (world-binning) in order to extract a coarse-binned E155 g_1 neutron

parameter	g_1^p/F_1^p	g_1^n/F_1^n
a	0.817	-0.013
b	1.014	-0.330
c	-1.489	-0.761
α	0.700	-0.335
β	-0.037	0.129
χ^2	234.2	17.6
d.f.	247	35

Table 4.1: **E155 Global Fits**

bin	**min x**	**max x**
1	0.010	0.020
2	0.020	0.030
3	0.030	0.040
4	0.040	0.060
5	0.060	0.100
6	0.100	0.150
7	0.150	0.200
8	0.200	0.300
9	0.300	0.400
10	0.400	0.600
11	0.600	0.900

Table 4.2: **World-Binning**

result. Coarse-binning reduces the statistical error on the final neutron results. The coarse-binning consists of 11 bins over $0.010 < x < 0.900$ split as shown in table (4.2) with the centers in the middle of the x range. All the fine-binned g_1/F_1 data that fall between the limits of each coarse-bin are averaged, weighted by their statistical error. The new $\langle g_1/F_1 \rangle$ value at the "measured" $\langle x \rangle$ value is then shifted to the central x value of each bin by evolving the data according to equation (4.3). The proton and deuteron are combined using:

$$g_1^n = 2g_1^d/\big(1 - \frac{3}{2} \cdot \omega_D\big) - g_1^p, \tag{4.7}$$

where $\omega_D = 0.05 \pm 0.01$ is the probability that the deuteron is in the D-state. The neutron result is shown in the bottom plot of figure (4.5).

4.3 Q^2 Dependence of g_1

Although we assume for the most part the ratio g_1/F_1 is Q^2 independent when averaging the data from the three spectrometers, it is evident that there is a significant Q^2 dependence when plotting the coarse-binned g_1 data for each spectrometer as a function of Q^2 at constant x. Figure (4.7) shows plots of the world proton data. Clearly g_1 increases (decreases) with Q^2 at low (high) x. Figures (4.8) and (4.9) show plots of the world data on g_1/F_1 for the proton and deuteron, illustrating a nearly flat dependence. This is reasonable, since g_1 and F_1 are believed to evolve similarly with Q^2. E155 contributes up to three data points to some of the plots, since each of the spectrometers had different $\langle Q^2 \rangle$ for a given x-bin, with the 2.75 (10.5) degree contributing the lowest (highest) $\langle Q^2 \rangle$ for a given world x-bin. F_1 and F_2 are linked by equation (1.36). For example, the Q^2-dependence of F_2 is shown in figures (E.1) and (E.2).

4.4 The g_1 Integral and Sum Rule Results

The E155 results and various fits to the world data allow for an evaluation of the integrals over g_1 which provides a test of the Ellis-Jaffe and Bjorken sum rules and a determination of the net quark polarization $\Delta\Sigma$.

One can obtain the integral of g_1^p and g_1^d over the entire x-range of $0 < x < 1$ at fixed Q_o^2 by piecing together what one knows of g_1 from the measurements made during E155 with kinematics covering $0.014 < x < 0.9$ and using various fits to data

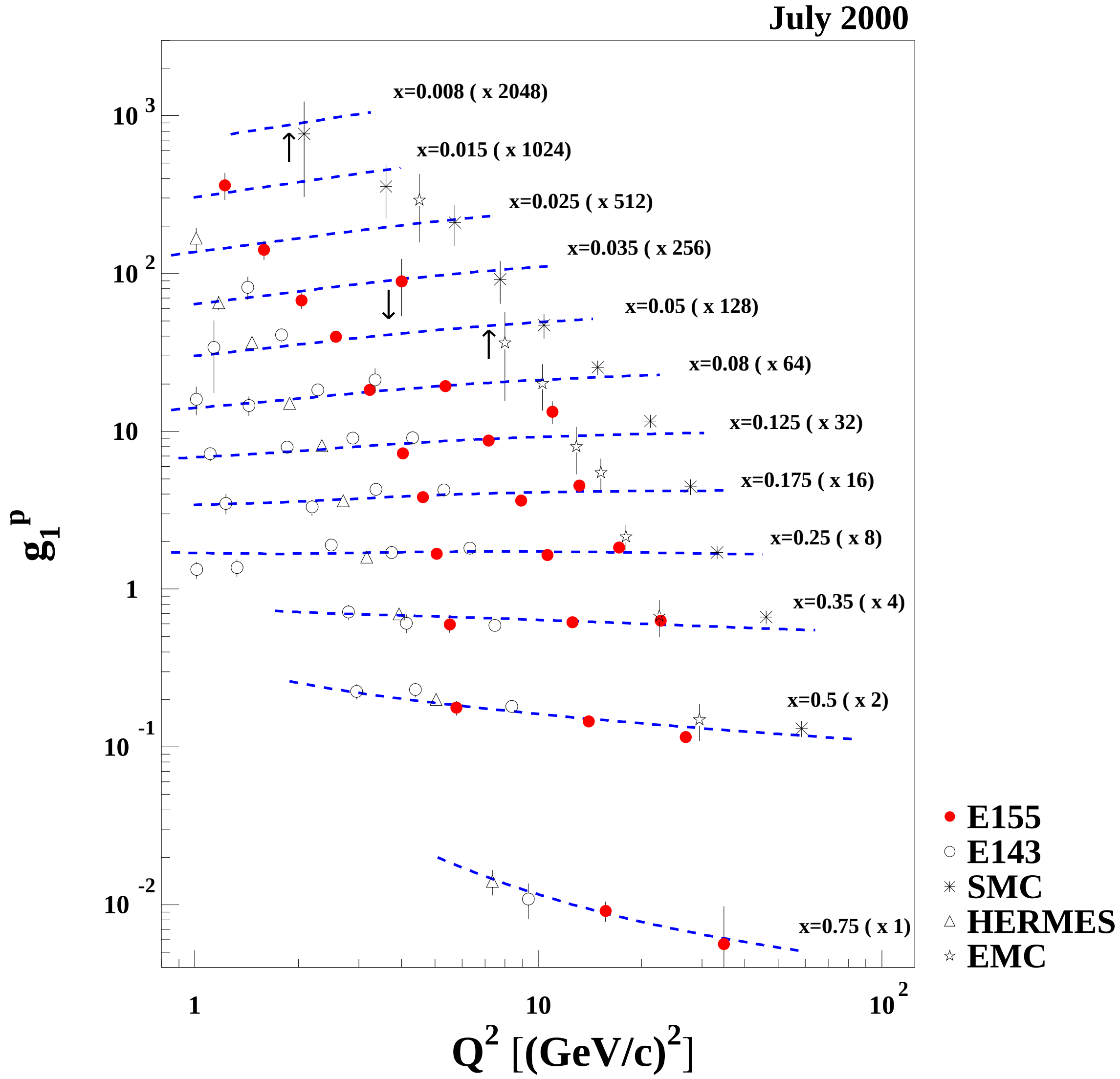

Figure 4.7: **E155 g_1 Proton vs. Q^2** Plot of world g_1 proton data against Q^2 for 12 different constant values of x. g_1 is multiplied by the given number at the right in order to separate each curve for easy viewing. The dashed-curves are the E155 global (phenomenological) fit.

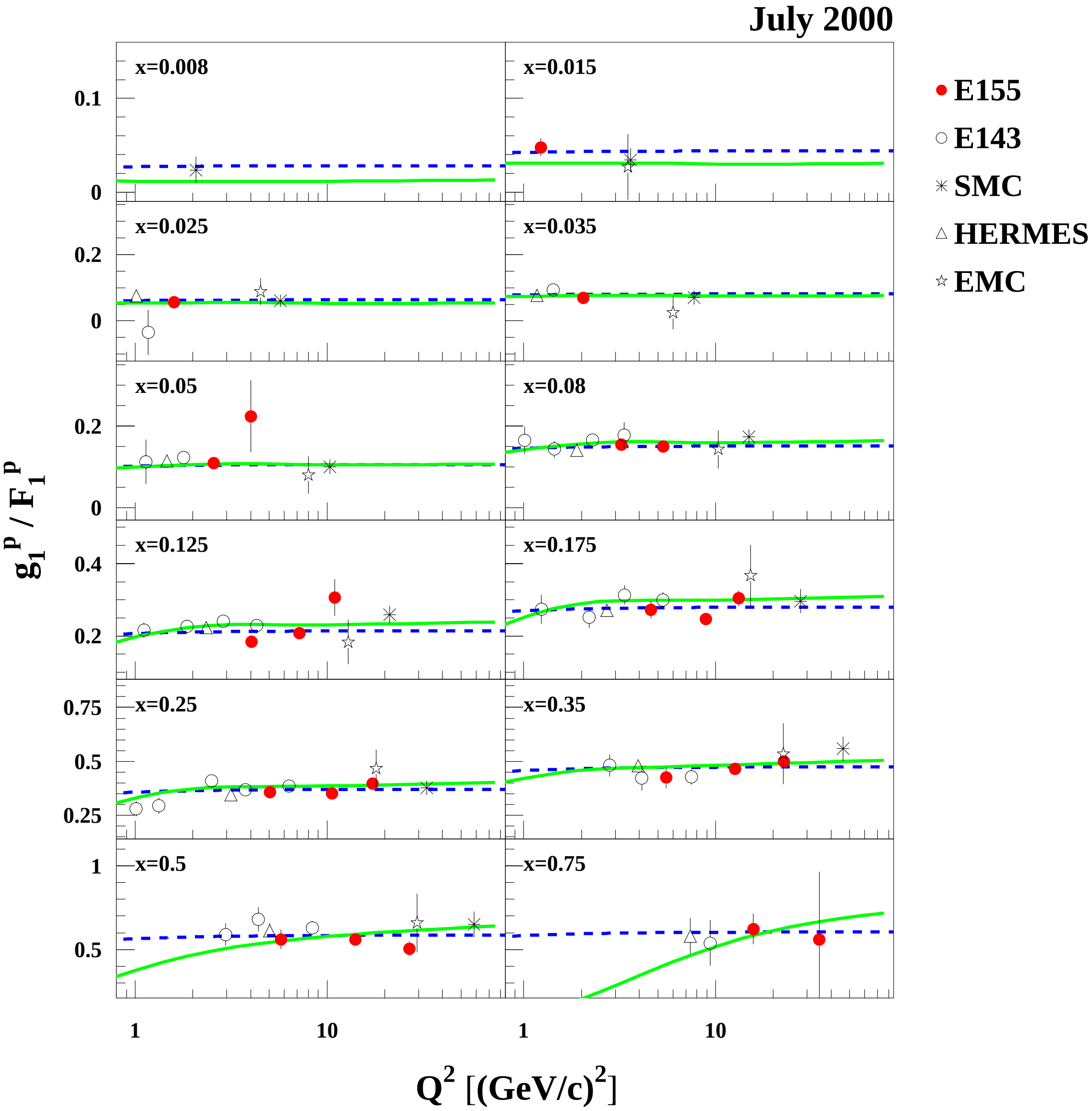

Figure 4.8: **E155 Q^2 Dependence of g_1/F_1 Proton** The dashed-curves are the E155 global (phenomenological) fit and the solid-curves are the E155 NLO fits.

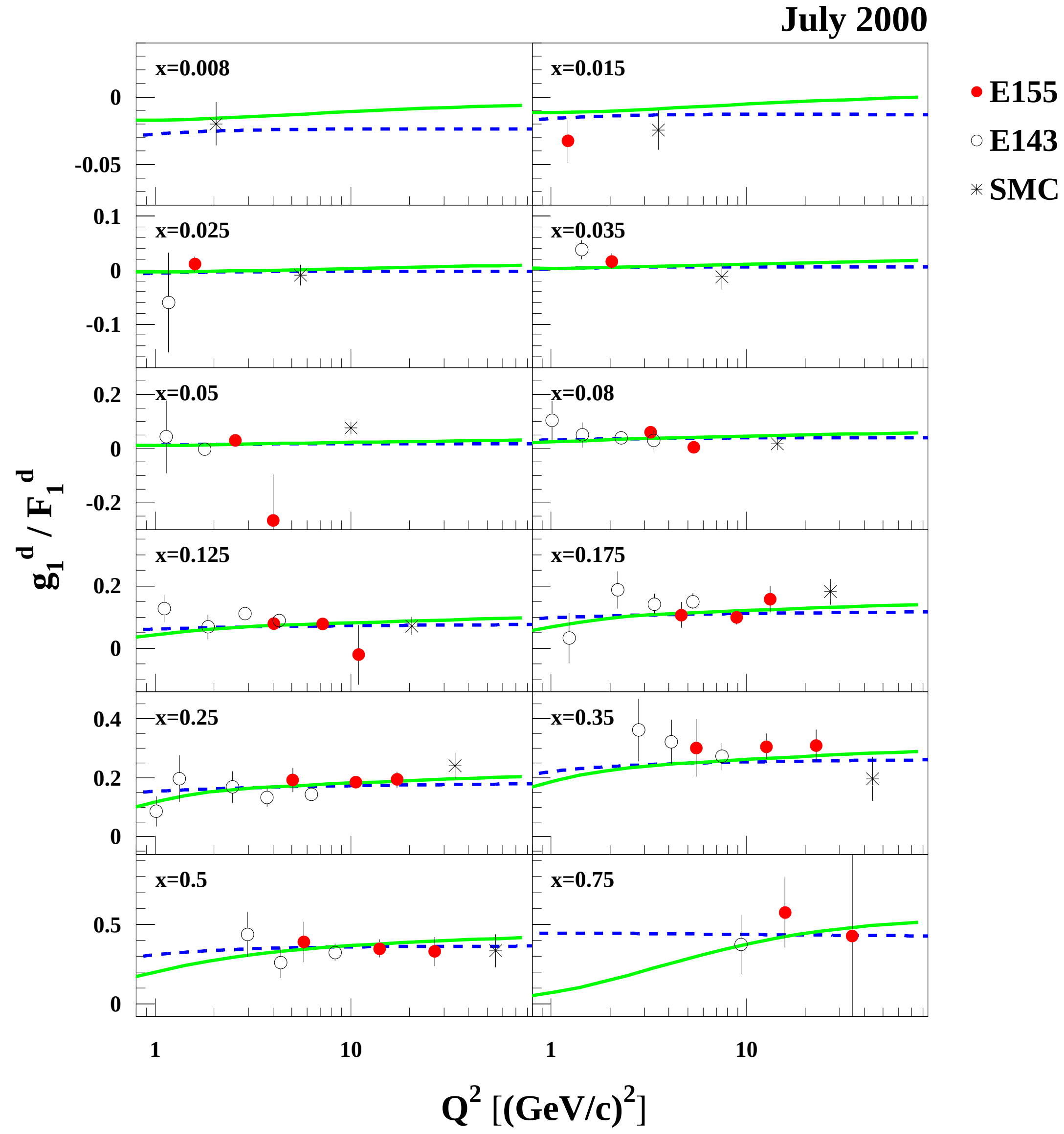

Figure 4.9: **E155 Q^2 Dependence of g_1/F_1 Deuteron** The dashed-curves are the E155 global (phenomenological) fit and the solid-curves are the E155 NLO fits.

at low and high x to extrapolate g_1 over kinematics outside the measured x-range.

4.4.1 Measured Range

Determination of the g_1 integral in the E155 measured x-range was computed numerically using

$$\Gamma_1(0.014, 0.90) \equiv \int_{0.014}^{0.90} g_1(x, Q_o^2)dx = \sum_i g_1(x_i, Q_o^2)dx_i \tag{4.8}$$

after averaging the data from the three spectrometers and shifting the data to a fixed $Q_o^2 = 5$ GeV^2. From the E155 g_1 proton and deuteron data, the student analysis [see chapter 3] results are

$$\int_{0.014}^{0.9} g_1^p(x)dx = 0.118 \pm 0.002 \pm 0.010 \tag{4.9}$$

$$\int_{0.014}^{0.9} g_1^d(x)dx = 0.044 \pm 0.003 \pm 0.003. \tag{4.10}$$

where the errors are, in order, statistical and systematic.

4.4.2 Low and High x Extrapolations

For E155, the contribution from $x < 0.014$ was determined using next-to-leading order perturbative quantum chromodynamic (NLO pQCD) fits [98] to the data, where polarized parton distributions are calculated at low Q^2 and then evolved to $Q^2 = 5$ GeV^2 using an evolution equation formalism, to extrapolate g_1 to $x = 0$. The $x > 0.9$ contribution was treated as negligible after fitting to high x g_1 data and an extrapolation of $x \longrightarrow 1$ revealed a small contribution within experimental errors [83].

Brief Description of NLO

The NLO pQCD procedure used for E155 is the same as used by E154 [99]. A functional form of the polarized parton distributions (valence quarks: Δu_V and Δd_V, sea quarks: $\Delta\bar{Q}$, gluons: ΔG) at low $Q_o^2 = 0.4$ GeV^2 are defined in terms of their unpolarized counterparts via

$$\Delta q_i(x, Q_o^2) = A_i x^{\alpha_i} q_i(x, Q_o^2) \tag{4.11}$$

where the fitting procedure adjusts the parameters A_i and α_i such that the polarized distributions are most consistent with the g_1 data. The unpolarized parton distributions are taken from the latest global analyses of unpolarized structure function data, the so-called GRV98, from reference [100]. A flavor symmetric sea, $\bar{u} = \bar{d} = s = \bar{s}$, is assumed such that the sea quark distribution is parameterized as $\Delta\bar{Q} = \frac{1}{2}(\Delta\bar{u} + \Delta\bar{d}) + \frac{1}{5}\Delta\bar{s}$.

The fitted results for equation (4.11) are then evolved to higher Q^2 using the so-called "Dokshitzer-Gribov-Lipatov-Altarelli-Parisi" (DGLAP) evolution equations, which hold x and Q^2 dependence information for the polarized parton distributions [101, 102]. From these NLO fitted distributions one can extract the moments of the polarized parton distributions, Δu_V, Δd_V, $\Delta\bar{Q}$, ΔG, the moments of g_1, Γ_1^p, Γ_1^d, Γ_1^n and Γ_1^{p-n}, and the net quark polarization, $\Delta\Sigma$.

Low x NLO Results

An extrapolation based on the published E154 NLO fits at $Q^2 = 5$ GeV^2 yields an estimate for the unmeasured low x region to be [99, 103]:

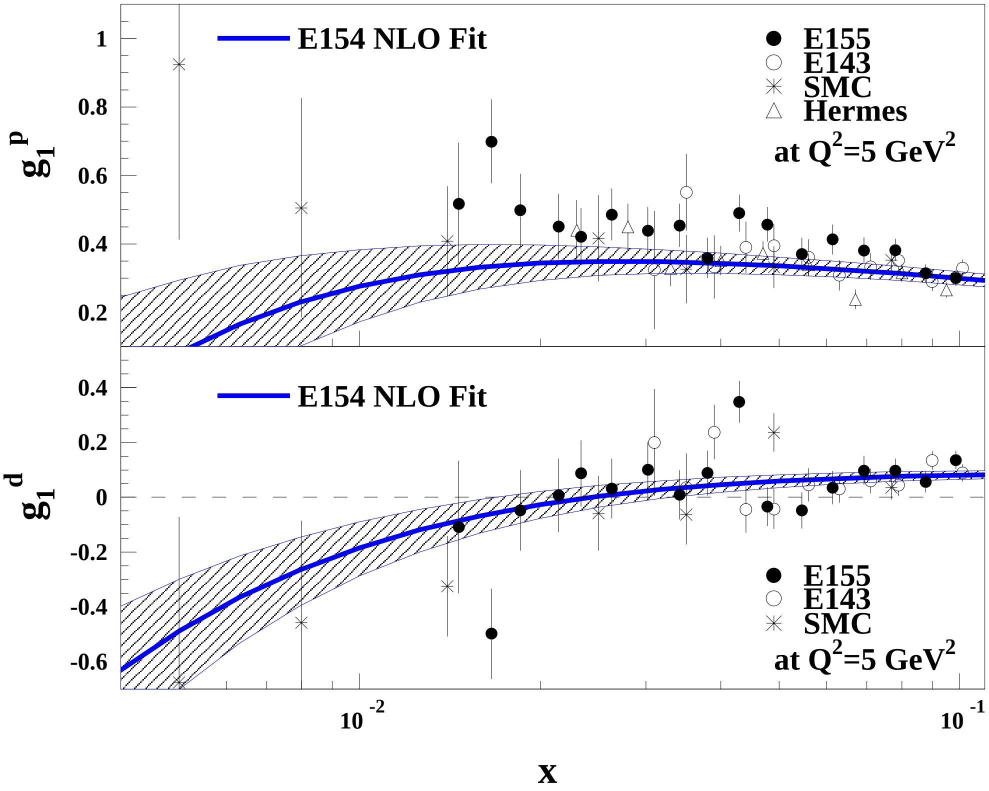

Figure 4.10: **E154 NLO Fits** The solid-curve (hatched-area) is the central value of (error on) the E154 NLO fits.

$$\int_0^{0.014} g_1^p(x)dx = -0.006 \pm 0.004 \pm 0.002 \pm 0.009, \tag{4.12}$$

$$\int_0^{0.014} g_1^d(x)dx = -0.014 \pm 0.004 \pm 0.002 \pm 0.005, \tag{4.13}$$

where the error is, in order, statistical, systematic and theoretical/evolution. The E154 NLO fits are plotted against a world data set in figure (4.10) [82]. E155 data were not used in these fits. An updated E155 NLO analysis that included the E155

E155 **SET**	**E155 measured** $\int_{0.014}^{0.9} g_1$	**E154 NLO low x** $\int_{0}^{0.014} g_1$	**measured + low x** $\int_{0}^{1} g_1$
p	$0.118 \pm 0.002 \pm 0.010$	$-0.006 \pm 0.004 \pm 0.002 \pm 0.009$	$0.112 \pm 0.004 \pm 0.014$
d	$0.044 \pm 0.004 \pm 0.003$	$-0.014 \pm 0.004 \pm 0.002 \pm 0.005$	$0.030 \pm 0.006 \pm 0.006$
n	$-0.024 \pm 0.005 \pm 0.011$	$-0.024 \pm 0.004 \pm 0.002 \pm 0.005$	$-0.048 \pm 0.006 \pm 0.012$
p-n	$0.142 \pm 0.006 \pm 0.014$	$0.018 \pm 0.006 \pm 0.003 \pm 0.010$	$0.160 \pm 0.008 \pm 0.017$

Table 4.3: **E155 Analysis Sum Rule Results** The integral of g_1 at fixed $Q^2 = 5$ GeV^2 in the E155 measured region as well as the low x extrapolation based on E154 NLO results. The error terms are, in order, statistical, systematic and theoretical/evolutional. The high x contribution is considered negligible.

data is described in the following section and results given in figure (4.11).

4.4.3 Total Integral

Combining the low x, high x and measured region contributions yields the total experimental integrals,

$$\int_0^1 g_1^p(x)dx = 0.112 \pm 0.004 \pm 0.010 \pm 0.009, \tag{4.14}$$

$$\int_0^1 g_1^d(x)dx = 0.030 \pm 0.006 \pm 0.004 \pm 0.005 \tag{4.15}$$

The E155 "measured+low/high x extrapolation" integral results are also presented in table (4.3). Determination of the integrals over the whole $0 < x < 1$ range based on E155 NLO fits [fits to world g_1 data including the latest E155 data are shown in figure (4.11)] are presented in table (4.8) near the end of this chapter. In this procedure, the central values were determined by minimizing the χ^2 between the fit and data, whereas the errors were determined by the spread of 600 fits to the data points scattered randomly about their central values [103]. This method gives

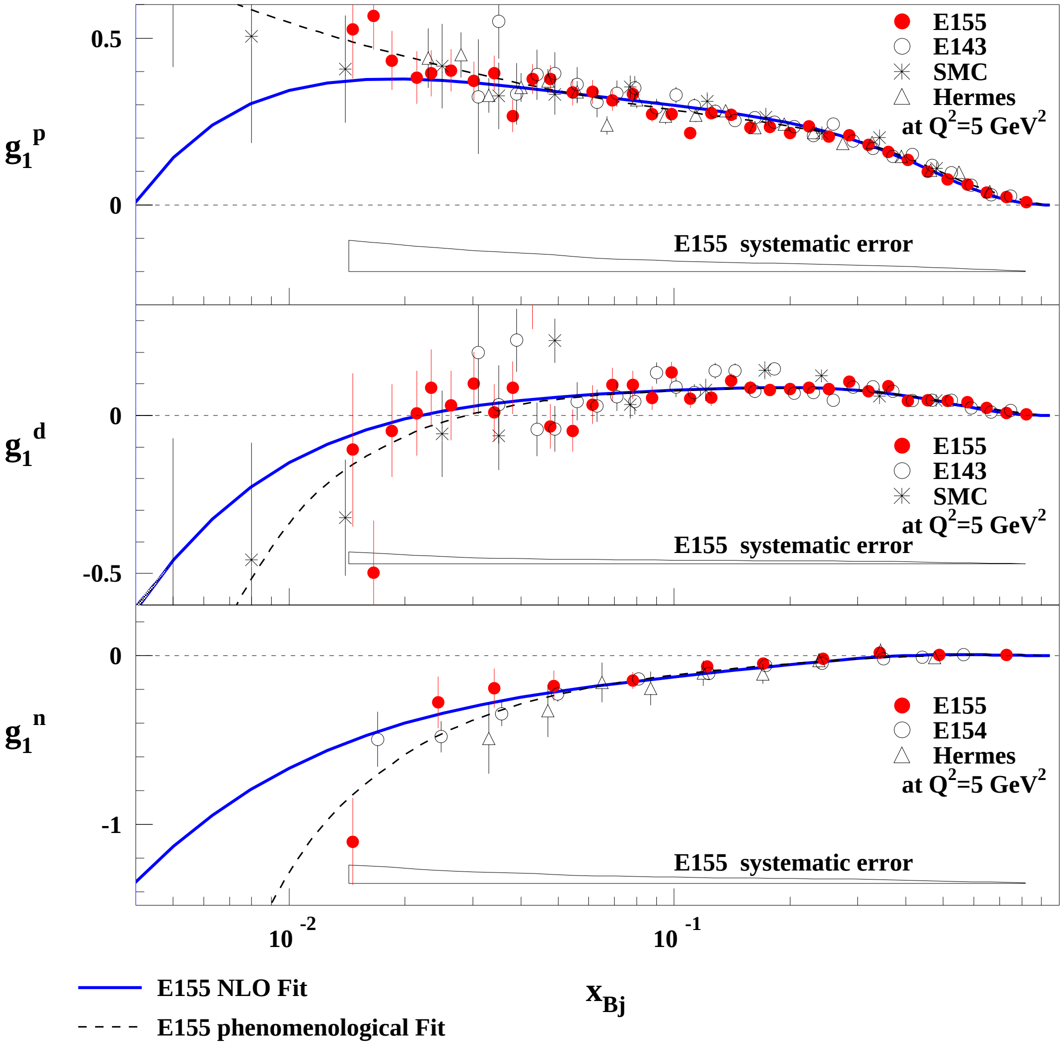

Figure 4.11: **E155 NLO and Empirical Fits** E155 fine-binned g_1 data evolved to $Q^2 = 5$ GeV^2. Also plotted are the E155 NLO and the E155 Global (phenomenological) fits to world data. Figure is taken directly from reference [89].

final results with lower statistical error than the values determined directly from the measured region plus low x extrapolations.

4.4.4 Independent Sum Rule Analysis

The motivation for extracting a function to describe g_1 for the neutron using E155 deuteron data alone and world proton data has to do with the nature of the targets involved in each experiment. The determination of the proton structure function is carried out by scattering polarized electrons off polarized protons in a suitable target material (ammonia, alcohols). For the neutron, the structure function is determined by either 1) scattering off a deuteron in ammonia, ^{6}LiD etc. and a subtraction procedure with proton information employed where correction factors involve the nuclear physics of the deuteron, or 2) scattering off ^{3}He with nuclear correction factors applied as well. These methods are employed since no free neutron targets exist. By using a fit to ^{6}LiD data alone, any nuclear effects due to our lithium deuteride target itself might be resolved.

In an independent sum rule analysis (ISRA), fits to pre-E155 world g_1/F_1 proton data and the measured g_1/F_1 deuteron data from E155 alone are used to extract a function to describe g_1 for the neutron with which various sum rules are tested. A sum rule analysis has been done with the E155 global fits to proton, neutron and deuteron as well.

ISRA Fits

The world proton data set consists of 158 g_1/F_1 data points from five experiments: CERN experiments EMC and SMC and SLAC experiments E80, E130 and E143, whereas the deuteron data consists of 71 g_1/F_1 data points from E155 alone. All the

parameter	g_1^p/F_1^p	g_1^d/F_1^d
a	1.275	1.411
b	——	——
c	-0.677	-0.758
α	0.806	1.445
β	-0.153	0.314
χ^2	123.1	83.3
d.f.	154	67

Table 4.4: **ISRA Fits**

data fit the constraints $x > 0.01$, $Q^2 > 1.0$ GeV^2 and missing mass $W^2 > 4.3$ GeV^2 to assure DIS events. Each of the data sets are fitted to the functional form:

$$\left(\frac{g_1}{F_1}\right)_{fit} = f(x, Q^2) = ax^{\alpha}(1 + bx + cx^2)(1 + \beta/Q^2), \tag{4.16}$$

where the fit results and errors are given in table (4.4) and appendix E. Notice the constant term (a) is outside the polynomial term, the same convention is used in the E143 long paper [29], different from the E155 global fit convention that used the functional form in equation (4.5).

Figures (4.12) thru (4.20) are the results of the ISRA with the E155 global fits plotted for comparison. Figures (4.12) and (4.13) show the g_1/F_1 fit results plotted with the entire data set in the top plot and the same data set coarse-binned in the bottom plot. Figure (4.14) shows the extracted g_1/F_1 neutron from the proton and deuteron parameterizations for g_1/F_1 from the ISRA using the equation

$$\left(\frac{g_1^n}{F_1^n}\right) \cdot F_1^n = 2\left(\frac{g_1^d}{F_1^d}\right)_{fit} \cdot F_1^d \Big/ \left(1 - \frac{3}{2} \cdot \omega_D\right) - \left(\frac{g_1^p}{F_1^p}\right)_{fit} \cdot F_1^p \tag{4.17}$$

and world fits to F_2 [104] and R [105] via equation (1.36), where the E155, E154 and

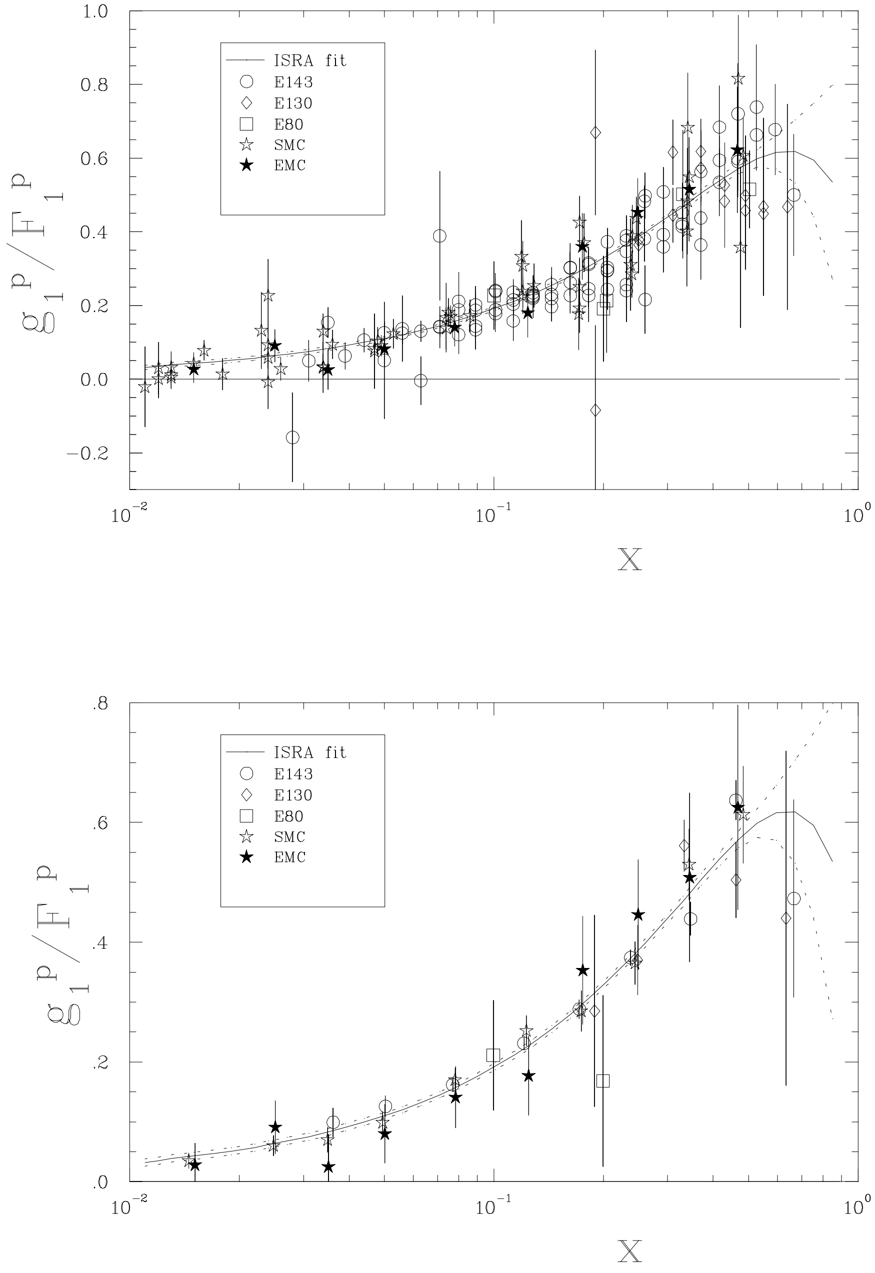

Figure 4.12: **ISRA g_1/F_1 Proton Fit Results** The fitted function for g_1/F_1 proton from table (4.4) plotted with the 158 point world proton data set on top, and the same data set coarse-binned via table (4.2) on the bottom. For clarity, the five data sets have been offset from the central x-bin value by -0.2, -0.1, 0, 0.1, 0.2 x for E143, E130, E80, SMC, EMC respectively. The dashed lines represent the error on the fits.

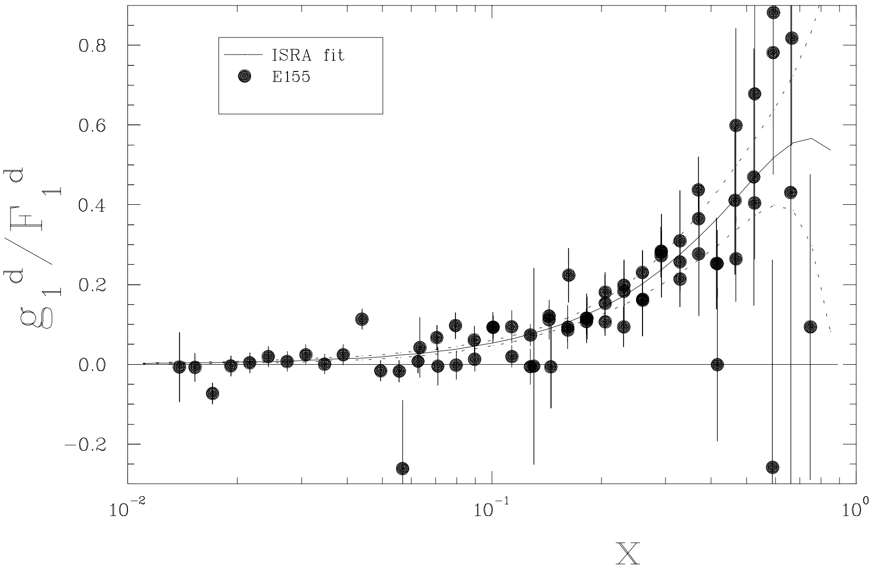

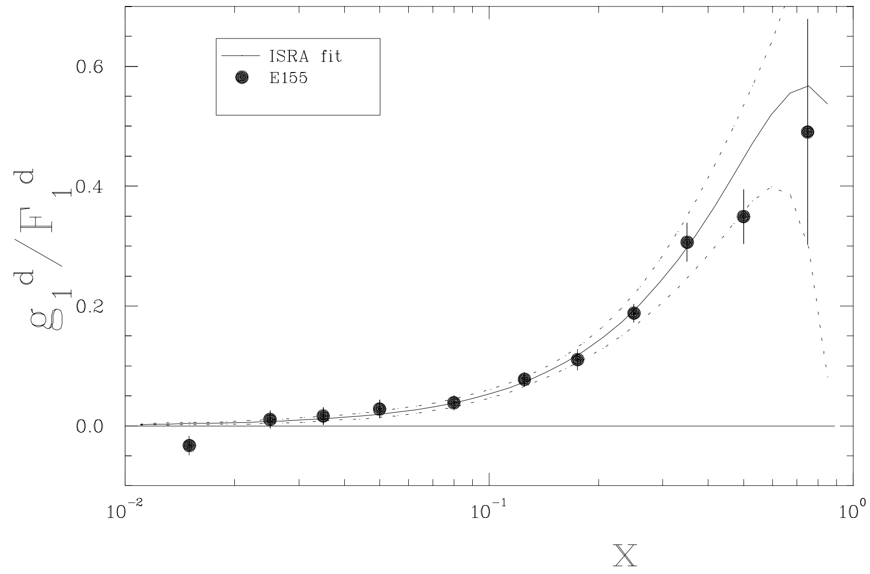

Figure 4.13: **ISRA g_1/F_1 Deuteron Fit Results** The fitted function for g_1/F_1 deuteron from table (4.4) plotted with the 71 point E155 deuteron data set on top, and the same data set coarse-binned via table (4.2) on the bottom. The dashed lines represent the error on the fits.

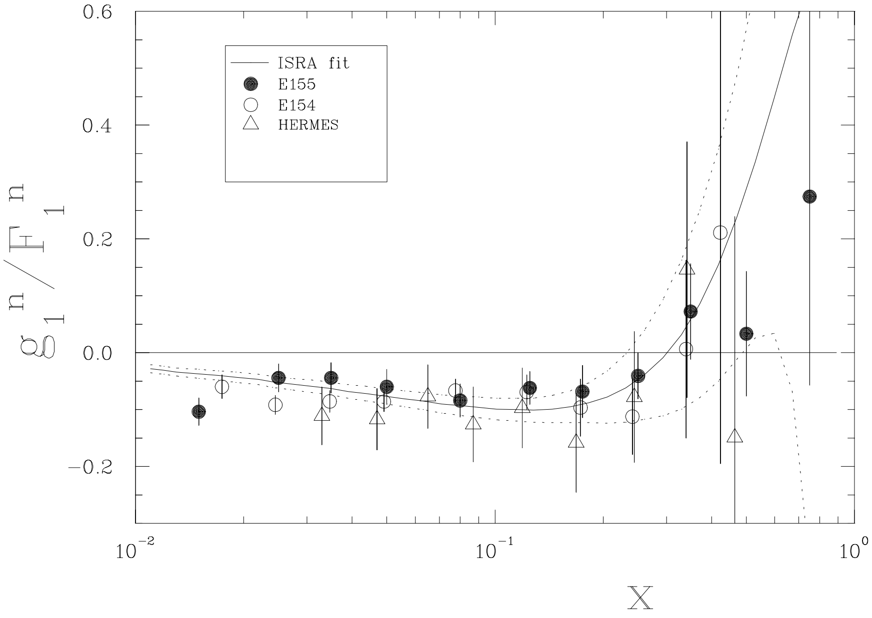

Figure 4.14: **ISRA g_1/F_1 Neutron Extraction** The parameterization of g_1/F_1 for neutron as extracted from the ISRA fits to proton and deuteron via equation (4.17). The neutron data from E155, E154 and Hermes are plotted only for comparison. The dashed lines represent the error on the fits.

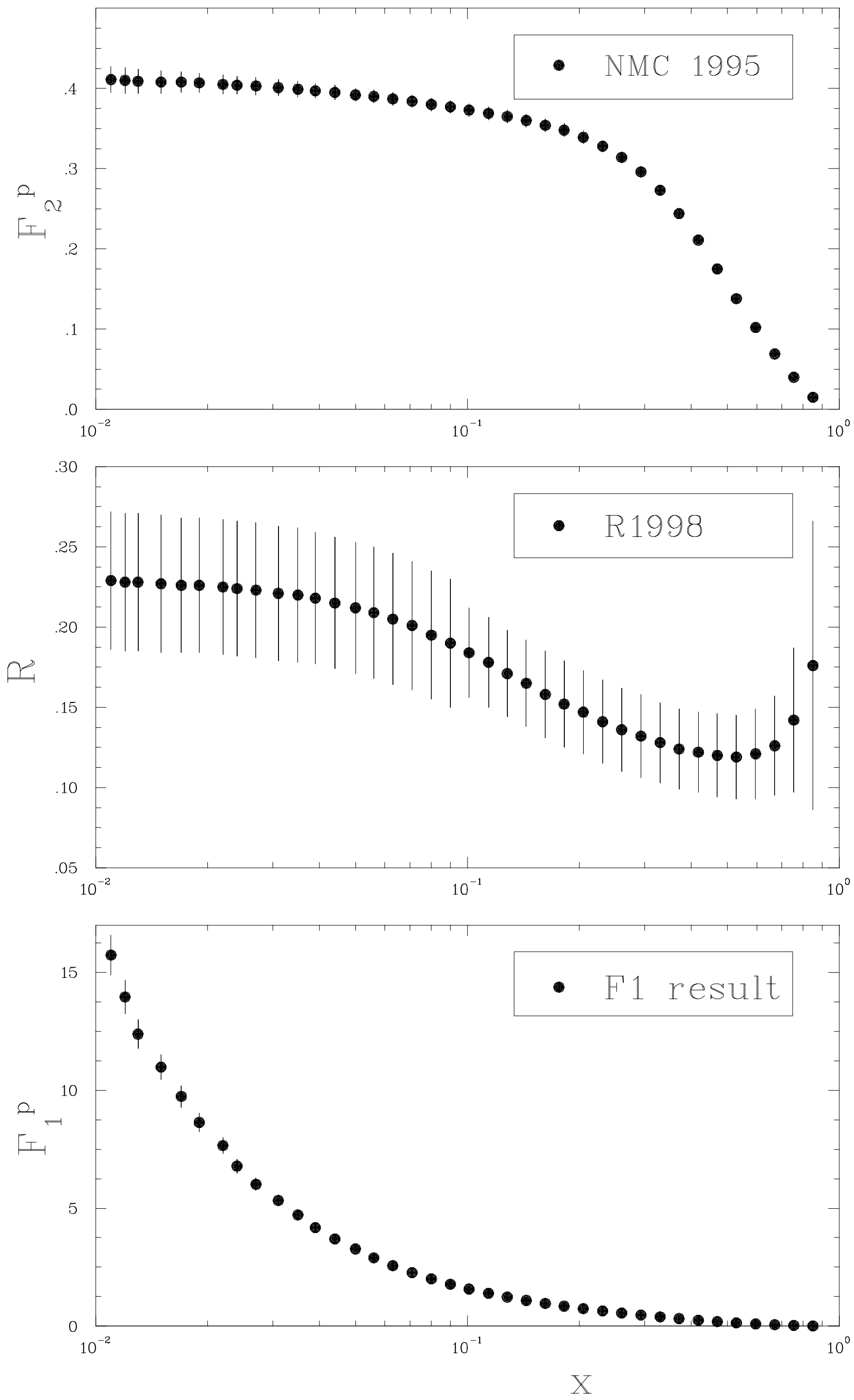

Figure 4.15: F_2**,** R **and** F_1 **Proton** The NMC F_2 and SLAC R parameterizations with the extracted F_1 as used in the ISRA evaluated at a common $Q_o^2 = 5$ GeV^2.

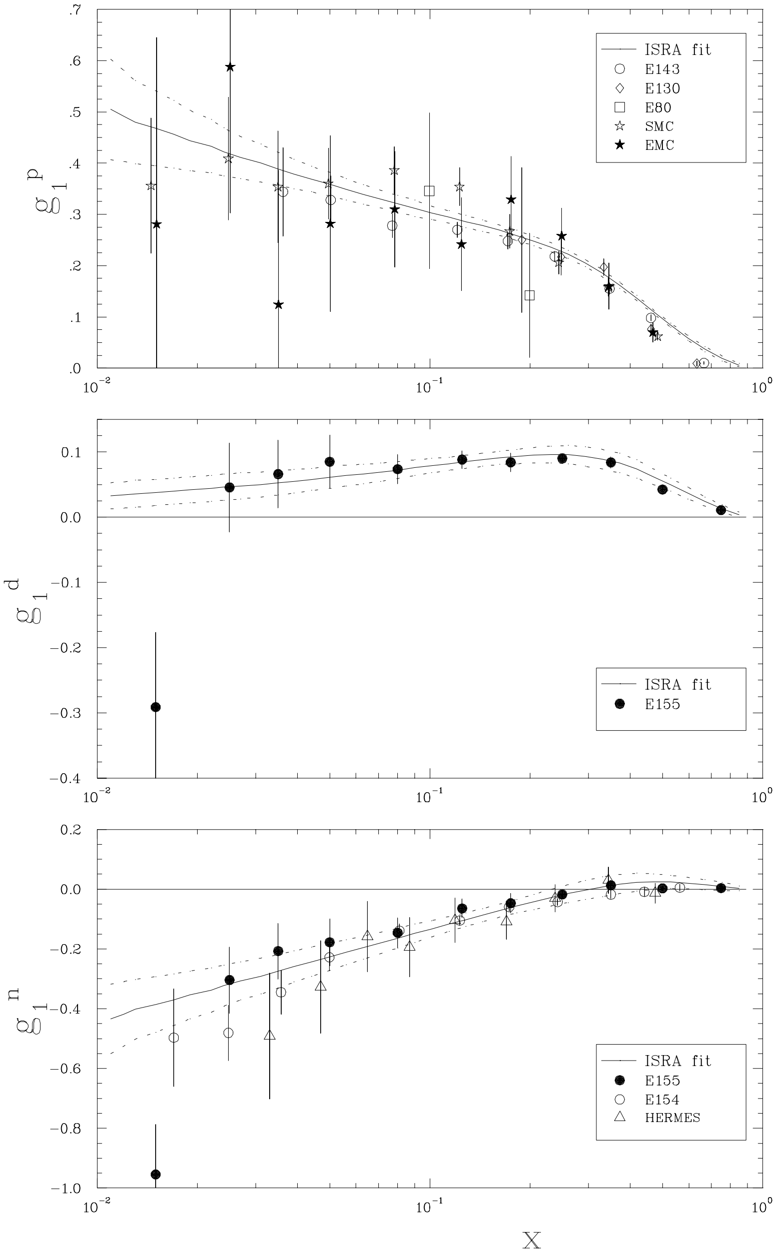

Figure 4.16: **ISRA g_1 Results** The extracted functions for g_1 from the g_1/F_1 fits in table (4.4) multiplied by F_1 (obtained from the F_2 and R parameterizations). *Top plot:* g_1 for proton plotted with coarse-binned ISRA g_1/F_1 proton data set multiplied by F_1. The five data sets are offset in x as in the bottom plot of figure (4.12). *Middle plot:* g_1 for deuteron plotted with coarse-binned E155 deuteron data set multiplied by F_1. *Bottom plot:* g_1 for neutron plotted with coarse-binned E155, E154, and Hermes neutron data for comparison. The dashed lines represent the error on the fits.

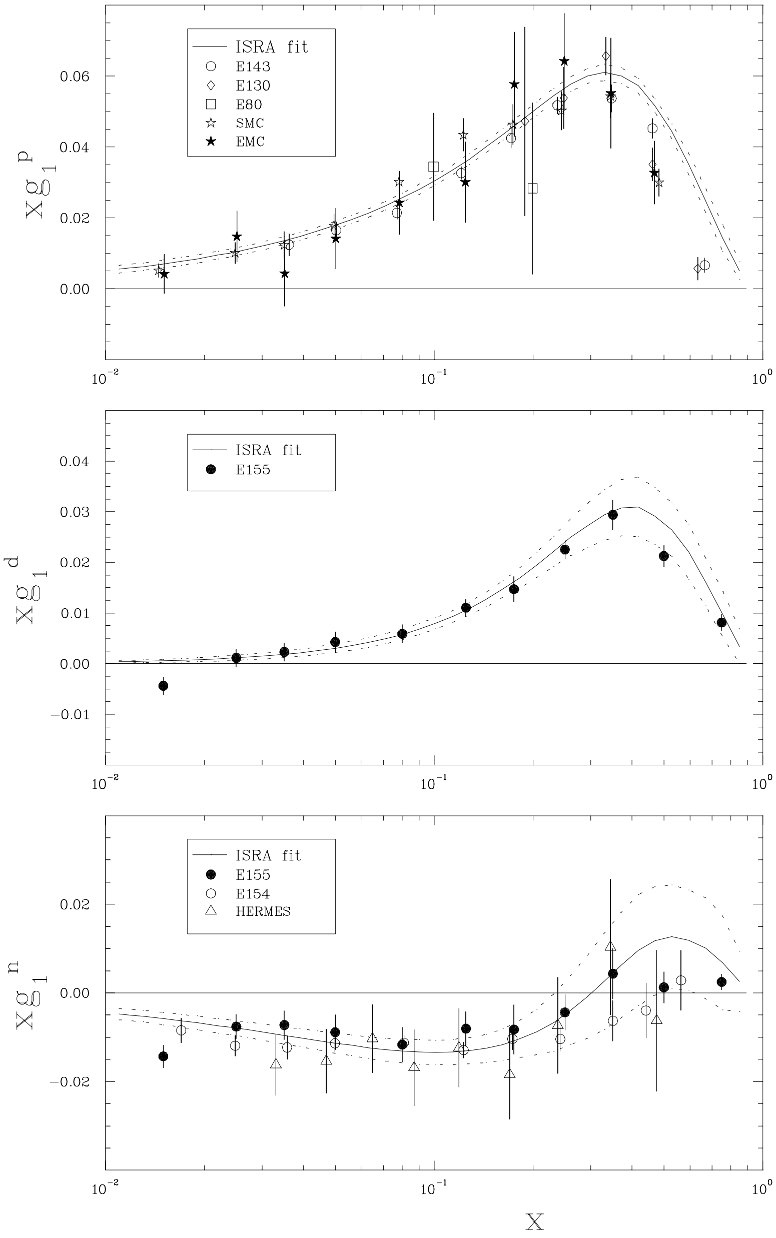

Figure 4.17: **ISRA xg_1 Results** Same as figure (4.16) except g_1 is multiplied by the central value of each x-bin.

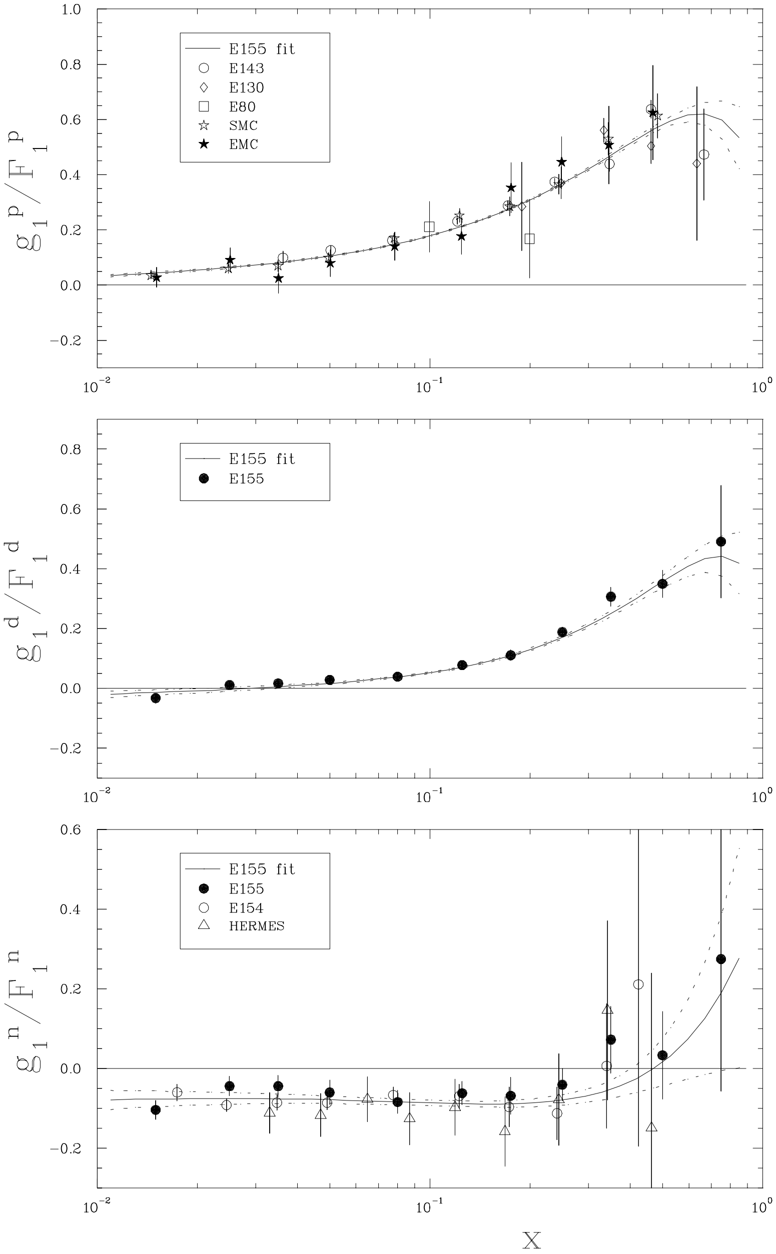

Figure 4.18: **E155 Global g_1/F_1 Fit Results** The E155 global fit results plotted against the same experiment data sets as in figures (4.12) thru (4.14) for direct comparison with the ISRA result.

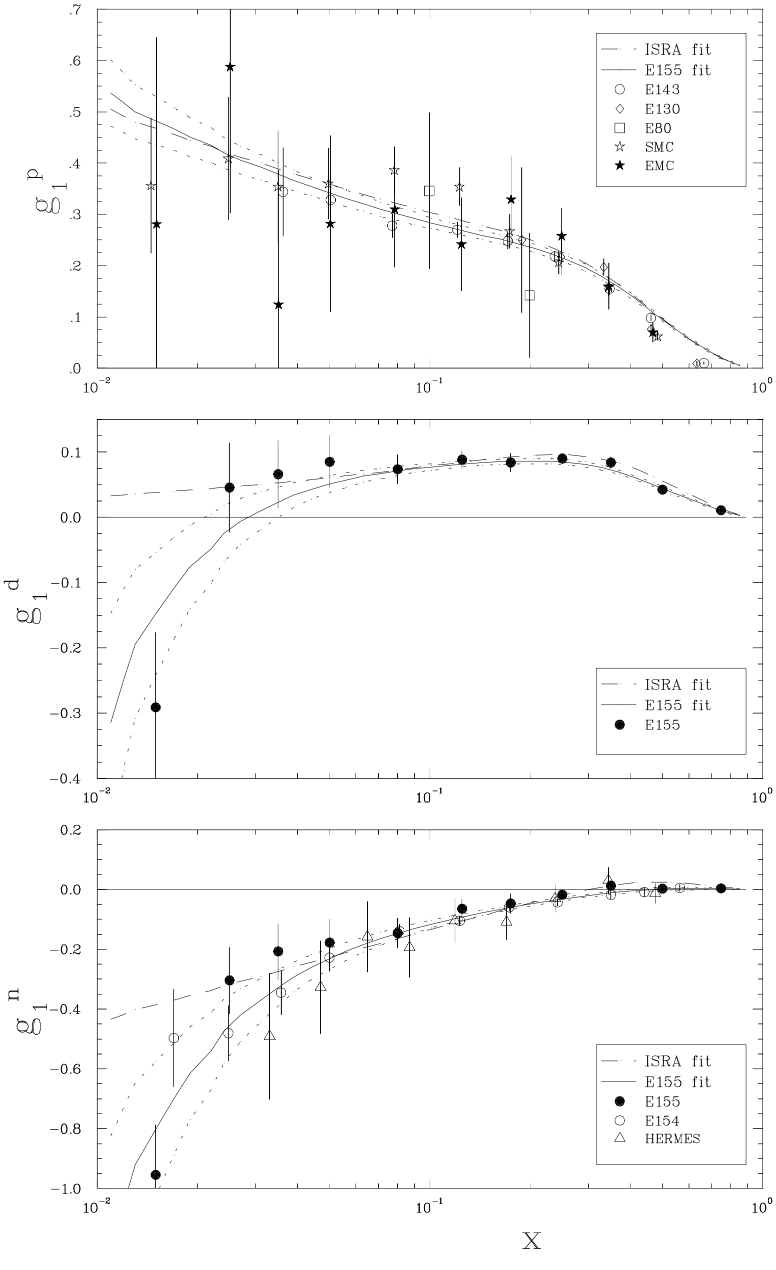

Figure 4.19: **E155 Global g_1 Results** The E155 global fit results (solid curve) plotted against the same experiment data sets as in figure (4.16) for direct comparison with the ISRA result (large-dashed curve). The small-dashed curves represent the error on the E155 global fits.

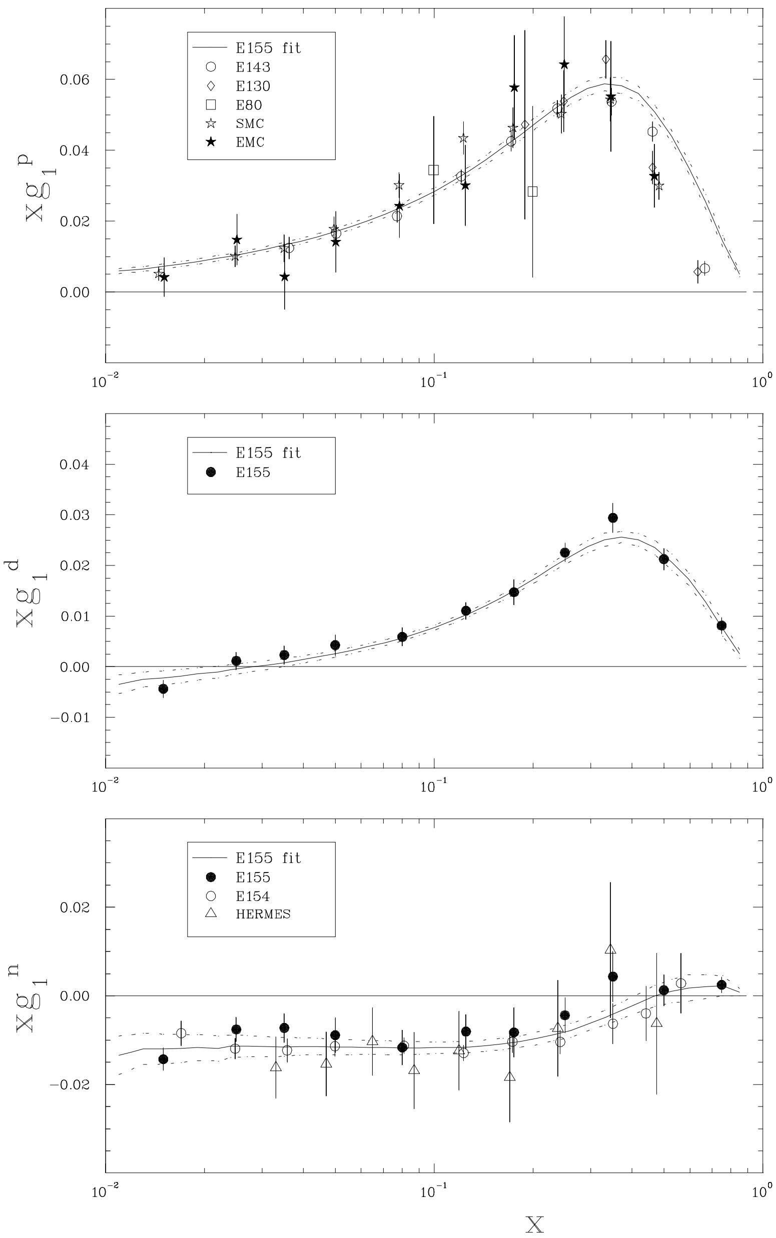

Figure 4.20: **E155 Global xg_1 Results** The E155 global fit results plotted against the same experiment data sets as in figure (4.16) for direct comparison with the ISRA result.

Hermes neutron data are plotted only for comparison. As used in the ISRA and E155 analysis, a fine-binned set of F_2, R and calculated F_1 are evaluated at a common $Q^2 = 5$ GeV^2 and plotted against $\log(x)$ in figure (4.15).

Figure (4.16) shows g_1 evaluated from the ISRA g_1/F_1 parameterizations. Notice that g_1 for deuteron and neutron follows the E155 collaboration's deuteron and neutron results (solid black circles) rather well except for the lowest coarse-bin at low x. This is in contrast to the E155 global fits which follow the low x point trend downward as shown in figure (4.19). Note that the E155 coarse-binned data was evolved using the E155 global fits, hence causing the low x point to shift lower in value.

ISRA Integrals

The ISRA g_1/F_1 fits to proton and deuteron data were used to obtain first moments of g_1, Γ_1^p, Γ_1^d, Γ_1^p and Γ_1^{p-n} in the effort to test the Ellis-Jaffe and Bjorken sum rules and to extract the quark contributions to the nucleon spin.

ISRA Measured Region

The measured region ($0.014 < x < 0.9$) integrals were evaluated by numerically integrating the ISRA g_1/F_1 proton and deuteron parameterizations along with F_1 and R via equation (E.11), the results of which are presented in table (4.6). The neutron integral was calculated using equation (4.7) while proton-neutron (p-n) from simple subtraction. Similarly, "E155" measured region integrals were obtained from the E155 global fit parameterizations for proton, deuteron and neutron for comparison and are presented in table (4.7).

ISRA **SET**	**Regge** $\alpha = 0$	**Regge** $\alpha = -0.5$	**Log Form** $g_1 = \beta\ ln(\frac{1}{x})$	**ISRA** **Fit**	**Average**
p	0.005	0.001	0.009	0.008	0.006 ± 0.007
d	0.001	0.000	0.002	0.001	0.001 ± 0.002
n	-0.003	-0.001	-0.005	-0.006	-0.004 ± 0.007
p-n	0.008	0.002	0.014	0.014	0.010 ± 0.010

Table 4.5: **ISRA Low x Extrapolations** Estimates of $\int_0^{0.014} g_1 dx$ at $Q^2 = 5$ GeV^2 using several models. The 2nd and 3rd columns fit g_1 data with $x \leq 0.1$ evolved to common $Q^2 = 5$ GeV^2 using the Regge form $g_1 = \beta x^{-\alpha}$ for α equal 0 or -0.5. The 4th column fits g_1 to the form $g_1 = \beta \ln(1/x)$. The 5th column uses the ISRA fit II from table (4.4). The last column gives the unweighted average of the four hypotheses with an error determined from the spread of the different methods. The n and $p - n$ results are extracted from the p and d fit results.

ISRA Low and High x Region

Due to the uncertain nature of $g_1(x)$ as $x \longrightarrow 0$, the ISRA obtained low x contributions to the integrals by taking the average of several more traditional methods than NLO. One such method is based on Regge trajectory-type behavior, where $g_1(x) \approx \beta x^{-\alpha}$ for $x \longrightarrow 0$ and α is the intercept of the a_1 Regge trajectory [29, 106]. The value of α is typically assumed to be in the range $-0.5 \geq \alpha \geq 0$. The ISRA performed fits to g_1 proton and deuteron data for $x \leq 0.10$ g_1 at constant $Q^2 = 5$ GeV^2 using the Regge form for $\alpha = 0$ (flat Regge extrapolation) and $\alpha = -0.5$. Other functional forms such as $g_1 \approx \ln(1/x)$ [106, 107] were fitted to small x data for g_1 as well and are summarized in table (4.5). No NLO fitting was done in the ISRA.

After fitting g_1 data for $x > 0.5$ and $Q^2 = 5$ GeV^2 to the functional form $g_1 = \beta(1-x)^3$ [108] and integrating the fit for $(0.9 < x < 1)$, the high x extrapolation was found to be small and treated as negligible.

ISRA SET	**fitted** $\int_{0.014}^{0.9} g_1$	**high x** $\int_{0.9}^{1} g_1$	**low x** $\int_{0}^{0.014} g_1$	**total** $\int_{0}^{1} g_1$
p	$0.125 \pm 0.005 \pm 0.010$	0	0.006 ± 0.007	$0.131 \pm 0.005 \pm 0.012$
d	$0.048 \pm 0.006 \pm 0.003$	0	0.001 ± 0.002	$0.049 \pm 0.006 \pm 0.004$
n	$-0.021 \pm 0.013 \pm 0.011$	0	-0.004 ± 0.007	$-0.025 \pm 0.013 \pm 0.013$
p-n	$0.146 \pm 0.014 \pm 0.011$	0	0.010 ± 0.010	$0.156 \pm 0.014 \pm 0.015$

Table 4.6: **ISRA Results** The integral of g_1 in the fitted region as well as high and low x extrapolations at fixed $Q^2 = 5$ GeV^2. The fitted region values for p and d are obtained by integrating parameterizations of g_1/F_1, F_2 and R using the form $F_1 \cdot \left(\frac{g_1}{F_1}\right)_{fit}$ and equation (1.36).

E155 SET	**global fit** $\int_{0.014}^{0.9} g_1$
p	$0.120 \pm 0.004 \pm 0.010$
d	$0.040 \pm 0.002 \pm 0.003$
n	$-0.034 \pm 0.005 \pm 0.011$
p-n	$0.154 \pm 0.007 \pm 0.011$

Table 4.7: **E155 Global Fit Integrals** The integral of g_1 in the E155 measured region using the E155 global fits at fixed $Q^2 = 5$ GeV^2 and same method as described in table (4.6). The n and $n - p$ results are extracted from the p and d fit results.

	E155$_{NLO}$ $\int_0^1 g_1$	**E155**$_{exp}$ $\int_0^1 g_1$	**ISRA**$_{exp}$ $\int_0^1 g_1$	**theory** $\int_0^1 g_1$
p	0.118 ± 0.008	0.112 ± 0.015	0.131 ± 0.013	0.163 ± 0.004
d	0.028 ± 0.006	0.030 ± 0.008	0.049 ± 0.007	0.067 ± 0.006
n	-0.058 ± 0.009	-0.048 ± 0.013	-0.025 ± 0.018	-0.019 ± 0.004
p-n	0.176 ± 0.008	0.160 ± 0.019	0.156 ± 0.021	0.182 ± 0.005

Table 4.8: **Sum Rule Results Comparison** The first column contains the E155 NLO fit results. The second column contains the final E155 integrals as determined from the measured integral and NLO low x extrapolations. The third column contains the ISRA total integral results. The last column contains the calculated integrals using pQCD to third order (first three rows are Ellis-Jaffe, the last row Bjorken sum rule). All numbers are for fixed $Q^2 = 5$ GeV^2 and have their statistical and systematic errors combined in quadrature.

Moments and Quark Polarization

The total ISRA$_{exp}$ integrals were obtained by combining the low x, measured and high x region contributions and are presented in table (4.6). The E155 experimental results from table (4.3) and the E155 NLO results from table (4.10) are presented with the ISRA moments in table (4.8) for comparison. Moments from all three analyses are somewhat consistent within their errors; however, note that Γ_1^d from E155$_{NLO}$ (E155$_{exp}$) is greater than 3σ (2σ) away from the ISRA value. The large difference is mostly due to the treatment of the unmeasured low x region.

The theoretical Ellis-Jaffe values for the first moments of g_1 are clearly larger than the measured ones. In table (4.8) one can see that the measured integrals for proton, deuteron and neutron are, in order, 5σ to 2σ, 7σ to 2σ and 4σ to 1σ away from the theoretical sum rule values, with the E155$_{NLO}$ (ISRA$_{exp}$) results typically the furthest away (nearest). However, all moment analyses for proton-neutron are within 1σ of the theoretical Bjorken value.

The quark spin contributions $\Delta\Sigma(Q^2)$, Δu, Δd and Δs can be computed readily

	proton	**deuteron**	**neutron**
Δu	0.82 ± 0.04	0.73 ± 0.03	0.82 ± 0.06
Δd	-0.49 ± 0.04	-0.52 ± 0.03	-0.54 ± 0.06
Δs	-0.13 ± 0.04	-0.19 ± 0.02	-0.16 ± 0.05
$\Delta\Sigma$	0.26 ± 0.13	0.39 ± 0.08	0.26 ± 0.18

Table 4.9: **ISRA Quark Helicities** Summary of quark helicity components calculated from ISRA Γ_1 of table (4.8), $a_3 = F+D$ and $a_8 = 3F-D$ where $\Delta\Sigma = \Delta\Sigma(Q^2)$.

Δu_V	0.71 ± 0.02 ± 0.04
Δd_V	-0.45 ± 0.03 ± 0.03
$\Delta\overline{Q}$	-0.01 ± 0.01 ± 0.02
ΔG	1.62 ± 0.78 ± 1.13
$\Delta\Sigma$	0.229 ±0.041 ±0.057
Γ_1^p	0.118 ±0.004 ±0.007
Γ_1^n	-0.058 ±0.005 ±0.008
Γ_1^d	0.028 ±0.004 ±0.005
Γ_1^{p-n}	0.176 ±0.003 ±0.007

Table 4.10: **E155 NLO Results** Moments of the polarized parton distributions, net quark polarization and g_1 structure function at $Q^2 = 5$ GeV^2 determined by way of the NLO pQCD fitting procedure.

from the sum rule results in terms of Γ_1, a_3 and a_8 via equations (1.84) thru (1.86) with the method outlined in section (1.5.1). The ISRA results are presented in table (4.9). The NLO quark helicities are obtained via the NLO method as outlined in section (4.4.2) and are presented in table (4.10). Both analyses confirm the small quark contribution to the nucleon spin. E155 NLO indicates a large positive (small negative) contribution from gluons (the sea).

Comment on Error

Typically fits to data are done considering statistical errors only. A better method could be to add the statistical and systematic error in quadrature and do fits to data weighted on the combined error. Including systematic effects could more accurately represent the uncertainty in the experimental data.

The ISRA followed the traditional approach; the fits were weighted by statistical errors only. The integrals were calculated from the final fits with the statistical error determined from the fit error on the g_1/F_1, F_2 and R parameterizations. The ISRA moment systematic errors were taken directly from the published E155 measured region error [16] for the deuteron and a combination of the published measured proton integral systematic errors that make up the fitted world proton data. These errors were then propagated through to the neutron and proton-neutron moment results.

Synopsis

Depending on the analysis procedure used, one obtains significant differences in the extracted g_1 integrals. A large portion of the integral value over $0 \leq x \leq 1$ comes from the low x unmeasured region; hence, the total integrals depend highly on assumptions of low x behavior and their extrapolations. The NLO fitting formalism yields large negative contributions to all three integrals (proton, deuteron and neutron) as noted in table (4.3), while more traditional Regge-type extrapolations tend to contribute less and are positive (negative) for the proton and E155 deuteron (neutron) as indicated in table (4.5). A glance at the g_1 plots in figure (4.10) indicate that the NLO fits to proton do not follow the SMC data's upward trend as x approaches zero. However, NLO does appear to follow the downward trend in the g_1 deuteron and neutron data rather well. Since the E155 NLO parameterization of g_1 deuteron fit was obtained from global NLO fits to proton, neutron and deuteron data, the downward trend may be biased by the high precision g_1 neutron data which sharply drops at low x. The E155 global phenomenological fits appear to fit the low x well for all three nuclear

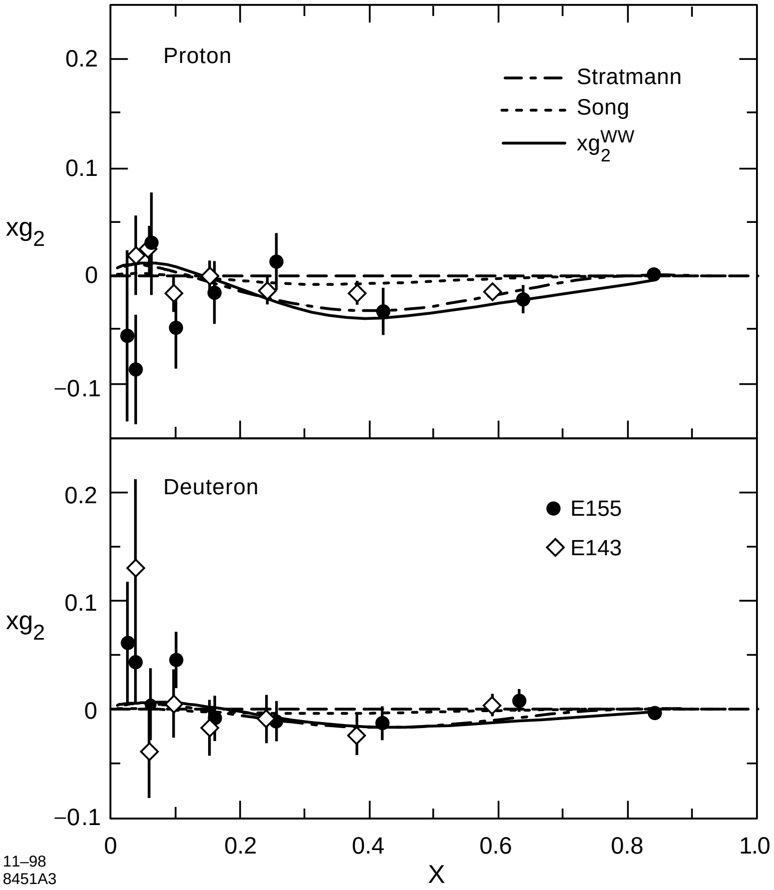

Figure 4.21: **E155/E143 xg_2 Results** The spectrometer combined data for xg_2 with statistical errors only (systematic errors negligible). MOD Bag Model calculation by Stratmann [109], Center-of-Mass (CM) Bag Model calculation by Song [110] and Twist-2 g_2^{WW} calculation are also shown. From reference [40].

species since they empirically fit the actual world data.

4.5 The g_2 Structure Function

The absolute value of A_2 was extracted from the transverse scattering data and found to be significantly smaller than the $\sqrt{R}$ positivity limit over the measured $0.2 < x < 0.8$ range [40]. The extracted g_2 for proton and deuteron was found to be consistent with the twist-2 Wandzura-Wilczek calculation [see section (1.6)]. Figure (4.21) shows the xg_2 results for both E143 and E155. Since g_2 measurements were performed at different kinematics than g_1 [48.4 GeV for $A_{||}$ (g_1), 38.8 GeV for $A_{\perp}$ (g_2)] and the large statistical errors compared to the g_1 measurement, the g_2 result served as a confirmation to use the g_2^{WW} approximation in equation (4.1) to extract g_1 from the $A_{||}$ data. E155 evaluated the integrals over g_2 for the measured range and found

$$\int_{0.02}^{0.8} g_2^p(x)dx = -0.022 \pm 0.071, \tag{4.18}$$

$$\int_{0.02}^{0.8} g_2^d(x)dx = 0.023 \pm 0.044, \tag{4.19}$$

both consistent with zero and thus confirming the Burkhardt-Cottingham sum rule [see section(1.7.3)] within the experimental error. The experiment also found the twist-3 matrix elements d_2 for the proton and deuteron to be consistent with zero.

4.6 Conclusions

The accuracy of spin structure data have much improved over the past few years with E155 contributing the most precise measurement of g_1 to date. Although not as precise, E155 measurements of g_2 show consistency with the g_2^{WW} prediction. The violation of the Ellis-Jaffe sum rule is confirmed by the small values for the first moments of g_1, while the Bjorken prediction for the difference of proton and neutron moments are valid within the experimental error. The combination of E155 and ISRA constrains the net quark polarization $\Delta\Sigma$ between 1/4 to 2/5, verifying the small quark contribution to the nucleon spin as observed by previous experiments. This means that the overall spin of the nucleon could be mostly made up by a positive contribution from the gluons in ΔG. Moreover, the E155 NLO results indicate that within the quark contribution, there is a non-zero (possibly negative) quark sea $\Delta\bar{Q}$. Only after establishing well the gluon and sea contributions can one quantify the system orbital angular momentum contribution, L_z, to the total spin of the nucleon.

Appendix A

The E155 Collaboration

The E155 collaboration consisted of over 90 scientists and students from around the world from over twenty educational institutions and laboratories. There were six graduate students from American University, College of William & Mary, Old Dominion University, University of Wisconsin and University of Virginia who participated in E155 as their thesis experiment (names listed in italics). The following lists the members of the E155 collaboration, along with the member institutions.

Collaboration Members

P. Anthony, R. Arnold, T. Averett, H. Band, C. Berisso, H. Borel, P. Bosted
S. Bültmann, M. Buenerd, T. Chupp, S. Churchwell, G.R. Court, D. Crabb
D. Day, P. Decowski, P. DePietro, R. Erbacher, R. Erickson, A. Feltham
H. Fonvieille, E. Frlez, R. Gearhart, V. Ghazikhanian, J. Gomez, K. Griffioen
C. Harris, M.A. Houlden, E. W. Hughes, C. Hyde-Wright, G. Igo, S. Incerti
J. Jensen, J. Johnson, *P. King*, Yu. G. Kolomensky, S. Kuhn, R. Lindgren
R. Lombard-Nelsen, J. Marroncle, W. Meyer, J. McCarthy, *P. McKee*
G. Mitchell, J. Mitchell, M. Olson, S. Penttila, G. Peterson, G. G. Petratos

R. Pitthan, D. Pocanic, R. Prepost, C. Prescott, L. M. Quin, B. Raue
D. Reyna, L.S. Rochester, S. Rock, O. Rondon-Aramayo, F. Sabatie
S. St. Lorant, I. Sick, L. Sorrell, T. Smith, F. Staley, L. M. Stuart, Z. Szalata
Y. Terrien, L. Todor, *A. Tobias*, *T. Toole*, S. Trentalange, D. Walz
R. Welsh, *F.R. Wesselmann*, T. Wright, C. Young, B. Youngman, M. Zeier
H. Zhu, B. Zihlmann

American University
Universität Basel
University Blaise Pascal
Ruhr-Universität Bochum
California Inst. of Technology
University of California–Los Angeles
PNC Saclay
Florida International University
Kent State University
University of Liverpool
LANL
University of Massachusetts
University of Michigan
Old Dominion University
Smith College
SLAC
Stanford University
TJNAF
University of Virginia
College of William and Mary
University of Wisconsin

Appendix B

Polarized Target Specifics

B.1 Liverpool NMR Simulation Study

The effects observed on a series-tune NMR system which violates the constant current conditions inherent in the design is presented for the tune frequency of 213.080MHz. The Liverpool NMR simulation package was used to calculate the relevant circuit parameters [77]. The package is a collection of MathCAD 6+ *.mcd files used to simulate the LCR Q-meter circuit used in our polarized target system. Ncc6back.mcd was used to calculate all the numbers in tables (B.2) thru (B.4).

The typical values for the parameters R_1 (R1 resistor), R_{cc} (constant current resistor), $\mathrm{r}_{\mathrm{coil}}$ (RF resistance of the sampling coil), $\mathrm{r}_{\mathrm{damp}}$ (damping resistor) and L (coil inductance) are listed in table (B.1) and were the same for all the calculations presented in this note. Equation (B.1) defines the true resonant frequency of the circuit.

$$f_{true} = \frac{1}{2\pi\sqrt{LC}} \tag{B.1}$$

parameter	value
R_1	50Ω
R_{cc}	619Ω
r_{coil}	0.35Ω
r_{damp}	10Ω
L	3×10^{-8}H

Table B.1: **Parameter Values Used for all Calculations**

Table (B.2) and figure (B.1) represent the case where the transmission cable length is held strictly at integer values of $\frac{n}{2}\lambda$ with C_{stray} parameter set to zero (0.001pF in the simulation). Here, increasing lengths of the $\frac{n}{2}\lambda$ cable introduce more total and resonant portion impedance into the circuit. Figure (B.2) illustrates how the phase is affected by varying the length in steps of $\frac{n}{2}\lambda$. In each case, the circuit could be tuned with a properly shaped Q-curve without any problem. Table (B.4) shows that if the $\frac{n}{2}\lambda$ cable length is not strictly held at integer values of n, one can introduce far too much impedance via the cable and it is possible to tune the circuit in pseudo-parallel mode with an inverted Q-curve as a result. The shaded portions of these tables denote an inverted Q-curve tune. Figures (B.5) and (B.6) indicate the effect on impedance and phase for this case. Table (B.3) and figures (B.3) and (B.4) show the effect of stray capacitance on the tune. Note that the Q-curve flips at stray capacitances of 18pF $<$ C_{stray} $<$ 19pF for 213.080MHz.

true freq (MHz)	$\frac{n}{2}\lambda$	C_{tune} **(pF)**	Z_{RES} **(Ω)**	ϕ_{RES} **(deg)**	Z_{TOT} **(Ω)**	ϕ_{TOT} **(deg)**	**knob**
213.086	0	18.60	10.35	0	8.58	0	0.92978
213.796	1	18.47	11.75	-1.45	9.51	1.175	0.92361
214.498	2	18.35	13.15	-2.75	10.41	2.1703	0.917575
215.235	3	18.23	14.55	-4.00	11.27	3.086	0.9113
216.007	4	18.10	15.96	-5.22	12.11	3.933	0.904801
216.809	5	17.96	17.36	-6.40	12.90	4.7201	0.898124
217.637	6	17.83	18.77	-7.55	13.67	5.452	0.891303
218.486	7	17.69	20.18	-8.68	14.41	6.1344	0.884383
219.357	8	17.55	21.59	-9.77	15.13	6.7695	0.877374
220.244	9	17.41	22.99	-10.84	15.81	7.363	0.870325
221.144	10	17.27	24.39	-11.88	16.47	7.9175	0.863256
222.055	11	17.12	25.79	-12.90	17.11	8.4357	0.856188

Table B.2: **Results for varying $\frac{n}{2}\lambda$ at 213.080MHz** The C_{stray} parameter was kept constant at 0 pF. All Q-curves were normal.

true freq (MHz)	C_{stray} **(pF)**	C_{tune} **(pF)**	Z_{RES} **(Ω)**	ϕ_{RES} **(deg)**	Z_{TOT} **(Ω)**	ϕ_{TOT} **(deg)**	**knob**
223.768	1	16.86	19.21	-7.96	13.90	5.7082	0.843127
245.871	4	13.97	21.10	-9.50	14.88	6.6241	0.69835
289.107	8	10.10	26.52	-12.74	17.43	8.245	0.505094
367.890	12	6.24	44.35	-18.92	23.83	9.2225	0.3119275
442.203	14	4.32	73.94	-24.73	30.51	9.8507	0.2158965
590.636	16	2.42	181.2	-36.49	40.56	7.6142	0.1210179
1232	18	0.56	1270	-71.35	49.35	2.1055	0.0278225
96.676	19	9.03	443	-14.40	45.06	1.4396	4.517
189.269	20	2.36	369	-42.32	45.29	4.7267	1.1785
300.497	22	9.35	273.4	-68.35	46.27	9.0265	0.46753

Table B.3: **Results for varying C_{stray} at 213.080MHz** The number of $\frac{n}{2}\lambda$ was kept constant at $n = 6$. The shaded C_{stray} values correspond to capacitances that produced inverted Q-curves.

true freq (MHz)	$\frac{n}{2}\lambda$	C_{tune} **(pF)**	Z_{RES} **(Ω)**	ϕ_{RES} **(deg)**	Z_{TOT} **(Ω)**	ϕ_{TOT} **(deg)**	**knob**
265.580	6.0625	1.20	23.14	-10.85	15.88	7.35	0.5985615
329.500	6.125	7.78	33.72	-15.61	20.32	9.231	0.3888591
437.390	6.1875	4.41	70.02	-23.76	29.79	9.7841	0.2206777
752.216	6.25	1.49	368.0	-47.76	45.62	5.25675	0.0746112
189.480	6.3125	2.35	380.9	-42.34	45.43	4.5905	1.17585
350.610	6.375	6.87	264.8	-74.88	46.95	9.8395	0.34343
480.281	6.4375	3.66	295.9	-83.42	48.40	9.346	0.18302
624.210	6.5	2.17	405.1	-86.68	49.28	6.975	0.10835
831.910	6.5625	1.22	653.2	-88.32	49.74	4.37	0.061
1274	6.625	0.52	1463	-89.33	49.95	1.95	0.026
73.210	6.8125	157	15.88	-1.19	12.05	0.909	7.87698
131.860	6.875	48.56	16.46	-3.38	12.39	2.5335	2.428116
175.910	6.9375	27.29	17.72	-5.80	13.10	4.253	1.364293

Table B.4: **Results for varying $\frac{n}{2}\lambda$ in non-integer steps at 213.080MHz** The C_{stray} parameter was kept constant at 0 pF. The shaded C_{stray} values correspond to capacitances that produced inverted Q-curves.

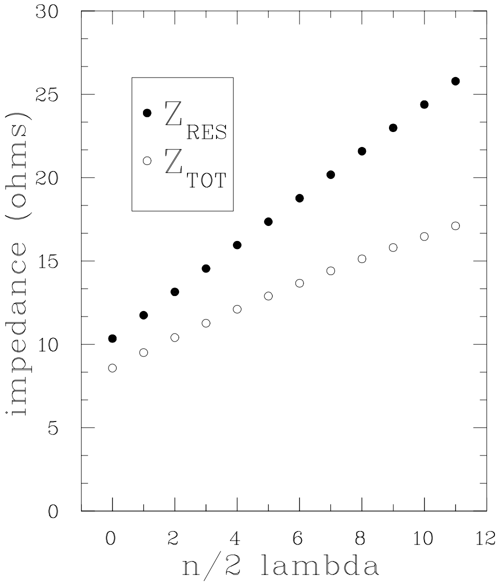

Figure B.1: **Integer** n **Effects on Circuit Impedance Tuned for 213.080MHz**

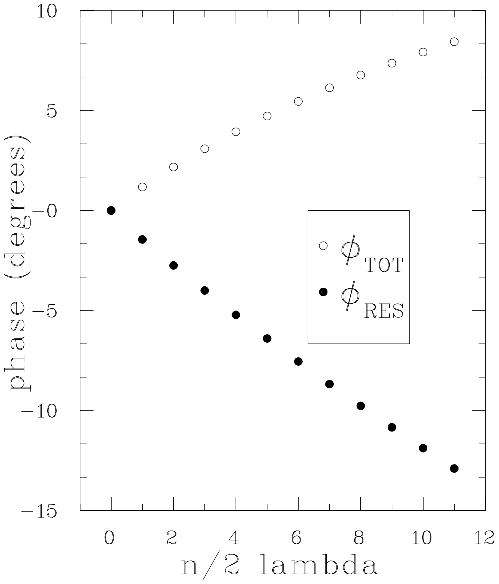

Figure B.2: **Integer n Effects on Phase for 213.080MHz**

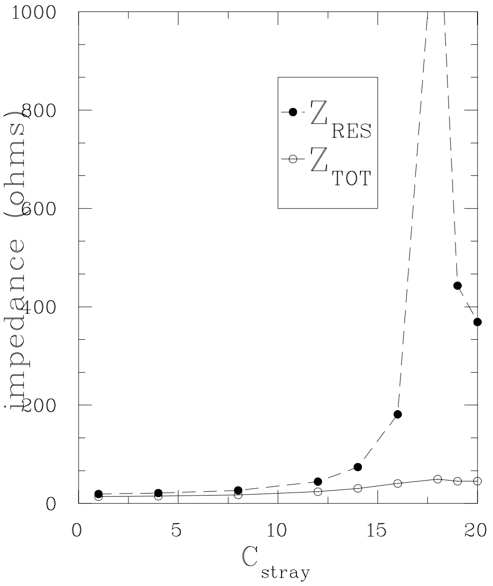

Figure B.3: C_{stray} **Effects on Circuit Impedance Tuned for 213.080MHz** The transmission cable length was held constant at n=6. Note that the Q-curve flips at stray capacitances of 18pF < C_{stray} < 19pF.

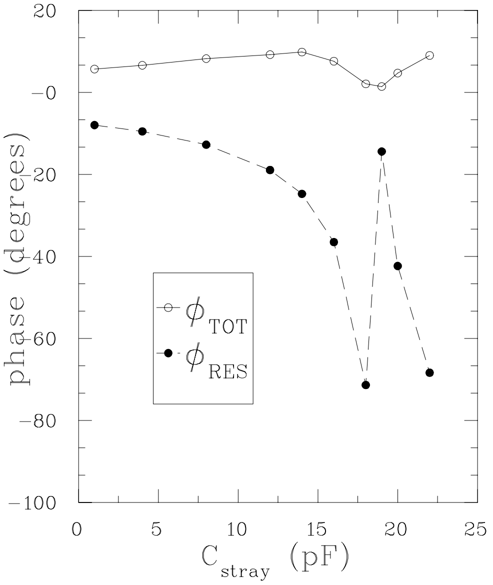

Figure B.4: C_{stray} **Effects on Phase for 213.080MHz**

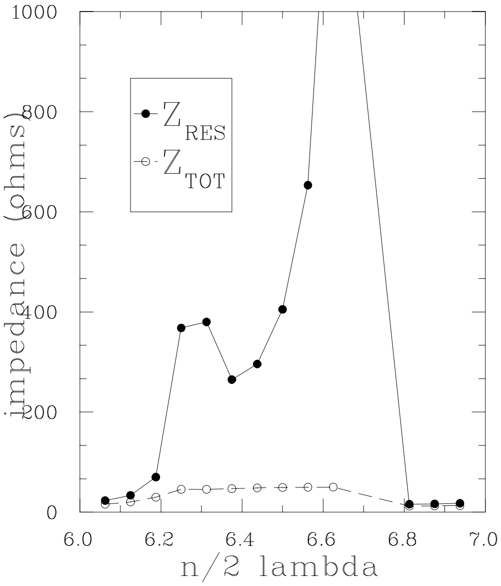

Figure B.5: **Non-integer n/2 Lambda Effects on Impedance for 213.080MHz**

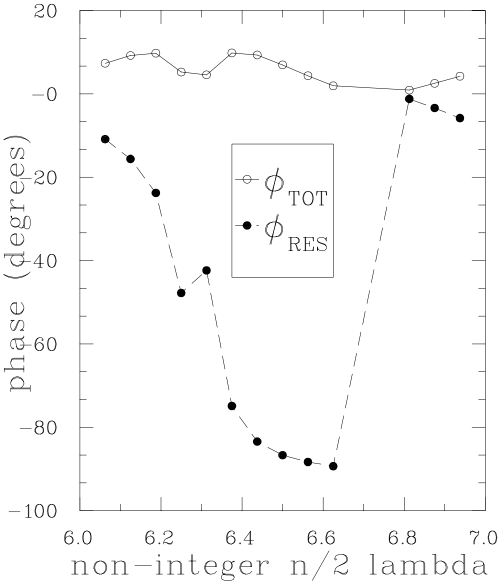

Figure B.6: **Non-integer n/2 Lambda Effects on Phase for 213.080MHz**

Appendix C

Asymmetry Analysis Notes

C.1 Derivation of the Dilution Factor

In this section, only the derivation of the dilution factor for $^{15}\mathrm{NH}_3$ for longitudinal scattering will be considered. The method can be readily applied to $^{6}\mathrm{LiD}$ and transverse scattering.

From our measured asymmetry, we want to extract the asymmetry of electron scattering from a specific nucleon, the proton. Ignoring all asymmetry corrections except the beam and target polarizations, the nucleon asymmetry can be denoted by

$$A_{nuc} = \left[\frac{R_{nuc}^{\downarrow\Uparrow} - R_{nuc}^{\uparrow\Uparrow}}{R_{nuc}^{\downarrow\Uparrow} + R_{nuc}^{\uparrow\Uparrow}}\right] \cdot \left(\frac{1}{P_b P_t}\right) \tag{C.1}$$

where $R_{nuc}^{\downarrow\Uparrow}$ and $R_{nuc}^{\uparrow\Uparrow}$ are defined in equations (3.2). The count rate $R_{nuc}^{\downarrow\Uparrow} + R_{nuc}^{\uparrow\Uparrow}$ is not directly measurable since the total count rate $R_{tot}^{\downarrow\Uparrow} + R_{tot}^{\uparrow\Uparrow}$ from *all materials in the beam* is what the spectrometers actually see. If we consider this in our nucleon asymmetry, we find:

$$A_{nuc} = \frac{\left[\frac{R_{nuc}^{\downarrow\Uparrow} - R_{nuc}^{\uparrow\Uparrow}}{R_{tot}^{\downarrow\Uparrow} + R_{tot}^{\uparrow\Uparrow}}\right]}{\left[\frac{R_{nuc}^{\downarrow\Uparrow} + R_{nuc}^{\uparrow\Uparrow}}{R_{tot}^{\downarrow\Uparrow} + R_{tot}^{\uparrow\Uparrow}}\right]} \cdot \left(\frac{1}{P_b P_t}\right) \tag{C.2}$$

where the raw measured asymmetry is given by the numerator:

$$A_{raw} = \left[\frac{R_{nuc}^{\downarrow\Uparrow} - R_{nuc}^{\uparrow\Uparrow}}{R_{tot}^{\downarrow\Uparrow} + R_{tot}^{\uparrow\Uparrow}}\right] \tag{C.3}$$

and the dilution factor is given by the denominator, the sum of rates off the polarized target nucleons (protons) over the sum of rates off all materials:

$$f = \left[\frac{R_{nuc}^{\downarrow\Uparrow} + R_{nuc}^{\uparrow\Uparrow}}{R_{tot}^{\downarrow\Uparrow} + R_{tot}^{\uparrow\Uparrow}}\right] = \left[\frac{R_{p}^{\downarrow\Uparrow} + R_{p}^{\uparrow\Uparrow}}{R_{tot}^{\downarrow\Uparrow} + R_{tot}^{\uparrow\Uparrow}}\right]. \tag{C.4}$$

This expression for the dilution factor can be calculated from known cross-sections and material thicknesses. However, the above are *measured* event rates that have not been corrected for radiative effects. The dilution factor is calculated using Born cross-sections which must be modified with unpolarized radiative corrections [more on RCs in section (3.3.10)] that serve to radiate the calculated Born dilution factor to include non-Born DIS processes. The Born and fully radiated cross-sections are calculated for each target material listed in table (3.4) with the correction factor defined as:

$$U_{RC} = \frac{\sum_i \sigma_{Born}(i) W(i)}{\sum_i \sigma_{rad}(i) W(i)} \tag{C.5}$$

$$f_{rad} = f_{Born} \cdot U_{RC}^{\text{all}} / U_{RC}^{\text{H}} \tag{C.6}$$

where the summation goes over all the scattering materials in question, $W(i)$ is the relative weight of the number of nuclei for each material, "all" represents the correction for all materials in the target and "H" represents the correction for protons only. Only after this radiated dilution factor is applied to our measured raw asymmetry [section (3.3.6)] that a set of (un)polarized radiative corrections (f_{RC}) A_{RC} is applied to bring the measured asymmetry to a final Born asymmetry. This approach allows us to calculate f_{RC} and A_{RC} for protons (deuterons) only, greatly simplifying the radiative corrections process. The derived rates that follow should also be radiated using unpolarized RCs which are plotted in figures (3.5) and (3.6).

For the following equations, we will leave out U_{RC} for clarity. The proton rates are given by:

$$R_p^{\downarrow\Uparrow} = N_p\big[P_p\sigma_p^{\downarrow\Uparrow} + (1-P_p)\sigma_p\big] \tag{C.7}$$

$$R_p^{\uparrow\Uparrow} = N_p\big[P_p\sigma_p^{\uparrow\Uparrow} + (1-P_p)\sigma_p\big] \tag{C.8}$$

while the rates off all the materials within the acceptance of the spectrometers is given by:

$$\begin{aligned} R_{tot}^{\downarrow\Uparrow} = R_p^{\downarrow\Uparrow} &+ (1-\eta)N_N\cdot\big[P_{15N}\sigma_{15N}^{\downarrow\Uparrow} + (1-P_{15N})\sigma_{15N}\big] \\ &+ \eta N_N\cdot\big[P_{14N}\sigma_{14N}^{\downarrow\Uparrow} + (1-P_{14N})\sigma_{14N}\big] + \sum_i N_i\sigma_i \end{aligned} \tag{C.9}$$

$$\begin{aligned} R_{tot}^{\uparrow\Uparrow} = R_p^{\uparrow\Uparrow} &+ (1-\eta)N_N\cdot\big[P_{15N}\sigma_{15N}^{\uparrow\Uparrow} + (1-P_{15N})\sigma_{15N}\big] \\ &+ \eta N_N\cdot\big[P_{14N}\sigma_{14N}^{\uparrow\Uparrow} + (1-P_{14N})\sigma_{14N}\big] + \sum_i N_i\sigma_i \end{aligned} \tag{C.10}$$

- $\sigma_x^{\downarrow\Uparrow}$ and $\sigma_x^{\uparrow\Uparrow}$ (σ_x) are the polarized (unpolarized) cross-sections of nucleus x, where $\sigma = (\sigma^{\downarrow\Uparrow} + \sigma^{\uparrow\Uparrow})/2$.
- N_p, N_N and N_{He} are the number density of protons, nitrogen and LHe.

- P_p, P_{15N} and P_{14N} are the proton, ^{15}N and ^{14}N polarizations.
- η is the fraction of ^{14}N in ^{15}N in ammonia ($\eta = 0.02$ for our ^{15}NH$_3$).

Combining equations (C.7) thru (C.10) lead to the unpolarized nucleon and total rates:

$$\begin{aligned} R_p^{\downarrow\Uparrow} + R_p^{\uparrow\Uparrow} &= N_p\big[(\sigma_p^{\downarrow\Uparrow} + \sigma_p^{\uparrow\Uparrow})P_p + 2(1-P_p)\sigma_p\big] \\ &= N_p\big[2\sigma_p P_p + 2\sigma_p - 2P_p\sigma_p\big] \\ &= 2N_p\sigma_p \end{aligned} \tag{C.11}$$

$$\begin{aligned} R_{tot}^{\downarrow\Uparrow} + R_{tot}^{\uparrow\Uparrow} = {} & R_p^{\downarrow\Uparrow} + R_p^{\uparrow\Uparrow} + (1-\eta)N_N\big[P_{15N}(\sigma_{15N}^{\downarrow\Uparrow} + \sigma_{15N}^{\uparrow\Uparrow}) + 2(1-P_{15N})\sigma_{15N}\big] \\ & + \eta N_N\big[P_{14N}(\sigma_{14N}^{\downarrow\Uparrow} + \sigma_{14N}^{\uparrow\Uparrow}) + 2(1-P_{14N})\sigma_{14N}\big] + 2\sum_i N_i\sigma_i \\ = {} & 2N_p\sigma_p + (1-\eta)N_N\big[2P_{15N}\sigma_{15N} + 2(1-P_{15N})\sigma_{15N}\big] \\ & + \eta N_N\big[P_{14N}\sigma_{14N} + 2(1-P_{14N})\sigma_{14N}\big] + 2\sum_i N_i\sigma_i \\ = {} & 2N_p\sigma_p + 2(1-\eta)N_N\sigma_{15N} + 2\eta N_N\sigma_{14N} + 2\sum_i N_i\sigma_i \end{aligned} \tag{C.12}$$

and finally we obtain the dilution factor for ^{15}NH$_3$ which is of the form presented in equation (3.12):

$$\begin{aligned} f_{\mathrm{NH3}} = \frac{R_p^{\downarrow\Uparrow} + R_p^{\uparrow\Uparrow}}{R_{tot}^{\downarrow\Uparrow} + R_{tot}^{\uparrow\Uparrow}} &= \frac{N_p\sigma_p}{N_p\sigma_p + (1-\eta)N_N\sigma_{15N} + \eta N_N\sigma_{14N} + \sum_i N_i\sigma_i} \\ &= \frac{N_p\sigma_p}{N_p\sigma_p + N_N\sigma_N + \sum_i N_i\sigma_i} \end{aligned} \tag{C.13}$$

Material	Length (cm)	Density (g/cm3)	Atomic Mass (g/mol)	Z (protons)	N (neutrons)
$^{15}NH_3$	pf × 3.0	0.917	18.024	3 (H_3) 7 (^{15}N)	0 (H_3) 8 (^{15}N)
^{6}LiD	pf × 3.0	0.82	8.03	1 (^2H) 3 (^6Li)	1 (^2H) 3 (^6Li)
^{4}He	(1-pf) × 3.0	0.145	4.0026	2	2

Table C.1: **Selected Target Properties**

noting that the quantity $N_N \sigma_N$ is understood to contain the impurities of ^{15}N & ^{14}N of our target. In order to evaluate (C.13), we need to know the deep inelastic scattering cross-sections for the proton, neutron, ^{15}N, ^{14}N, ^{4}He and the unpolarized nuclei ^{A}X and their corresponding EMC factors.

$$\sigma_{15\mathrm{N}} = (7\sigma_p + 8\sigma_n) g_{\mathrm{emc}}^{15\mathrm{N}} \tag{C.14}$$

$$\sigma_{\mathrm{He}} = (2\sigma_p + 2\sigma_n) g_{\mathrm{emc}}^{\mathrm{He}} \tag{C.15}$$

$$\sigma_{^A X} = (Z\sigma_p + (A - Z)\sigma_n) g_{\mathrm{emc}}^{\mathrm{^AX}} \tag{C.16}$$

The EMC factors take into account that we are scattering off nucleons bound inside a nucleus as opposed to free nucleons [10][22]. σ_p and σ_n can be obtained by using NMC measurements of the unpolarized structure functions F_2^p and F_2^n [104]. Thus, we can use the ratio of these structure functions as the ratio of neutron and proton cross sections

$$\frac{\sigma_n}{\sigma_p} \Longrightarrow \frac{F_2^n(x)}{F_2^p(x)}. \tag{C.17}$$

Using the properties given in table (C.1), the number density of each component can be expressed as follows:

$$N_p = 3 \cdot \left(\frac{\rho_{\mathrm{NH3}}}{A_{\mathrm{NH3}}}\right) \cdot N_A \cdot \mathrm{pf} \cdot l_{tgt} \tag{C.18}$$

$$N_N = \left(\frac{\rho_{\mathrm{NH3}}}{A_{\mathrm{NH3}}}\right) \cdot N_A \cdot \mathrm{pf} \cdot l_{tgt} \tag{C.19}$$

$$N_i = \left(\frac{\rho_i}{A_i}\right) \cdot N_A \cdot l_i \tag{C.20}$$

where $N_{\mathrm{15N}} = (1-\eta) \cdot N_N$ and $N_{\mathrm{14N}} = \eta \cdot N_N$ number densities, ρ is the density, A is the atomic number, $N_A = 6.02 \times 10^{23}$ mol^{-1} is Avagadro's number, pf is the packing fraction as explained in section (3.3.7) and l is the length of the material in question. Dividing the numerator and denominator of equation (C.13) by σ_p, plugging in equations (C.14) thru (C.16) for the appropriate cross-sections and using the appropriate number densities, we find the numerator of f to be:

$$3 \cdot \left(\frac{\rho_{\mathrm{NH3}}}{A_{\mathrm{NH3}}}\right) \cdot N_A \cdot \mathrm{pf} \cdot l_{tgt} \cdot \sigma_p \tag{C.21}$$

and the denominator of f to be:

$$\begin{aligned}
&3 \cdot \left(\frac{\rho_{\mathrm{NH3}}}{A_{\mathrm{NH3}}}\right) \cdot N_A \cdot \mathrm{pf} \cdot l_{tgt} \cdot \sigma_p \\
&+ (1-\eta)\left(\frac{\rho_{\mathrm{NH3}}}{A_{\mathrm{NH3}}}\right) \cdot N_A \cdot \mathrm{pf} \cdot l_{tgt} \cdot (7\sigma_p + 8\sigma_n) g_{\mathrm{emc}}^{\mathrm{15N}} \\
&+ \eta\left(\frac{\rho_{\mathrm{NH3}}}{A_{\mathrm{NH3}}}\right) \cdot N_A \cdot \mathrm{pf} \cdot l_{tgt} \cdot (7\sigma_p + 7\sigma_n) g_{\mathrm{emc}}^{\mathrm{14N}} \\
&+ \left(\frac{\rho_{\mathrm{He}}}{A_{\mathrm{He}}}\right) \cdot N_A \cdot \left[(1-\mathrm{pf}) \cdot l_{tgt} + l_{\mathrm{He(out)}}\right] \cdot (2\sigma_p + 2\sigma_n) g_{\mathrm{emc}}^{\mathrm{He}} \\
&+ \sum_j \left(\frac{\rho_j}{A_j}\right) \cdot N_A \cdot l_j \cdot \sigma_j \cdot g_{\mathrm{emc}}^{j}
\end{aligned} \tag{C.22}$$

where j is the sum over all other materials except He, since we took He out of the summation for clarity. The above expressions, with unpolarized radiative corrections, make up the calculation of the dilution factor for ammonia. A similar procedure was carried out to calculate the factor for lithium deuteride:

$$f_{\mathrm{LiD}} = \frac{N_p\sigma_p + N_n\sigma_n}{N_p\sigma_p + N_n\sigma_n + N_{\mathrm{Li}}\sigma_{\mathrm{Li}} + N_{\mathrm{He}}\sigma_{\mathrm{He}} + \sum_i N_i\sigma_i}. \tag{C.23}$$

More information on this derivation can be found in references [111, 112].

Date	Run	Insert	Solid Tgt	Cell	Tgt	H/D Coil	Bottle	Dose	Size
Feb07-Mar17	0002-1874	01 (C)	small C #2	Upper	^{6}LiD	Al/Al	52	3.7	1.0-2.0
			large Be #2	Lower	^{6}LiD	Al/Al	31	2.3	2.5-3.5
Mar17-Mar19	1876-1986	02 (B)	small Be #3	Upper	^{15}NH$_3$	Al/Al	E155 7&8	1.0	scraps
			large C #2	Lower	^{15}NH$_3$	Al/Al	E155 5&6	1.0	2.5-3.5
Mar19-Mar28	1987-2574	03 (D)	small Be #1	Upper	^{15}NH$_3$	Al*/Al	E155 7&8	1.0	scraps
			large C #1	Lower	^{15}NH$_3$	CuNi*/Al	E155 5&6	1.0	2.5-3.5
Mar28-Apr02	2575-2853	04 (B)	small Be #3	Upper	^{15}NH$_3$	CuNi*/Al	E155 7&8	1.0	scraps
			large C #1	Lower	^{15}NH$_3$	CuNi*/Al	E143 101&28	4/1	2.5-3.5
Apr02-Apr11	2859-3404	05 (A)	small C #2	Upper	^{6}LiD	none/Al	56&71	2.6	1.0-2.0
			large Be #3	Lower	^{6}LiD	CuNi*/CuNi	41	2.0	1.0-2.0
Apr11-Apr16	3405-3701	06 (B)	small Be #3	Upper	^{15}NH$_3$	CuNi*/Al	E143 102&28	2/1	2.5-3.5
			large C #2	Lower	^{15}NH$_3$	CuNi*/Al	E155 5&6	1.0	2.5-3.5
Apr16-Apr18	3702-3752	07 (B)	small Be #3	Upper	^{14}NH$_3$	CuNi*/Al	E143 15&6		2.5-3.5
			large C #2	Lower	^{15}NH$_3$	CuNi*/Al	E155 8&5**		scraps/2.5
Apr21-Apr22	3753-3782	08 (A)	small C #3	Upper	empty				
			large Be #3	Lower	empty				
Apr22-Apr23	3783-3786	09 (D)	small Be #1	Upper	empty				
			large C #1	Lower	empty				
Apr23-Apr30	3787-4388	10 (A)	small C #4	Upper	^{6}LiD	none/Al			
			large C #2	Lower	^{15}NH$_3$	CuNi*/none			

Table C.2: **Polarized Target Insert History** The table above indicates the targets used during the E155 experimental run, which ran through the months of February, March and April 1997. There were four insert sticks labeled A,B,C and D used during the runs. Each stick had two solid targets, ^{12}C and ^{9}Be , and two target cells holding the polarized target material, ^{6}LiD or ^{15}NH$_3$. Each target cell utilized up to two NMR coils, one optimized for the proton and another for the deuteron. These coils were made out of aluminum wire or copper-nickel tubing. The asterisk in the *coil* category indicates a *loop* proton coil, whereas no asterisk indicates a *straight* proton coil. The *bottle* category indicates the source of the polarized target material used, with the pre-experiment irradiation *dose* value in units of 10^{17} electrons per cm^2. The polarized target granule *size* is given in units of mm.

* indicates a loop proton coil, whereas no asterisk indicates straight proton coil

**includes bottle E143 #28

Appendix D

Lithium Deuteride Composition Analyses

Two sets of composition analyses were done on the E155 collaboration's ^{6}LiD polarized target material. An original set of analyses were done to three raw samples at Los Alamos National Laboratory back in December of 1996. In January of 1999, another set of three samples were analyzed at Oak Ridge Centers for Manufacturing Technology (ORCMT), Lockheed Martin Energy Systems, in the Analytical Services Organization (ASO) labs. The second set of ^{6}LiD analyses became necessary when the collaboration discovered data from the ^{6}LiD target insert 5 Lower of E155 gave results that deviated from world data by a significant amount [113]. The details of all these analyses are provided below.

D.1 LiD Chemistry Background

Lithium hydride belongs to the family of compounds known as *hydrides*, the general name for any binary compound comprising one other element and hydrogen [114].

Hydride compounds containing *deuterons* (^{2}H) in place of *protons* (^{1}H) will have nearly the same chemical properties as for normal hydrides, and are called *deuterides.* The bond between Li and H(D) is ionic, where the hydrogen (deuteron) is present as a negatively charged hydride ion H^- (deuteride ion D^-). Therefore, lithium deuteride can be best labeled as an *alkali metal ionic deuteride.*

Lithium Deuteride can be synthesized by reacting deuterium directly with lithium via the reaction [115]

$$2\mathrm{Li} + \mathrm{D}_2 \longrightarrow 2\mathrm{LiD}. \tag{D.1}$$

Lithium hydride reacts readily with water in the air to produce lithium hydroxide and hydrogen gas, which is true for lithium deuteride as well.

$$\mathrm{LiH} + \mathrm{H}_2\mathrm{O} \longrightarrow \mathrm{LiOH} + \mathrm{H}_2 \tag{D.2}$$

$$\mathrm{LiD} + \mathrm{H}_2\mathrm{O} \longrightarrow \mathrm{LiOH} + \mathrm{HD} \tag{D.3}$$

From these reactions, one can see that if one has a pure sample of LiD(H) with no oxygen content, any exposure to moisture will result in -OH replacing -D(H). The result is gaining a hydrogen and oxygen for every deuteron lost.

D.2 Los Alamos Analysis

The E155 polarized target group obtained some ^{6}LiD in the summer of 1996 from Lawrence Livermore National Laboratory (LLNL) for use in the upcoming DIS experiment in End Station A at SLAC. The material arrived in the form of a large solid

ID	Weight (mg)	%H	%D	Total H+D Collected	% Theory H	Weight %(H+D)	%6Li	%7Li
1	44.3	7.84	92.15	1.5439	56	13.49	95.390	4.610
2	38.9	2.31	97.69	1.9806	82	20.24	95.406	4.594
3	38.8	2.51	97.49	2.1397	89	21.93	95.389	4.611

Table D.1: **Los Alamos Analysis Results**

UVA ID	ACO ID	% Weight Oxygen	Isotope % D	Isotope % 6Li
1198-1	R990060000	$3.29 \pm .20$	$97.6 \pm .10$	$95.57 \pm .10$
1198-2	R990060001	63.8 ± 2	32 ± 1	$98.9 \pm .10$
1198-3	R990060002	$1.50 \pm .20$	$98.9 \pm .10$	$95.55 \pm .10$

Table D.2: **Oak Ridge Analysis Results**

cylinder packaged in an air tight container to prevent the material from taking on oxygen from the moisture in the air. The relatively large percentage of ^{7}Li in ^{6}Li is due to the fact that ^{6}LiD comes from the hydrogen bomb industry.

Three random samples from the original raw material were sent to Los Alamos for H/D ratio and Li-6 and Li-7 concentration measurements. The analysis results are presented in table (D.1).

D.3 Oak Ridge Analysis

The University of Virginia Polarized Target Group requested the services of ORCMT to provide analysis of Lithium-6 Deuteride for percent oxygen, H/D ratio, and Li-6 and Li-7 concentrations. The requested samples were packed using a dry nitrogen atmosphere glove bag apparatus and used the services of Department of Transportation (DOT) trained personnel to complete the packing and ship the samples according to DOT guidelines. Results in table (D.2) were provided on 28Jan99. Table (D.3) identifies the samples sent to ASO, and table (D.4) lists the analysis methodology.

UVA ID	Quantity Sent	Description
1198-1	2.8g	Black granules of ^{6}LiD from 5 Lower target cell
1198-2	3.4g	Grayish-white powder from outer layer of raw ^{6}LiD material
1198-3	3.2g	Brown chunks from core of raw ^{6}LiD material

Table D.3: **Lithium Deuteride Sample Identity**

Analysis	^{6}LiD Required	Procedure
Oxygen Content	0.7g	measurement of H_2O content in ^{6}LiD done by neutron activation analysis
H/D Ratio	1.5g	sample is reduced to give off all H(D) gas, then gas is oxidized to produce water then water density is measured to determine H_2O/D_2O ratio
^{6}Li/^{7}Li Ratio	0.1g	isotopic ratio mass spectroscopy analysis

Table D.4: **Analysis Methodology**

SAMPLE	Lithium:		Hydrogen:		Oxygen:
1198-1	^{6}Li	^{7}Li	^{2}H	^{1}H	^{16}O
isotope %	$95.57 \pm .10$	$4.43 \pm .10$	$97.6 \pm .10$	$2.4 \pm .10$	100
atomic weight	6.0150	7.0150	2.0140	1.0080	15.994
% weight	$69.07 \pm .17$	$3.73 \pm .08$	$23.62 \pm .06$	$0.29 \pm .04$	$3.29 \pm .20$
atom %	$47.38 \pm .08$	$2.20 \pm .006$	$48.39 \pm .01$	$1.19 \pm .01$	$0.85 \pm .005$

SAMPLE	Lithium:		Hydrogen:		Oxygen:
1198-2	^{6}Li	^{7}Li	^{2}H	^{1}H	^{16}O
isotope %	$95.52 \pm .10$	$4.48 \pm .10$	32 ± 1	68 ± 1	100
atomic weight	6.0150	7.0150	2.0140	1.0080	15.994
% weight	$28.14 \pm .56$	$1.54 \pm .05$	$3.16 \pm .12$	$3.36 \pm .08$	63.8 ± 2
atom %	33.94 ± 1.92	$1.59 \pm .09$	$11.37 \pm .12$	$24.16 \pm .22$	28.94 ± 1.65

SAMPLE	Lithium:		Hydrogen:		Oxygen:
1198-3	^{6}Li	^{7}Li	^{2}H	^{1}H	^{16}O
isotope %	$95.55 \pm .10$	$4.45 \pm .10$	$98.9 \pm .10$	$1.1 \pm .10$	100
atomic weight	6.0150	7.0150	2.0140	1.0080	15.994
% weight	$70.22 \pm .18$	$3.81 \pm .09$	$24.33 \pm .06$	$0.14 \pm .04$	$1.50 \pm .20$
atom %	$47.59 \pm .08$	$2.22 \pm .006$	$49.26 \pm .01$	$0.55 \pm .01$	$0.38 \pm .008$

Table D.5: **% Weight and Atom % Composition of Lithium Deuteride** Lithium deuteride composition as deterimined by Oak Ridge isotopic and oxygen content measurements assuming only LiD, LiH and LiOH in our samples.

Notice that samples 1198-1 and 1198-3 scale as expected. The larger the % oxygen content, the smaller % deuteron content. Once again, this is because water reacts with LiD, replacing the -D with -OH, hence increasing the hydrogen and oxygen content, hence decreasing the amount of D as compared to H in our samples.

Let us calculate the % weight and atom % of each element in the sample using the information provided by the Oak Ridge measurements and assuming that only LiD, LiH and LiOH exist in our target samples. Results are provided in table (D.5).

$$\begin{aligned} \mathrm{SUM}_{\mathrm{weight}} &= x(\mathrm{LiD}) + z(\mathrm{LiH}) + y(\mathrm{LiOH}) \\ &= x\mathrm{Li} + x\mathrm{D} + z\mathrm{Li} + z\mathrm{H} + y\mathrm{Li} + y\mathrm{O} + y\mathrm{H} \\ &= (x+y+z)\mathrm{Li} + (y+z)\mathrm{H} + y\mathrm{O} \end{aligned} \tag{D.4}$$

the fractions x, y and z are given by:

$$x + y + z = 1 \tag{D.5}$$

$$x = \frac{\%D}{100} \tag{D.6}$$

$$y + z = \frac{\%H}{100} \tag{D.7}$$

the atomic weight of each element is given by:

$$Li = At.Wt.Li \tag{D.8}$$

$$D = At.Wt.D \tag{D.9}$$

$$H = At.Wt.H \tag{D.10}$$

$$O = At.Wt.16O \tag{D.11}$$

$$Li = \frac{\%6Li}{100} At.Wt.6Li + \frac{\%7Li}{100} At.Wt.7Li \tag{D.12}$$

The quantities %6Li, %7Li, %D and %H are isotope percentages provided by Oak Ridge on a 0 to 100% scale. In addition, the %Wt.16O was also provided by Oak Ridge. From the above equations and the given percent composition, we can solve for the % weight for each element:

$$\%Wt.6Li = \frac{\%6Li \cdot At.Wt.6Li}{\mathrm{SUM}_{\mathrm{weight}}} \tag{D.13}$$

$$\%Wt.7Li = \frac{\%7Li \cdot At.Wt.7Li}{\mathrm{SUM}_{\mathrm{weight}}} \tag{D.14}$$

$$\%Wt.D = \frac{\%D \cdot At.Wt.D}{\mathrm{SUM}_{\mathrm{weight}}} \tag{D.15}$$

$$\%Wt.H = \frac{\%H \cdot At.Wt.H}{\mathrm{SUM}_{\mathrm{weight}}} \tag{D.16}$$

$$\%Wt.16O = \frac{y \cdot At.Wt.16O}{\mathrm{SUM}_{\mathrm{weight}}} \tag{D.17}$$

From here we can go on to solve for the atom % composition of each element in our samples using a quantity labeled as $\mathrm{SUM}_{\mathrm{atom}}$:

$$\begin{aligned}\mathrm{SUM}_{\mathrm{atom}} = \bigg(& \frac{\%Wt.6Li}{At.Wt.6Li} + \frac{\%Wt.7Li}{At.Wt.7Li} + \frac{\%Wt.D}{At.Wt.D} \\ & + \frac{\%Wt.H}{At.Wt.H} + \frac{\%Wt.16O}{At.Wt.16O} \bigg) \cdot \mathrm{SUM}_{\mathrm{weight}}\end{aligned} \tag{D.18}$$

$$atom\%6Li = \frac{\%Wt.6Li \cdot \mathrm{SUM}_{\mathrm{weight}}}{At.Wt.6Li \cdot \mathrm{SUM}_{\mathrm{atom}}} \tag{D.19}$$

$$atom\%7Li = \frac{\%Wt.7Li \cdot \mathrm{SUM}_{\mathrm{weight}}}{At.Wt.7Li \cdot \mathrm{SUM}_{\mathrm{atom}}} \tag{D.20}$$

$$atom\%D = \frac{\%Wt.D \cdot \mathrm{SUM}_{\mathrm{weight}}}{At.Wt.D \cdot \mathrm{SUM}_{\mathrm{atom}}} \tag{D.21}$$

$$atom\%H = \frac{\%Wt.H \cdot \mathrm{SUM}_{\mathrm{weight}}}{At.Wt.H \cdot \mathrm{SUM}_{\mathrm{atom}}} \tag{D.22}$$

$$atom\%16O = \frac{\%Wt.16O \cdot \mathrm{SUM}_{\mathrm{weight}}}{At.Wt.16O \cdot \mathrm{SUM}_{\mathrm{atom}}} \tag{D.23}$$

Likewise, all errors are propagated through from knowing the errors on %6Li, %7Li, %D, %H and %Wt.16O.

D.4 Conclusions

The Oak Ridge analysis shows that our lithium deuteride target material from target insert #5 lower cell had an oxygen contamination of about 3.3%. When compared to a raw ^{6}LiD sample which had a 1.5% oxygen content, the 3.3% oxygen content in the material from #5 lower cell indicates that contamination occurred during normal handling of the target. Each time an insert was loaded and unloaded, there was a chance that some air got in contact with the target material and picked up some water contamination. Tables (D.6) and (D.7) show the target composition numbers used in the preliminary E155 student analysis. These lithium deuteride numbers were originally based solely on the Los Alamos composition analyses. For the final analysis, a 3.3% oxygen correction factor was used in the calculation of the ^{6}LiD dilution factor [82].

Element	Z	A	Atomic Weight	Abundance
N	7	14	14.003074	2%
		15	15.000109	98%
H	1	1	1.007825	99.985%
		2	2.014102	0.015%

Table D.6: **^{15}NH$_3$ Proton Target**

Element	Z	A	Atomic Weight	Abundance
Li	3	6	6.015123	95.4%
		7	7.016001	4.6%
H	1	1	1.007825	2.5%
		2	2.014102	97.5%

Table D.7: **^{6}LiD Deuteron Target**

Appendix E

ISRA Details

Fits to g_1/F_1 to E155 deuteron and world proton data were used to evaluate the values and errors on the first moments Γ_1^p, Γ_1^d, Γ_1^n and $\Gamma_1^{(p-n)}$. The errors on the fitted functions and their integration were readily obtained from the error information provided by the fitting procedure.

E.1 Error on a Function

The ISRA fitting was done using GNUPLOT Linux version 3.7 which employed the Marquardt-Levenberg algorithm to minimize the *chi-square* χ^2, *goodness-of-fit* criterion, between the central values of the fit $f(x_i)$ and the data f_i.

$$\chi^2 = \sum_{i=1}^{N} \left[\frac{[f_i - f(x_i)]^2}{\sigma_i^2} \right]. \tag{E.1}$$

The *reduced chi-square* χ^2_ν is defined as the chi-square per degree of freedom, where ν is the number of degrees of freedom.

$$\chi^2_\nu = \frac{\chi^2}{\nu} \tag{E.2}$$

$$\nu = N - n - 1 \tag{E.3}$$

N is the number of data points and n is the number of parameters in the fitted function. The data points to be fitted were weighted (w) by their statistical error (σ), those with smaller statistical error influencing the fit more than those with greater error.

$$w = \frac{1}{\sigma^2} \tag{E.4}$$

The total standard error on the fitted function was calculated via the reported standard deviations, σ_i, of the fit parameters and the given *correlation* matrix, $\boldsymbol{\rho}$. For example, for an arbitrary function $f(x)$ with two parameters $a \pm \delta a$ and $b \pm \delta b$, the error is given by δf, which is obtained from information given in the *error* (*variance-covariance*) matrix, $\boldsymbol{\epsilon}$.

$$(\delta f)^2 = \left(\frac{\partial f}{\partial a}\right)^2 \cdot \sigma^2_{aa} + 2\left(\frac{\partial f}{\partial a}\right) \cdot \left(\frac{\partial f}{\partial b}\right) \cdot \sigma^2_{ab} + \left(\frac{\partial f}{\partial b}\right)^2 \cdot \sigma^2_{bb} \tag{E.5}$$

$$\boldsymbol{\epsilon} = \begin{bmatrix} \sigma^2_{aa} & \sigma^2_{ab} \\ \sigma^2_{ba} & \sigma^2_{bb} \end{bmatrix} \tag{E.6}$$

$$\boldsymbol{\rho} = \begin{bmatrix} \rho_{aa} & \rho_{ab} \\ \rho_{ba} & \rho_{bb} \end{bmatrix} \tag{E.7}$$

In the error matrix $\boldsymbol{\epsilon}$, the diagonal elements σ_{ii}^2 are the *variances*, and the off-diagonal elements σ_{ij}^2 $(i \neq j)$ are the *covariances*. Note that $\sigma_{ii}^2 = (\sigma_i)^2$. The correlation matrix $\boldsymbol{\rho}$ contains the *correlation coefficients* that describes the relationship between all the parameters in the fitted function. The diagonal elements ρ_{ii} are always 1, since each parameter is totally correlated with itself. If all parameters are uncorrelated, then the off-diagonal matrix elements would be zero. If a given pair of parameters are totally correlated, then their off-diagonal elements would be of unit magnitude, with a sign defining the relation as proportional or inversely proportional. One can obtain the variances and covariances from the parameter standard deviations and their correlation coefficients by way of equation (E.8).

$$\sigma_{ij}^2 = \rho_{ij} \cdot \sigma_i \cdot \sigma_j \tag{E.8}$$

E.2 Error on an Integral

The integral of an arbitrary function can be accomplished analytically or numerically. Finding the integral analytically is the preferred method, but many parameterizations are very complicated and thus lend themselves to numerical integration. Numerically, the integral I and its error δI of a function $f(x)$ with two parameters $a \pm \delta a$ and $b \pm \delta b$ and x-bin width Δ_i is given by

$$I = \int f(x)dx = \sum_i^N \Big(f(x_i) \cdot \Delta_i \Big) \tag{E.9}$$

$$
\begin{aligned}
(\delta I)^2 = & \left(\sum_i^N \Delta_i \frac{\partial f(x_i)}{\partial a}\right)^2 \cdot \sigma_{aa}^2 + 2\left(\sum_i^N \Delta_i \frac{\partial f(x_i)}{\partial a}\right) \cdot \left(\sum_i^N \Delta_i \frac{\partial f(x_i)}{\partial b}\right) \cdot \sigma_{ab}^2 \\
& + \left(\sum_i^N \Delta_i \frac{\partial f(x_i)}{\partial b}\right)^2 \cdot \sigma_{bb}^2.
\end{aligned}
\tag{E.10}
$$

The above methods can be extended to the exact functional forms used for the analysis in this dissertation. Specifically, fits to g_1/F_1 for the proton and deuteron were done using the functional form as in equation (4.16).

The first moments of the spin structure functions were evaluated at a common $Q_o^2 = 5$ GeV^2 using parameterizations of g_1/F_1 multiplied by an effective parameterization of F_1 via equation (1.36) using the NMC fit to F_2 [104] and the SLAC global fit to R [105] such that

$$
\Gamma_1 = \int g_1(x)dx = \sum_i^N \left((\frac{g_1}{F_1})_{fit} \cdot F_1(x_i, Q_o^2) \cdot \Delta_i \right) \tag{E.11}
$$

The spin averaged structure function for the deuteron as a function of Q^2 at 16 different values of x is plotted along with the NMC fits in figures (E.1) and (E.2).

The ISRA determined the error on the ISRA fits and their integrals via 5x5 correlation matrix for proton

$$
\begin{bmatrix}
1.000 & -.857 & 0.926 & -.179 \\
-.857 & 1.000 & -.753 & 0.110 \\
0.926 & -.753 & 1.000 & 0.103 \\
-.179 & 0.110 & 0.103 & 1.000
\end{bmatrix}
\tag{E.12}
$$

parameter	**ISRA p**	**ISRA d**	**E155 p**	**E155 n**
a	1.275 ± 0.105	1.411 ± 0.461	0.817 ± 0.230	-0.013 ± 0.038
b	——	——	1.014 ± 0.636	-0.330 ± 0.153
c	-0.677 ± 0.251	-0.758 ± 0.717	-1.489 ± 0.600	-0.761 ± 0.590
α	0.806 ± 0.039	1.445 ± 0.235	0.700 ± 0.082	-0.335 ± 0.524
β	-0.153 ± 0.066	0.314 ± 1.346	-0.037 ± 0.061	0.129 ± 0.459

Table E.1: **Standard Deviations on the Fits**

and correlation matrix for deuteron

$$\begin{bmatrix} 1.000 & -.867 & 0.898 & 0.295 \\ -.867 & 1.000 & -.771 & -.335 \\ 0.898 & -.771 & 1.000 & 0.645 \\ 0.295 & -.335 & 0.645 & 1.000 \end{bmatrix}. \tag{E.13}$$

There are separate correlation matrices for each fit since each parameterization was fitted to different data sets and are uncorrelated. Equation (E.8) and the standard deviations given in table (E.1) must be used to obtain the variances and covariances in order to evaluate the error on the ISRA fits.

The ISRA determined the error on the E155 global fits and their integrals via the 10x10 error matrix

$$\begin{bmatrix} 0.0527 & -.1417 & 0.1184 & 0.0185 & 0.0018 & 0.0004 & -.0013 & 0.0024 & -.0024 & 0.0078 \\ -.1417 & 0.4039 & -.3628 & -.0484 & -.0031 & -.0013 & 0.0014 & -.0006 & 0.0125 & -.0156 \\ 0.1184 & -.3628 & 0.3605 & 0.0391 & 0.0006 & 0.0016 & 0.0022 & -.0115 & -.0197 & 0.0071 \\ 0.0185 & -.0484 & 0.0391 & 0.0067 & 0.0012 & 0.0001 & -.0005 & 0.0011 & -.0005 & 0.0036 \\ 0.0018 & -.0031 & 0.0006 & 0.0012 & 0.0037 & 0.0000 & -.0003 & 0.0007 & 0.0007 & 0.0042 \\ 0.0004 & -.0013 & 0.0016 & 0.0001 & 0.0000 & 0.0014 & 0.0047 & -.0190 & -.0196 & 0.0005 \\ -.0013 & 0.0014 & 0.0022 & -.0005 & -.0003 & 0.0047 & 0.0235 & -.0880 & -.0700 & -.0142 \\ 0.0024 & -.0006 & -.0115 & 0.0011 & 0.0007 & -.0190 & -.0880 & 0.3477 & 0.2742 & 0.0329 \\ -.0024 & 0.0125 & -.0197 & -.0005 & 0.0007 & -.0196 & -.0700 & 0.2742 & 0.2744 & 0.0298 \\ 0.0078 & -.0156 & 0.0071 & 0.0036 & 0.0042 & 0.0005 & -.0142 & 0.0329 & 0.0298 & 0.2107 \end{bmatrix} \tag{E.14}$$

given for the correlated proton and neutron (hence deuteron) fits. The standard deviations on the E155 fit parameters are also given in table (E.1).

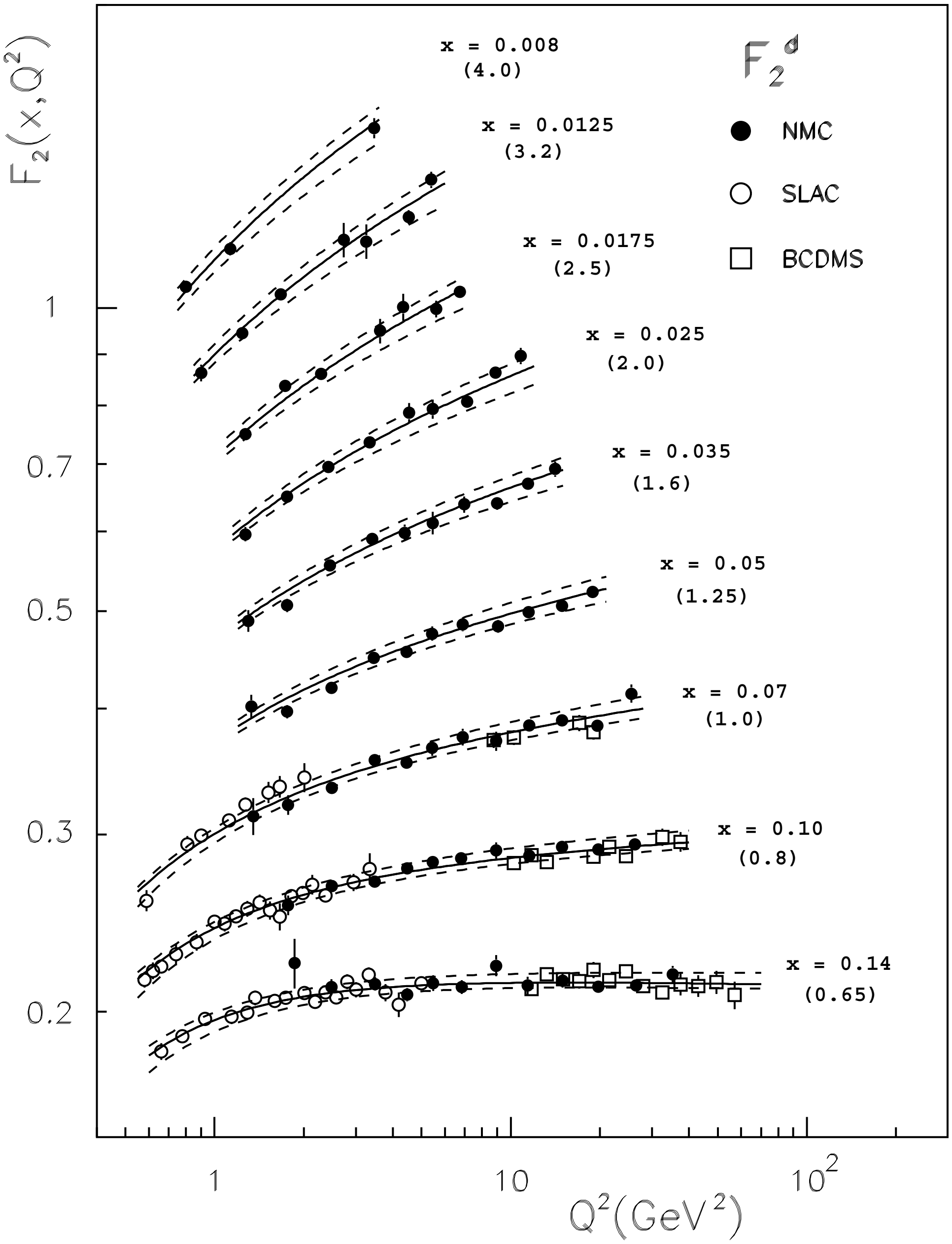

Figure E.1: F_2 **NMC** [104]

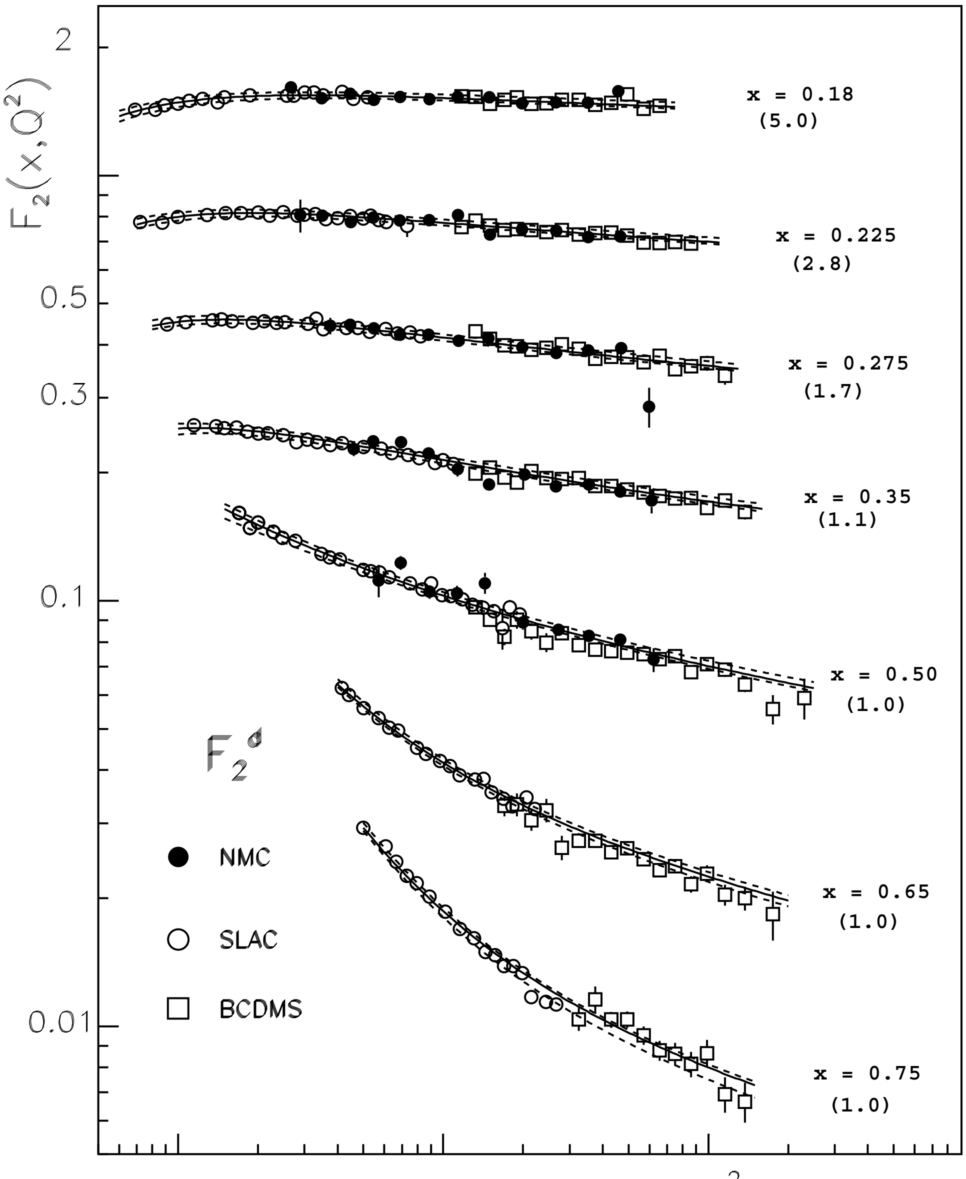

Figure E.2: F_2 **NMC** [104]

Bibliography

[1] R. Hofstadter, *Nuclear and Nucleon Structure*, W. A. Benjamin, Inc., (1963).

[2] A. Bodek *et al*, *Phys. Lett.* **B51** (1974) 417.

[3] A. Pickering, *Constructing Quarks*, University of Chicago Press, (1984), A sociological history of particle physics.

[4] J. D. Bjorken and E. A. Paschos, *Phys. Rev.* **185** (1969) 1975.

[5] L. Hoddeson *et al*, ed., *The Rise of the Standard Model*, Cambridge University Press, (1997).

[6] M. Gell-Mann, *Phys. Lett.* **8** (1964) 214.

[7] G. Zweig, CERN-TH-412, (1964).

[8] M. J. Alguard *et al*, *Phys. Rev. Lett.* **37** (1976) 1261.

[9] G. Baum *et al*, *Phys. Rev. Lett.* **51** (1983) 1135.

[10] J. Ashman *et al*, *Phys. Lett.* **B206** (1988) 364.

[11] E. Leader and M. Anselmino, *Z. Phys.* **C41** (1988) 239.

[12] T. Cuhadar, Spin Crisis, SMC webpages, (1995).

[13] F. E. Close, in *The Spin Structure of the Nucleon, International School of Nucleon Structure: 1st Course*, 628, (1995).

[14] S. E. Kuhn, *Nucleon Structure Functions: Experiments and Models*, HUGS 97, Technical note, (1997), unpublished article gives a simple, intuitive introduction into the physics and the experimental techniques of structure function measurements.

[15] R. L. Jaffe and A. Manohar, *Nucl. Phys.* **B337** (1990) 509.

[16] P. Anthony *et al*, *Phys. Lett.* **B463** (1999) 339.

[17] E. Leader and E. Predazzi, *An introduction to gauge theories and modern particle physics*, Cambridge University Press, (1996).

[18] V. W. Hughes and J. Kuti, *Ann. Rev. Nucl. Part. Sci.* **33** (1983) 611.

[19] C. Carlson and W. Tung, *Phys. Rev.* **D5** (1972) 721.

[20] A. J. G. Hey and J. E. Mandula, *Phys. Rev.* **D5** (1972) 2610.

[21] F. Halzen and A. D. Martin, *Quarks & Leptons: An Introductory Course in Modern Particle Physics*, John Wiley & Sons, (1984).

[22] R. G. Roberts, *The Structure of the Proton*, Cambridge University Press, (1990).

[23] M. Anselmino, A. Efremov and E. Leader, *Phys. Rep.* **261** (1995) 1.

[24] R. Windmolders, *Int. J. Mod. Phys.* **A7** (1992) 639.

[25] D. H. Perkins, *Introduction to High Energy Physics*, Addison-Wesley Publishing Company, (1982).

[26] T. Pussieux and R. Windmolders, (1995), CEA-Dapnia-SPhN-95-010, CERN Library SCAN-9508126.

[27] M. Doncel and E. de Rafael, *Nuovo Cimento* **4A** (1971) 363.

[28] J. Soffer and O. V. Teryaev, *hep-ph/9906455* (1999).

[29] K. Abe *et al*, *Phys. Rev.* **D58** (1998) 112003.

[30] N. Isgur, in *The Spin Structure of the Nucleon, International School of Nucleon Structure: 1st Course*, 260, (1995).

[31] D. Haidt *et al*, *Eur. Phys. J.* **C3** (1998) 1.

[32] R. D. Erbacher, *New F and D Constants*, E155, Technical Note 69, (1998), unpublished.

[33] G. 't Hooft and M. Veltman, *Nucl. Phys.* **B44** (1972) 189.

[34] R. D. Ball, S. Forte and G. Ridolfi, *Phys. Lett.* **B378** (1996) 255.

[35] T. J. Liu, J. McCarthy and O. A. Rondon, *Phys. Rev.* **D54** (1996) 2391.

[36] S. A. Larin and J. A. M. Vermaseren, *Phys. Lett.* **B259** (1991) 345.

[37] R. L. Jaffe, in *The Spin Structure of the Nucleon, International School of Nucleon Structure: 1st Course*, 42, (1995).

[38] R. L. Jaffe and X. Ji, *Phys. Rev.* **D43** (1991) 724.

[39] K. G. Wilson, *Phys. Rev.* **179** (1969) 1499.

[40] P. Anthony *et al*, *Phys. Lett.* **B 458** (1999) 529.

[41] S. Wandzura and F. Wilczek, *Phys. Rev.* **B72** (1977) 195.

[42] J. D. Bjorken, *Phys. Rev.* **148** (1966) 1467.

[43] J. Ellis and R. Jaffe, *Phys. Rev.* **D9** (1974) 1444.

[44] S. A. Larin, *Phys. Lett.* **B334** (1994) 192.

[45] B. Ehrnsperger and A. Schäefer, *Phys. Lett.* **B348** (1995) 619.

[46] H. Burkhardt and W. N. Cottingham, *Ann. Phys.* **56** (1970) 453.

[47] G. Altarelli *et al*, *Phys. Lett.* **B334** (1994) 187.

[48] H. Quinn and R. A. McDunn, Accelerator, SLAC webpages, (May 1999), Figures 2.1, 2.4 and 2.5 were obtained from the SLAC accelerator webpages.

[49] C. Young, E143 Beam, E143 webpages, (August 1994).

[50] T. Kotseroglou *et al*, *Summary of the 1997 E155 Run - Sources*, E155, Technical Note 104, (1997), unpublished.

[51] L. Stuart, *E154 Beam Energies and Spin Precession*, E154, Technical Note 6, (1995), unpublished.

[52] R. Erickson, T. Fieguth, L. Keller and D. Walz, *SLAC-PUB-5891* (1992).

[53] C. Prescott, *Calibration of the A-line by Spin Precession*, E155, Technical Note 24, (1996), unpublished.

[54] P. S. Cooper *et al*, *Phys. Rev. Lett.* **34** (1975) 1589.

[55] H. R. Band *et al*, *E-154 Møller Polarimeter*, E154, Technical Note 40, (1996), unpublished.

[56] D. G. Crabb *et al*, *Phys. Rev. Lett.* **64** (1990) 2627.

[57] M. L. Seely, *Dynamic Nuclear Polarization of Irradiated Target Materials*, Ph.D. Thesis, Yale University, (1982).

[58] W. Meyer and E. Schilling, in *Proceedings of the 4th International Workshop on Polarized Target Materials and Techniques*, 165. Universitat Bonn, Physikalishes Institut, (1984).

[59] C. Jeffries, *Ann. Rev. Nucl. Sci.* **14** (1964) 101.

[60] A. Honig, *Phys. Rev. Lett.* (1967) 1009.

[61] T. D. Averett, *Measurement of the Spin Structure Function* $g_2(x, Q^2)$ *for the Proton and Deuteron*, Ph.D. Thesis, University of Virginia, (1995).

[62] R. D. Hutchins-Fatemi, Private communication, (August 1999), Discussion of electron-deuteron spin coupled system energy levels.

[63] S. Bültmann *et al*, *NIM* **A425** (1998) 23.

[64] D. G. Crabb and W. Meyer, *Annu. Rev. Nucl. Part. Sci.* **47** (1997).

[65] G. Ferguson, *5.1 Tesla Split Pair for Neutron Beam Polarization Studies, Operator's Handbook*, (1992).

[66] G. K. White, *Experimental Techniques in Low-Temperature Physics*, Oxford University Press, 3rd edn., (1979).

[67] F. Pobell, *Matter and Methods at Low Temperatures*, Springer-Verlag, 2nd edn., (1996).

[68] Y. Kiselev, *NIM* **A356** (1995) 99.

[69] R. D. Hutchins-Fatemi, Private communication, (August 1999), Renee's design and implementation of the target microwave guide assembly.

[70] G. R. Court *et al*, *NIM* **A324** (1993) 433.

[71] A. Abragam, *Principles of Nuclear Magnetism*, Oxford Science Publications, (1961).

[72] P. M. McKee, Private communication, (September 1999), The data for all NMR signals was provided by Paul.

[73] P. M. McKee, E-mail Correspondence, (September 1999), The data obtained from Paul during his proton polarization correction analysis.

[74] A. Melissinos, *Experiments in modern physics*, New York, Academic Press, (1966).

[75] P. McKee, *A Correction to the Proton Polarization from Radiation Damage*, E155, Technical Note 112, (2000), unpublished.

[76] P. M. McKee, *The Spin Structure Function of the Proton from SLAC Experiment E155*, Ph.D. Thesis, University of Virginia, (2000).

[77] G. R. Court and M. A. Houlden, in *Proceedings of the Workshop on NMR in Polarized Targets*, 1. University of Virginia, (1998).

[78] G. R. Court, Virginia Target Group Meeting, (March 2000).

[79] P. Anthony *et al*, *Phys. Lett.* **B493** (2000) 19.

[80] T. Liu, *Measurements of Spin Structure Function* $\mathrm{g_1^p}$ *and* $\mathrm{g_1^d}$ *for Proton and Deuteron at SLAC E143*, Ph.D. Thesis, University of Virginia, (1996).

[81] W. R. Leo, *Techniques for Nuclear and Particle Physics Experiments*, Springer-Verlag, (1992).

[82] G. S. Mitchell, *A Precision Measurement of the Spin Structure Function* $\mathrm{g}_1(\mathrm{x}, \mathrm{Q}^2)$ *for the Proton and Deuteron*, Ph.D. Thesis, University of Wisconsin Madison, (1999).

[83] F. R. Wesselmann, *Precision Measurement of the Spin Structure of the Proton and the Deuteron*, Ph.D. Thesis, Old Dominion University, (1999).

[84] L. Sorrell, *Information on PMTs used for E154/E155/E155x Cherenkov System*, E155, Technical Note 81, (June 1999), unpublished.

[85] P. L. Anthony and Z. M. Szalata, *SLAC-PUB-7201* (1996).

[86] P. Bosted, *10.5 degree Electron Definition*, E155, Technical Note 68, (1998), unpublished.

[87] T. Toole, *A Ground Level Comparision of Two Implementations of the 10.5° Hybrid Definition*, E155, Technical Note 68, (1998), unpublished.

[88] C. Young, *Polarization Bits*, E154, Technical Note 35, (1996), unpublished.

[89] T. Toole, *A Precision Measurement of the Spin Structure Functions* g_1^p *and* g_1^d, Ph.D. Thesis, American University, (2000).

[90] C. Prescott *et al*, *Phys. Lett.* **B84** (1979) 524.

[91] L. G. Levchuk, *NIM* **A345** (1994) 496.

[92] O. A. Rondon, *Phys. Rev.* **C60** (1999) 035201.

[93] F. Sabatié, *Background Subtraction*, E154, Technical Note 45, (1996), unpublished.

[94] Y. Tsai, *Rev. Mod. Phys.* **46** (1974) 815.

[95] T. V. Kuchto and N. M. Shumeiko, *Nucl. Phys.* **B219** (1983) 412.

[96] F. Wesselmann, *Calculation of Radiative Corrections*, E155, Technical Note 100, (1999), unpublished.

[97] F. Wesselmann, *GUF Fit to Global g1/F1 Data Set*, E155, Technical Note 116, (2000), unpublished.

[98] B. Adeva *et al*, *Phys. Rev.* **D58** (1998) 112002.

[99] K. Abe *et al*, *Phys. Lett.* **B405** (1997) 180.

[100] M. Glück, E. Reya and A. Vogt, *Eur. Phys. J.* **C5** (1998) 461.

[101] V. N. Gribov and L. N. Lipatov, *Sov. J. Nucl. Phys.* **15** (1972) 438.

[102] G. Altarelli and G. Parisi, *Nucl. Lett.* **B126** (1977) 298.

[103] G. Mitchell, *E155 NLO Results*, E155, Technical Note 101, (1999), unpublished.

[104] M. Arneodo *et al*, *Phys. Lett.* **B364** (1995) 107.

[105] K. Abe *et al*, *Phys. Lett.* **B452** (1999) 194.

[106] F. E. Close and R. G. Roberts, *Phys. Lett* **B336** (1994) 257.

[107] S. D. Bass and P. V. Landshoff, *Phys. Lett.* **B336** (1994) 537.

[108] S. J. Brodsky, M. Burkardt and I. Schmidt, *Nucl. Phys.* **B441** (1995) 197.

[109] M. Stratmann, *Z. Phys.* **C60** (1993) 763.

[110] X. Song, *Phys. Rev.* **D54** (1996) 1955.

[111] T. D. Averett, *E143 Dilution Factor*, E143, Technical Note 44, (1994), unpublished.

[112] T. D. Averett, *Dilution Factor and corrections for Nitrogen and Lithium Polarizations*, E155, Technical Note 27, (1997), unpublished.

[113] P. Bosted, *Problems with E155 LiD target Insert 5, bottom cell*, E155, Technical Note 66, (1998).

[114] D. T. Hurd, *An Introduction to the Chemistry of the Halides*, John Wiley & Sons, Inc., (1952).

[115] W. M. Mueller, *Metal Hydrides*, Academic Press, (1968).